UNDERSTANDING VARIATIONS AND TRENDS IN CONVECTION OVER THE CONGO BASIN FROM A DIURNAL PERSPECTIVE

by

Kathrin Alber

A Dissertation

Submitted to the University at Albany, State University of New York

In Partial Fulfillment of

the Requirements for the Degree of

Doctor of Philosophy

College of Arts and Sciences

Department of Atmospheric and Environmental Sciences

2024

ABSTRACT

Tropical rainforests regulate global and regional climate systems and play a vital role in the world's water and carbon cycles. The Congo Basin, situated in central equatorial Africa, is home to the second largest rainforest on the planet and is one of the most convective regions in the world. Recent studies indicate that a large-scale and long-term drying trend, characterized by an increase in dry season length, a decrease in forest greenness, and a decrease in precipitation, has been stressing the region since the 1980's. Despite the alarming drying trend and the Congo's important role in the planetary circulation and the global terrestrial water and biochemical cycles, the region remains largely understudied compared to other major rainforests. Motivated by the need to better understand changes in convection and its associations with the drying trend, this dissertation aims to investigate variations and trends in convection from a diurnal perspective and explores relevant physical processes over the region.

First, trends in thunderstorm activity were investigated from 1983 to 2018 across all seasons, i.e., December-February (DJF), March-May (MAM), June-August (JJA), and September-November (SON). An analysis of Gridded Satellite (GridSat-B1) cold cloud fractions (i.e., areas with low brightness temperatures) and the Gálvez-Davison Index (GDI) reveals an increase in thunderstorm activity throughout all seasons, primarily linked to a decrease in hydrostatic stability. More specifically, the observed changes can be attributed to a decrease in temperature at 500 hPa, an increase in the temperature gradient between 700 and 950 hPa, and a decrease of the equivalent potential temperature (θ_e) gradient with height. These changes collectively act to decrease vertical stability and subsequently increase convective activity over the region.

Second, to increase our understanding of trends in thunderstorms over the Congo, changes in the diurnal cycle of convection were investigated from 1979 to 2019, and possible connections to the observed drying trend were explored. An analysis of the fifth generation of the European Centre for Medium Range Weather Forecasts reanalysis data (ERA5) as well as GridSat-B1 and

MODerate Resolution Imaging Spectroradiometer (MODIS) satellite data highlight a decrease in clouds in the morning, contrasted by an increase in clouds and convective activity in the afternoon, during all four seasons. Additionally, findings revealed a decrease in precipitation efficiency (i.e., the ratio between rainfall and total column water) and an increase in cloud base height. These detected changes can potentially be connected to the drying conditions over the region. Elevated surface temperatures and reduced surface relative humidity will likely raise the lifting condensation level, and ultimately decrease the precipitation efficiency. These factors would collectively exacerbate the existing drying trend.

Third, the impacts of the Madden-Julian Oscillation (MJO) on the diurnal cycles of convection and precipitation were evaluated during October through March from 1985 to 2019. GridSat-B1 and Tropical Rainfall Measuring Mission (TRMM) satellite data were used in conjunction with ERA5 reanalysis data, aiming to investigate the differences in the diurnal cycles of convection and precipitation during the MJO enhanced convective phase (RMM phases 1 and 2) versus the MJO suppressed convective phase (RMM phases 5 and 6). Results indicate increased precipitation and convection during the MJO enhanced convective phase and decreased precipitation and convection during the MJO suppressed convective phase as would be expected, where the largest differences were discovered during the morning hours, the time of day when convective processes are weakest. Additionally, the MJO's impact on stratiform precipitation was found to be more pronounced, while the convective precipitation fractions remain similar during both MJO phases. These identified changes were attributed to MJO induced shifts in circulation patterns: Enhanced upward air motion in the mid- and upper levels coupled with strong divergence in the upper levels act to increase stratiform rainfall during the enhanced phase. In contrast, the suppressed phase is characterized by strong mid-level divergence and upper- to mid-level subsidence, mainly during the nighttime and morning hours, resulting in decreased convection and precipitation.

Finally, the impacts of drying soils associated with the Congo drying trend on atmospheric stability and convection were investigated by using the Weather Forecasting and Research (WRF) model. The WRF model was run at a 4 km convection permitting resolution, and hourly ERA5 reanalysis data were used for initial and boundary conditions. Two sets of WRF simulations were conducted, i.e., one dry season case (16-January to 21-January 2018) and one wet season case (21-October to 26-October 2019), resulting in two six-day case studies. For the experiment run (EXP), the soil moisture was decreased by 50% compared to the control run (CTL). No other changes were made to the EXP run. Results highlight a decrease in low-level clouds with drier soils, which was attributed to the simulated decrease in near surface water vapor and increase in temperature in the lower levels. Conversely, mid- and high-level clouds were increased. Factors contributing to the observed increase in clouds include increased lifting condensation level (LCL) and planetary boundary layer (PBL) heights and decreased atmospheric stability due to the warming of the lower levels. Additionally, simulated circulation changes such as increased vertical velocity as well as increased near surface convergence and mid-level divergence likely contribute to the increase in mid-level clouds. Comparing both case studies, the changes during the dry season were more pronounced, possibly due to the already limited moisture availability, while the changes during the wet season were comparatively more subtle.

ACKNOWLEDGMENTS

I wouldn't be able to obtain my PhD without the many people around me who have supported me during this journey.

I would first like to sincerely thank my advisor Dr. Liming Zhou for his invaluable guidance, support, insightful comments, and patience during my time as a graduate student at UAlbany. Liming told me on my first day here that his students are always his top priority and that his door is always open. This commitment to his students has held true during my entire time at UAlbany, where Liming always made it a priority to provide support and guidance when I needed it. While he has always encouraged me to develop my own ideas, he always provided feedback when needed. Thank you for your mentorship and for teaching me how to become a diligent and independent researcher. I would also like to thank Dr. Aiguo Dai, Dr. Brian Rose, and Dr. Paul Roundy for serving as my PhD committee. Thank you for your support and guidance, and always having an open door for feedback when needed. I have appreciated our research discussions and the opportunity to learn from you.

I want to thank the present and former members of the Zhou research group (Stephen, Li, Yan, and Ajay) for many constructive comments and feedback during our group meetings.

I would also like to thank the faculty and staff within the Department of Environmental and Atmospheric Sciences (DAES). I'd like to thank Kevin Tyle, for his support with any IT related questions, especially for helping me to set up and run the WRF model, and for many donut days. Thank you to Chaina and Barb for helping with organizing conference travel and making everyday life as a grad student in the department as easy as possible. I would like to thank the lunch group and my office mates who made the past couple of years a lot more enjoyable.

I was very fortunate to have met many amazing people in Albany and I wouldn't have been able to complete this journey without them. Jeff and Monica with Edith, and Bill who became my family away from home. I am incredibly grateful for the many adventures we have been able to share climbing, cycling, backcountry skiing, and trail running together. Thank you for always supporting me and never stopping to believe in me. I would also like to thank the many people from the ARE running group, especially Tiffany for countless shared laps on the track, and all the runs and races we experienced together. Thank you, Danielle, for always supporting me, especially during tough times.

Finally, I would like to thank my family. My parents for their endless support and sending over many packages of chocolate from Switzerland to make sure I'd never run out of my favorite swiss chocolates. I would also like to thank my brother Jonas for his support and many encouraging messages, and my sister Andrea who is living in Boston. We were incredibly lucky to have ended up living so close together this far away from home. Thank you for always having my back. Lastly, I would like to thank my husband Tyler for his support during this not always easy journey. Thank you for always making sure that I had everything I needed to feel comfortable and for pushing me to do well while also making sure that I took enough breaks from research to go on ice and rock climbing, backcountry skiing, and cycling adventures together.

This research was supported by the National Science Foundation (NSF AGS-1854486).

STATEMENT OF PUBLICATION

The work in Chapter 2, Chapter 3, Chapter 4 has been peer-reviewed and published. The published articles listed below are reprinted in this dissertation with permission of the publisher. The articles were incorporated into this dissertation since they are integral components of this dissertation work. Minor changes were made to ensure the formatting and continuity of this thesis. The respective electronic permissions are attached in the Appendix.

Alber, K., Raghavendra, A., Zhou, L., Jiang, Y., Sussman, H.S., and Solimine, S.L., 2021. Analyzing intensifying thunderstorms over the Congo Basin using the Gálvez-Davison index from 1983–2018. Clim. Dyn., 56, 949–967. Reproduced with permission from Springer Nature.

Alber, K., Zhou, L., and Raghavendra, A., 2021. A shift in the diurnal timing and intensity of deep convection over the Congo Basin during the past 40 years. Atmos. Res., 264, 0169-8095. Used with permission.

Alber, K., Zhou, L., Roundy, P.E., and Solimine, S.L., 2023. Influence of the Madden-Julian Oscillation on the diurnal cycles of convection and precipitation over the Congo Basin. Atmos. Res., 294, 0169-8095. Used with permission.

TABLE OF CONTENTS

ABSTRACT ..... **ii**

ACKNOWLEDGMENTS ..... **v**

STATEMENT OF PUBLICATION ..... **vii**

CHAPTER 1: Introduction **1**

1.1 Background 1

1.2 Literature Review 2

1.2.1 Deep convection and rainfall over the Congo Basin 2

1.2.2 The diurnal cycle of deep convection 4

1.2.3 Role of the Madden-Julian Oscillation 6

1.2.4 Modeling impacts of soil moisture on atmospheric stability and convection 7

1.3 Research Questions 10

CHAPTER 2: Analyzing intensifying thunderstorms over the Congo Basin using the Gálvez-Davison index from 1983–2018 ..... **14**

2.1 Introduction 14

2.2 Data 17

2.2.1 GridSat-B1 satellite data 17

2.2.2 ERA-Interim reanalysis data 18

2.2.3 Dataset limitations 19

2.3 Methods 19

2.3.1 Thunderstorm detection 19

2.3.2 The Gálvez -Davison index (GDI) its sub-indices 20

2.3.3 Column buoyancy index (CBI) 21

2.3.4 Mid tropospheric warming/stabilization index (MWI) 22

2.3.5 Inversion index (II) ... 22

2.3.6 Terrain correction (TC) ... 23

2.3.7 Wind shear ... 23

2.3.8 Trend analysis ... 24

2.4 Results ... 24

2.4.1 More vigorous thunderstorms diagnosed by cold cloud top temperatures ... 24

2.4.2 Changes in GDI and its sub-indices ... 27

2.4.3 Wind shear ... 36

2.5 Discussion and conclusion ... 37

Appendix A: Calculation of θe proxies for each layer from specific humidity and temperature, used to calculate the GDI ... 44

CHAPTER 3: A shift in the diurnal timing and intensity of deep convection over the Congo Basin during the past 40 years ... 49

3.1 Introduction ... 49

3.2 Data ... 51

3.2.1 GridSat-B1 satellite data ... 52

3.2.2 MODIS land surface temperature satellite data ... 52

3.2.3 ERA5 reanalysis data ... 53

3.2.4 CPC precipitation data ... 54

3.3 Methods ... 54

3.3.1 Thunderstorm and cloud detection ... 54

3.3.2 Gálvez-Davison Index ... 55

3.3.3 Precipitation efficiency ... 55

3.3.4 Diurnal cycle analysis ... 56

3.3.5 Trend analysis ... 57

3.4 Results ... 57

3.5 Discussion and conclusions ... 71

CHAPTER 4: Influence of the Madden-Julian Oscillation on the diurnal cycles of convection and precipitation over the Congo Basin ... 76

4.1 Introduction ... 76

4.2 Data ... 79

4.2.1 GridSat-B1 satellite data ... 80

4.2.2 TRMM precipitation data ... 81

4.2.3 ERA5 reanalysis ... 82

4.3 Methods ... 83

4.3.1 MJO Identification ... 83

4.3.2 GridSat-B1 cloud fraction ... 83

4.3.3 Gálvez-Davison Index ... 83

4.3.4 Diurnal cycle calculation ... 84

4.4 Results ... 85

4.4.1 Spatial and temporal anomalies associated with the MJO phases ... 85

4.4.2 Influence of the MJO on the diurnal cycles of convection and rainfall ... 87

4.4.3 Possible physical mechanisms responsible for the MJO induced modulations ... 92

4.5 Summary and discussion ... 98

CHAPTER 5: Impacts of drying soils on atmospheric stability and the diurnal cycle of convection over the Congo Basin ... 103

5.1 Introduction ... 103

5.2 Data and Methods ... 106

5.2.1 Model Setup ... 106

5.2.2 Satellite Data used for Model Validation ... 109

5.2.3 Model Validation ... 109

5.2.4 Gálvez -Davison Index ... 114

5.3 Results ... 114

5.3.1 Impacts on surface heat fluxes, temperature and humidity profiles, LCL, and PBL ... 114

5.3.2 Impacts on atmospheric stability and convective potential ... 119

5.3.3 Impacts on cloud fractions and precipitation ... 127

5.3.4 Impacts on mesoscale circulation ... 129

5.4 Discussion and Conclusions ... 131

CHAPTER 6: Summary, Conclusions, and Future Work ... 136

6.1 Summary and Conclusions ... 136

6.2 Future Work ... 141

References ... 143

Appendix ... 171

CHAPTER 1: Introduction

1.1 Background

The Congo Basin, located in central equatorial Africa, is home to the planet's second largest rainforest and plays a vital role in the world's water and carbon cycles (Creese at al. 2019). It is a global epicenter for biodiversity and has an important impact on climate change (Lewis 2006). Central Africa is also a hotspot for thunderstorms and is one of the most convective regions in the world, characterized by intense thunderstorm activity (Dai 2001a; Zipser et al. 2006), a greater annual mean lighting flash rate than the rest of the deep tropics (Christian et al. 2003), and the second largest heating rate from convection after the Indonesian maritime continent (MC) (Washington et al. 2013). The extraordinarily high heating rate is the primary driver of the regions general circulation through condensation of water vapor in deep convective clouds, while the latitudinal temperature gradient is weak (Brncic et al. 2007; Webster 1973).

Recent studies have documented a long-term and large-scale drying trend accompanied by a decreasing trend in rainfall over the Congo (e.g., Zhou et al. 2014). This drying trend has led to forest browning, reduced canopy water content, increased dry season length (Jiang et al. 2019), increased forest fires, as well as changes in plant growth, water availability, biodiversity, agriculture, and human health (Nkem et al. 2013; Kamitewoko 2021). The Congo rainforest already exists close to the hydrological limits of closed-canopy forest which is largely impacted by climatic variability and hydrological changes (Lewis et al. 2009). Consequently, higher-biomass and closed-canopy forests such as the Congo might transition to more open and lower-biomass forests with lower water availability over a longer time-period (Zhou et al. 2014). Furthermore, African arid regions and drylands will be expanding under a warming climate (Feng and Fu 2013), and continued deforestation as a result of agricultural demands is posing another threat to the Congo rainforest (Chakraborty et al. 2019). Despite its important role in the global climate system, and its vulnerability to climate change, the Congo remains largely understudied compared to other major rainforests such as the Amazon or the rainforests of the MC (Adler et al. 2017). This is mainly associated with the lack of long-term homogenous and widespread rainfall records, in-situ measurements, and other climate observations in the region, where the number of rain gauges have been decreasing since 1980 (Washington et al. 2013). Thus, it is imperative to understand deep convection in order to better comprehend the variability in rainfall and convection across the region. This is especially crucial for investigating recent trends and changes in convection associated with the drying trend over the Congo Basin. Since large parts of the tropical rainfall and cloudiness can mainly be explained by the diurnal cycle controlled by surface heating over land (Yang and Slingo 2001), it will also be important to examine how the drying trend is affecting the intensity and timing of the diurnal cycle of convection and cloudiness over the Congo. Additionally, modes of variability like the Madden-Julian Oscillation (MJO) influence convection and precipitation variability and interact with the diurnal cycles of deep convection and precipitation over the Congo (Slingo et al. 2003; Sakaeda et al. 2017; Hart et al. 2019; Jiang et al. 2021). Consequently, it will be helpful to investigate such influences and interactions in order to be able to understand trends in thunderstorm activity and the diurnal cycle of deep convection.

1.2 Literature Review

1.2.1 Deep convection and rainfall over the Congo Basin

The Congo Basin is one of the three most convective regions in the tropics and influences the large-scale tropical circulation together with the two other major convective regions, i.e., the MC and Amazonia (Webster 1973; Washington et al. 2013). However, despite the Congo's formidable convection heating rate, thunderstorm intensity and lightning activity, the region receives less rainfall than the Amazon or the MC (Adler et al. 2017), and the mean precipitation has been decreasing further during recent years (Zhou et al. 2014; Hua et al. 2016, 2018). In contrast to the decreasing rainfall trends, Raghavendra et al. (2018) found an increase in the number, size, and intensity of thunderstorms over the time period of 1982–2016 during April, May, and June (AMJ), using satellite data. These results were later complemented by other studies which point to a general increase in thunderstorm activity over the Congo Basin throughout the year (e.g., Taylor et al. 2018; Hart et al. 2019). This seemingly unintuitive relationship between increasing thunderstorm activity and decreasing rainfall over the Congo may be reconciled by Hamada et al. (2015), who demonstrated a weak relationship between thunderstorm intensity and rainfall in the tropics. However, specific physical mechanisms explaining the complex relationship between tropical deep convection, surface rainfall, and an increase in thunderstorm activity over the Congo have only been incompletely identified. One explanation given for the observed increase in thunderstorm activity over the Congo Basin includes an increase in horizontal wind shear attributed to an increasing temperature contrast between the equator and northern Africa (Taylor et al. 2018).

The potential and intensity for atmospheric convection can generally be determined by assessing the thermodynamic stability of the atmosphere. Therefore, thermodynamic indices are often collectively used to assess atmospheric stability. However, although stability indices have been widely used to forecast thunderstorms (e.g., Haklander and Van Delden 2003; Jayakrishnan and Babu 2014), Gálvez and Davison (2016) found that traditional stability indices often lack skill when attempting to predict tropical convection since the processes driving convection differ between the tropics and the extra-tropics, and stability plays a different role in the development of moist convection. Quantifying tropical convection can be challenging since the skill of traditional stability indices like the Lifted-Index (LI), K-Index (KI), Showalter-Index (SI) or convective available potential energy (CAPE) in predicting deep convection is limited for the tropics (Uma and Das 2019). In the mid-latitudes, convection can be triggered by dynamic processes (e.g., frontal systems) while tropical convection depends more on column stability and thermodynamic processes since dynamical processes are usually weak. Aiming to improve forecasts for tropical convection, the Gálvez-Davison Index (GDI) was developed by the NOAA Weather Prediction Center (WPC) in 2014, focusing on thermodynamic processes more than on dynamical processes (Gálvez and Davison 2016). Miller et al. (2019) utilized the GDI and other stability indices to forecast rainfall in Puerto Rico and found that CAPE, the KI and Total Totals had little skill when compared to the GDI. Since the GDI is a relatively new index, follow-up studies are limited in numbers.

Spatial extent and intensity of convection can also be estimated using satellite data. Satellite measured brightness temperature (T_b) is often used to detect convective clouds, where T_b is a measurement of the radiance of an object, expressed in units of the temperature of an equivalent blackbody. Convective clouds can be detected by quantifying cloud top T_b. More specifically, lower T_b are indicative of deeper convection since low T_b point to cold cloud top temperatures, and cold cloud tops are indicative of stronger and deeper convection. Thus, the lower the T_b, the stronger and more intense are convection and thunderstorms (Hong et al. 2005; Mapes and Houze 1993; Schmetz et al. 1997).

1.2.2 The diurnal cycle of deep convection

The diurnal cycle is one of the most fundamental modes of atmospheric variability, attributable to large variations in the solar forcing over the course of the day, and rainfall and convection in the tropics are largely influenced by the diurnal cycle (Dai 2001b; Dai et al. 2007; Yang and Slingo 2001). For the rainfall in the tropics, the maximum is reached during the mid- to late afternoon over land and at nighttime over oceans. The maximum rainfall in the afternoon over land is a result of surface solar heating during the day, destabilizing the atmosphere and subsequently encouraging the onset of convection (Yang and Smith 2006). Over most tropical land areas, mornings are relatively clear, followed by a rapid afternoon buildup of convective clouds associated with a maximum in rainfall and a more gradual decay of clouds during the night (Garreaud and Wallace 1997).

The diurnal cycles of tropical convection and rainfall have been studied extensively and various methods have been used to analyze the diurnal cycles of clouds and precipitation over different tropical regions, where significant differences exist over land compared to oceans. For example, using water vapor absorption band radiance data from geostationary satellites, Soden (2000) found significant diurnal variations in the upper tropospheric relative humidity in the tropics over both land and oceans, where the variations over land are out of phase with those over the oceans. Tian et al. (2004) showed large diurnal variations in deep convection, precipitation, and high clouds over deep convective regions. They indicated that upper tropospheric relative humidity peaks around midnight over oceans and at 03:00 LST over land, with stronger diurnal variations of deep convection over land, which maximizes in the late afternoon and early evening hours. Hendon and Woodberry (1993) further investigated the diurnal cycle of tropical convection using global cloud imagery derived from 11μm satellite radiance measurements. Using only T_b lower than 230 K to isolate deep convection, they found the diurnal amplitude of deep convection to be significant over tropical landmasses while the diurnal cycle is weak over tropical oceans. Worku et al. (2019) investigated the diurnal cycle of rainfall, convection, and precipitation features over the MC using Tropical Rainfall Measuring Missions (TRMM) Multi-satellite Precipitation Analysis as well as data from the convective classifications from the International Satellite Cloud Climatology Project (ISCCP). Their results show isolated convection initiating around midday over the elevated parts of the larger islands, and convection becoming more organized during the afternoon and evening hours, with a peak in rainfall over the islands around 18:00-21:00 LST.

During the nighttime, convection is shown to propagate offshore where the rainfall peak is recorded around 06:00-09:00 LST. Angelis et al. (2004) investigated the diurnal cycle of rainfall over the Brazilian Amazon using 3 years of 3-hourly data from 24 rain gauges. They found the rainfall over the study area to be highly variable spatially and temporally with the northern Amazon forming the wettest and the southern Amazon forming the driest part. A diurnal cycle of rainfall was evident for all locations, but the diurnal rainfall peak was found to be at different times depending on the station. For Africa, Yang and Slingo (2001) used global 0.5º and 3-hourly satellite infrared data to provide a climatology of the diurnal cycle of convection and surface temperature in the tropics, showing that the moisture budget over central Africa is dominated by the diurnal cycle.

Little has been published about the diurnal cycle of convection over the Congo Basin, although analyzing the causes and effects of a shift in the diurnal timing and intensity of deep convection over the Congo Basin would be an important step in better understanding the observed drying trend over the region and implications of climate change. This emphasizes the need to better understand the diurnal cycle of convection over the region and how it has been affected by the ongoing drying trend.

1.2.3 Role of the Madden-Julian Oscillation

Subseasonal climate variability such as temperature extremes, dry spells, floods, or unusual high or low precipitation, have important impacts on ecosystems, agriculture, infrastructure, lives, and livelihoods in central equatorial Africa and can have significant economic and social consequences (Zaitchick 2017). Africa is one of the most vulnerable continents to climate variability, and central equatorial Africa is particularly at risk due to its rural population and agriculture practices that are rainfed (Sandjon et al. 2012). One important factor influencing rainfall and convection on intraseasonal timescales over the Congo is the MJO, the dominant mode of subseasonal climate variability in the tropics (Madden and Julian 1971; Madden and Julian 1972). Zaitchick (2017) showed that the MJO has a significant impact on intraseasonal rainfall variability over Africa including the Congo, while Raghavendra et al. (2020) indicated a relationship between the number of wet and dry MJO days and rainfall enhancement and suppression over the Congo. They further found a significant increase in MJO dry days since 1979 which may help to partially explain the drying trend over the region. However, most other studies analyzing the impacts of the MJO on the African continent have focused on Eastern Africa (e.g., Pohl and Camberlin 2006; Berhane and Zaitchik 2014; Vashisht and Zaitchik 2022; Maybee et al. 2022; Talib et al. 2023), Southern Africa (e.g., Hart et al. 2013) or Western Africa (e.g., Alaka and Maloney 2012; Sossa et al. 2017). Understanding how the different phases of the MJO impact convection, rainfall, and their diurnal cycles over the region may not only help to enhance our understanding of rainfall variability and variations in convection over the region, but might also help to improve weather forecasts, allowing farmers to better plan ahead, reducing negative impacts of unpredicted anomalous precipitation or droughts on their livelihoods.

1.2.4 Modeling impacts of soil moisture on atmospheric stability and convection

To improve our understanding of physical mechanisms in a climate system, numerical models are often used. For regional climate studies, regional climate models (RCMs) are utilized as they represent fine-scale physical processes more accurately. However, the simulation of deep convection and convective precipitation is challenging in climate models since the horizontal grid spacing in RCMs is coarse and typically larger than 12 km (Jacob et al. 2014) and cumulus parameterizations are required for coarser resolutions. Since deep convection can be triggered from various factors and processes ranging from microscale to the synoptic and planetary scales, parameterizing deep convection is challenging and cumulus parameterization schemes are one of the main contributors to errors and uncertainties in RCMs (Sherwood et al. 2014; Déqué et al.

2017). Additionally, since convective parameterization schemes interact with other schemes, weaknesses in convective parameterization can impact other schemes as well. Using convection parameterization schemes can therefore lead to errors like the misrepresentation of the diurnal cycle of convective precipitation (Dai et al. 1999). To simulate convection and convective precipitation more accurately, a higher spatial resolution is necessary and convection-permitting models (CPMs) with at least 4 km horizontal grid spacing have been shown to significantly improve the representation of convection. CPMs do not rely on convection parameterization schemes since deep convection starts to be resolved explicitly at smaller grid scales and convection parametrization schemes can be switched off (Weisman et al. 1997; Prein et al. 2015). Convective processes are therefore simulated more realistically in CPMs than in coarse resolution models. The Weather Research and Forecasting (WRF) model has been used frequently to study the diurnal cycle of precipitation and convection at regional scales (e.g., Evans and Westra 2012; Hassim et al. 2016; Scaff et al. 2020). Hassim et al. (2016) examined the diurnal cycle of rainfall over New Guinea using convection-permitting WRF model simulations, focusing on a period of suppressed regional-scale conditions in February 2010 with maximized local diurnal forcings. The modeled diurnal precipitation showed good agreement with the satellite-observed rainfall derived from the TRMM 3B42 product. Furthermore, Jucker et al. (2020) used convection-permitting simulations in WRF to simulate convection over tropical Australia, while Heath and Fuelberg (2014) used WRF convection-permitting simulations to examine regions where convection is impacting the Asian summer monsoon anticyclone. Rasmussen and Houze (2016) used WRF to simulate mesoscale convective systems in the Andes in subtropical South America, analyzing the effects of various topographic features on Mesoscale Convective Systems (MCSs).

Convective initiation requires a supply of available energy from the environment (i.e., convective available potential energy and gross moist instability) as well as dynamic conditions for the energy to be released (i.e., rising motion and lower wind shear) (Fu et al. 1999). For convection to develop, solar heating warms the Earth's surface and lower atmosphere, and heat is subsequently transported upward from the surface, where warmer and/or moister air at the surface will lead to more vigorous convection and higher cloud tops. Consequently, changes in land surface properties such as changes in soil moisture may influence the initiation and development of convection by modulating the solar heating at the surface and thereby influencing atmospheric temperature and humidity profiles (Betts and Ball 1998; Taylor and Ellis 2006; Taylor 2015). However, studies disagree on how soil moisture affects convective storms across the globe (Taylor 2015). Polcher (1995) showed that deforestation in tropical land areas will lead to an increased sensible heat flux and therefore more deep convective events, where the reduction of evaporation caused by deforestation modulates this mechanism by decreasing precipitation. Guillod et al. (2015) showed that afternoon precipitation over central Africa falls more often over soils that are drier than their surroundings, and Taylor et al. (2012) showed that rain in the afternoon is generally more likely to fall over areas that are wetter than surrounding areas, where this phenomenon is most pronounced over semi-arid regions, where new convection typically occurs near the boundary between cool, wet regions and a dry region.

Analyzing how a decrease in soil moisture will affect convection over the Congo will be an important step in determining how the drying trend might be influencing convection over the region. The long-term drought over the Congo is expected to largely reduce surface latent heat due to decreased soil moisture, which functions as a transition to shift the energy partitioning mostly toward sensible heat and thus warm the surface and the planetary boundary layer (Zhou et al. 2014). Although there are no regional studies about how changes in soil moisture impact convection over the Congo, the WRF model has previously been used to investigate the impacts of changes in soil moisture on various variables in other regions. Yuan et al. (2017) used WRF to assess the impacts of initial soil moisture and the vegetation fraction on the diurnal temperature range in China's semiarid and arid regions. They found that soil moisture affects the daily maximum and minimum temperatures by changes in the distribution of the available energy between the sensible and latent heat fluxes during the day and by changes in the surface emissivity during the night. Additionally, variations in the vegetation fraction are shown to modify the surface radiation and the energy budget. Zeng et al. (2014) used a succession of 24-hour WRF simulations to investigate the sensitivity of a short-range high-temperature weather event in July 2003 in East China to initial soil moisture conditions and indicated that hot weather can be amplified under low soil moisture conditions. Furthermore, Zhang et al. (2018) used WRF to simulate the impacts of soil moisture on summer heatwaves over the contiguous U.S. and showed that soil moisture can amplify the frequency and intensity of summer heatwaves through soil moisture-temperature feedbacks.

1.3 Research Questions

Motivated by the importance to gain a better understanding of trends and variations in convection over the Congo rainforest, I pursue the research outline presented below, including a brief motivation, research question, and hypotheses for each section, in four chapters.

Chapter 2: Analysis of trends in thunderstorm activity

Motivation: Several recent studies have detected a large-scale and long-term drying trend over the Congo basin, which is accompanied by a decline in forest greenness and canopy water content and an increase in dry season length. While rainfall has been shown to be decreasing, Raghavendra et al. (2018) found an increase in the number, size, and intensity of thunderstorms over the region during April, May, and June in recent years. Similarly, Taylor et al. (2018) highlight an increase in intense MCS frequency over the Congo during February, while Hart et al. (2019) found a general increase in convective activity over Africa during the satellite era. Some factors suggested to play a role in the observed increase in thunderstorm activity include increased shear favoring intense MCSs associated with baroclinicity trends and strong warming north of the Congo (Taylor et al. 2018), and interhemispheric asymmetry in surface warming (Hart et al. 2019). However, a comprehensive and extensive study analyzing trends in convective activity during all months of the year including an analysis of the physical mechanisms responsible for the observed trends has not been conducted yet over the Congo.

Research Question #1: What are the trends in thunderstorm activity during all four seasons over the Congo Basin during recent years? What physical mechanisms are causing the observed trends in thunderstorm activity?

Hypothesis: Despite an observed decrease in rainfall, thunderstorm activity over the Congo has been increasing. The warming and drying trend over the region is likely contributing to a decrease in atmospheric stability, which is resulting in more vigorous convection and thunderstorms over the region.

Chapter 3: Changes in the diurnal cycle of deep convection

Motivation: Thunderstorm activity over the Congo has been increasing, while several studies have documented a large-scale and long-term drying trend over the region. Since thunderstorms and convection over the Congo Basin are largely influenced by the diurnal cycle, which is mainly controlled by surface solar heating, the drying trend observed over the region may have an important impact on diurnal variations of convection and clouds, characterized by changes in the diurnal cycle of convection. However, a comprehensive analysis of changes of the diurnal cycle of convection and potential associations with the drying trend has not been conducted yet.

Research Question #2: How has the diurnal cycle of deep convection been changing during the past 40 years? What are the mechanisms contributing to the changes?

Hypothesis: The diurnal amplitude of deep convection has increased, due to a decrease of clouds in the morning, an earlier onset of convection, and more vigorous convection in the afternoon. These changes may have been caused by the warming and drying trend observed over the region. The warmer and drier conditions are possibly leading to a decrease in cloud cover in the morning due to the decreased moisture availability (i.e., greater CIN), while the surface warming is enhancing the vertical temperature gradient and decreasing the equivalent temperature gradient (i.e., greater CAPE), which will ultimately increase convective potential in the afternoon.

Chapter 4: Impacts of the MJO on the diurnal cycles of convection and rainfall

Motivation: The MJO is one of the most fundamental modes of atmospheric variability and profoundly influences precipitation and convection over the tropics. However, although the impacts of the MJO on African climate have been analyzed, most studies have focused on Eastern Africa, Southern Africa, and Western Africa, while studies focusing on the Congo are very limited. Raghavendra et al. (2020) found a significant relationship between the MJO and rainfall during October through March and showed a decreasing number of MJO dry days, which may be contributing to the observed decrease of rainfall over the region. Other studies on the MJO's influence over the Congo are limited in numbers. While the impact of the MJO on convection, cloudiness, and rainfall, as well as their diurnal cycles have been extensively studied over other tropical regions such as the maritime continent, an examination on the MJO's impacts on convection and rainfall from a diurnal perspective has yet to be conducted over the Congo.

Research Question #3: How does the MJO impact the diurnal cycles of convection and precipitation? What are the mechanisms controlling the observed impacts on convection and rainfall?

Hypothesis: The MJO highly impacts the diurnal timing and intensity of deep convection and precipitation over the Congo and thus significantly contributes to variations in convection and precipitation over the region. During the MJO enhanced convective phase, convective activity and precipitation over the Congo are increased, increasing their diurnal amplitudes, and delaying the peak of convection to later in the day. During the MJO suppressed convective phase, convective activity over the Congo is weakened and precipitation is decreased, decreasing the diurnal amplitudes of convection and precipitation, and shifting the peak in convection to earlier in the day. These impacts are the result of circulation changes caused by the MJO.

Chapter 5: Impacts of drier soils on atmospheric stability and convection

Motivation: Land surface properties such as soil moisture can modulate clouds and convection through land-air interactions and changes in the partitioning of the surface heat fluxes and the PBL. Thus, the observed drying trend over the Congo may be influencing thunderstorm activity over the region through changes in soil moisture. However, there is a lack of studies investigating how drier soils might influence atmospheric stability and convection over rainforests in general and over the Congo specifically. Therefore, it will be crucial to understand how the observed drying trend may be impacting clouds and convection over the region.

Research Question #4: How does a decrease in soil moisture impact atmospheric stability and the diurnal cycle of convection? What are the mechanisms causing the changes in atmospheric stability and convection? How do the changes compare during the wet vs. the dry season?

Hypothesis: Since the diurnal cycle of deep convection is mainly controlled by surface heating, the long-term drying trend greatly modifies the diurnal cycle of convection. Drying conditions characterized by a decrease in soil moisture will result in a decreased latent heat flux and an increased sensible heat flux, increasing surface heating and decreasing humidity. These changes collectively act to decrease atmospheric stability, subsequently increasing convection in the afternoon. The impacts are more pronounced during the dry season due to the already limited water availability.

CHAPTER 2:

Analyzing intensifying thunderstorms over the Congo Basin using the Gálvez-Davison index from 1983–2018

This chapter addresses research question 1) in Chapter 1.3 by analyzing trends in cold cloud fraction and the GDI, including its sub-indices, over the Congo during all four seasons from 1983 to 2018. The hypothesis of this study includes that despite a decrease in rainfall, thunderstorm activity over the Congo has increased as a result of the observed drying trend. The warming and drying conditions over the region have decreased atmospheric stability and thereby decreased convective inhibition, resulting in more vigorous convection over the region.

This article was published in Alber, K., Raghavendra, A., Zhou, L., Jiang, Y., Sussman, H.S., and Solimine, S.L., 2021a. Analyzing intensifying thunderstorms over the Congo Basin using the Gálvez-Davison index from 1983–2018. Clim. Dyn. 56, 949–967.

2.1 Introduction

Most of the precipitation in the tropics stems from convective rainfall (Dai 2006). Naturally, the majority of the rainfall over the Congo Basin located in equatorial central Africa originates from deep convection and mesoscale convective systems (Jackson et al. 2009). The Congo Basin, Amazonia, and the Indonesian maritime continent form the three most convective regions on the globe and enhance the large-scale tropical circulation (Zipser et al. 2006; Raghavendra et al. 2019). In fact, thunderstorms over the Congo are typically stronger and more intense when compared to other equatorial regions like Amazonia or Indonesia. In spite of its smaller size, the Congo is characterized by the second largest latent heating rate from convection after the Indonesian maritime continent (Washington et al. 2013). Equatorial Africa is also associated with the greatest annual mean lightning flash rate, having a higher frequency in thunderstorm occurrence and mean flash rate than the rest of the deep tropics (Christian et al. 2003). However, despite the Congo's formidable convection heating rate, thunderstorm intensity and lightning activity, the second largest rainforest in the world, i.e., the Congo Basin, receives less rainfall per unit area than Amazonia or Indonesia (Adler et al. 2017). The reduced availability of rainfall exacerbates the Congo rainforest's vulnerability to droughts when compared to other major rainforests (Zhou et al. 2014). On a concerning note, trends in the mean rainfall, forest greenness, and dry season length over the Congo Basin indicate a long-term and large-scale drying trend (Zhou et al. 2014; Jiang et al. 2019).

In order to understand rainfall variability and to identify potential drivers for the well-documented decrease in rainfall over the Congo, there exists a crucial need to understand deep convection. This emphasizes the need to investigate recent trends in thunderstorm activity over the Congo Basin. Despite the decrease in rainfall rates in the Congo Basin, Raghavendra et al. (2018) found an increase in number, size and intensity of thunderstorms over the time period of 1982–2016 during April, May, and June (AMJ), using satellite data. These results were later complemented by other studies which point to a general increase in thunderstorm activity over the Congo Basin throughout the year (e.g., Taylor et al. 2018; Hart et al. 2019; Raghavendra et al. 2019). This seemingly unintuitive relationship between increasing thunderstorm activity and decreasing rainfall over the Congo may be reconciled by Hamada et al. (2015), who demonstrated a weak relationship between thunderstorm intensity and rainfall. However, specific physical mechanisms explaining the complex relationship between tropical deep convection, surface rainfall, and an increase in thunderstorm activity over the Congo have only been incompletely identified. One explanation given for the observed increase in thunderstorm activity over the Congo Basin includes an increase in horizontal wind shear attributed to an increasing temperature contrast between the equator and northern Africa (Taylor et al. 2018).

Thermodynamic stability of the atmosphere is a key ingredient which determines the potential and intensity for atmospheric convection. Often, thermodynamic indices are collectively used to assess the stability of the atmosphere. Although stability indices have been widely used to forecast thunderstorms (e.g., Haklander and Van Delden 2003; Jayakrishnan and Babu 2014), Gálvez and Davison (2016) found that traditional stability indices often lack skill when attempting to predict tropical convection since the processes driving convection differ between the tropics and the extra tropics, and stability plays a different role in the development of moist convection. Quantifying tropical convection can be challenging since the skill of traditional stability indices like the Lifted-Index (LI), K-Index (KI), Showalter-Index (SI) or convective available potential energy (CAPE) in predicting deep convection is limited for the tropics (Uma and Das 2019).

In the mid-latitudes, convection can be triggered by dynamic processes (e.g., frontal systems). However, tropical convection depends more on column stability and thermodynamic processes since dynamical processes are usually weak. Aiming to improve forecasts for tropical convection, the Gálvez-Davison Index (GDI) was developed by the NOAA Weather Prediction Center (WPC) in 2014, focusing on thermodynamic processes more than on dynamical processes (Gálvez and Davison 2016). Miller et al. (2019) utilized the GDI and other stability indices to forecast rainfall in Puerto Rico and found that CAPE, the KI and Total Totals had very little skill when compared to the GDI. Since the GDI is a relatively new index, follow-up studies are limited in numbers. In this study, the GDI and its sub-indices are utilized to investigate the increasing trends in thunderstorm activity over the Congo during different seasons, and thus providing a perspective to understand thermodynamic characteristics of thunderstorm as well as profound indications of changes in thunderstorm activity. The physical processes influencing the GDI trends are later diagnosed in order to gain a better understanding about the increasing trend in a thunderstorm activity and decreasing trend in rainfall over the Congo.

2.2 Data

This study focuses on the Congo Basin, which is defined as the area from 5° N–5° S and 12° E–25° E. All four seasons, i.e., December, January, February (DJF), March, April, May (MAM), June, July, August (JJA) and September, October, November (SON) were examined. MAM and SON are the two wet seasons and DJF and JJA are the two dry seasons (Pokam et al. 2012; Dyer et al. 2017), where dry seasons in the tropics represent yearly periods with low amounts of rainfall, which coincide with the seasonal shift of the tropical rain belt (Nicholson 2018; Jiang et al. 2019). Two different datasets were used in this study, i.e., a satellite and reanalysis dataset.

2.2.1 GridSat-B1 satellite data

Infrared (IR) channel brightness temperature (T_b) from the Gridded Satellite (GridSat-B1) dataset sampled by the European Meteosat (MET) series of geostationary satellites, available from 1981–present (Knapp 2008; Knapp et al. 2011), was used in this study. The GridSat-B1 dataset was created by remapping and merging the International Satellite Cloud Climatology Project (ISCCP) B1 data onto 0.07° × 0.07° grids using nearest-neighbor sampling at a 3-h temporal resolution. The GridSat-B1 dataset provides a uniform set of quality controlled geostationary satellite observations for the visible (0.7 µm), infrared window (11.0 µm) and infrared water vapor (7.7 µm) channels. However, only the IR channel T_b has received more extensive inter-satellite calibration and is thus identified as a Climate Data Record (NRC 2004). Raghavendra et al. (2020) reported large volumes of missing data between 1982 and 1985 in the GridSat-B1 data record. However, T_b from 1983 to 2018 was used in this study since seasonal means were used, and missing data is occurring in smaller chunks.

2.2.2 ERA-Interim reanalysis data

The ERA-Interim dataset (ERA-I; Dee et al. 2011) was used to obtain atmospheric temperature and specific humidity at 950 hPa, 850 hPa, 700 hPa and 500 hPa, and zonal (u) and meridional (v) wind at 850 hPa and 500 hPa at a 0.7° × 0.7° spatial resolution. Although reanalysis products other than the ERA-I dataset could have been utilized for this study, the lack of surface observations and radiosonde networks over the Congo Basin makes it challenging to identify the most accurate reanalysis dataset (Washington et al. 2013; Hua et al. 2019). However, the bias and the root-mean-square error associated with the ERA-I wind field is found to be comparable to other reanalysis datasets and therefore the ERA-I dataset is found to be adequate for this study (Hua et al. 2019).

The ERA-I dataset was produced by the European Centre for Medium-Range Weather Forecasts (ECMWF) using the Integrated Forecast System (IFS) release Cy31r2 which was used for operational forecasting between 12 December 2006 and 5 June 2007 (Dee et al. 2011). Since the GDI was developed for the operational analysis and forecasting of tropical convection, the atmosphere needs to be evaluated before convection has occurred. Over the Congo Basin, thunderstorm activity is strongly influenced by the tropical diurnal cycle (Yang and Slingo 2001) and convection usually peaks between 15:00 and 18:00 UTC. Therefore, monthly mean data at 12:00 UTC was used from the ERA-I reanalysis dataset for all calculations to evaluate thunderstorm activity at 15:00 UTC using satellite observations from the GridSat-B1 data. The ECMWF forecast model is regarded as one of the most accurate numerical weather prediction models in the meteorological model community (Buizza et al. 2005; Wedam et al. 2009; Perez et al. 2010), therefore the ERA-I reanalysis dataset is also likely to be the best reanalysis dataset choice for this study due to the 3-h lag in evaluating the reanalysis data (atmospheric variables) and satellite observations (thunderstorm activity).

2.2.3 Dataset limitations

The GridSat-B1 dataset was derived from more than 30 geostationary satellites (Knapp 2008) and the data covering the Congo Basin was sampled by the European Meteosat (MET) series of geostationary satellites (MET 2–10) that provide excellent coverage over Central Africa (Raghavendra et al. 2018). Despite improved data processing and inter-satellite calibrations (Knapp 2012), the possibility that long-term trends estimated from the GridSat-B1 may suffer from biases associated with inter-satellite calibrations, satellite view zenith effects, gaps in coverage, and differences in instrument spectral response functions cannot be excluded (Knapp 2016). Therefore, higher-quality datasets and modeling work will be included in future studies.

Differences and uncertainties among different reanalysis products, climate model simulations and satellite derived datasets over the Congo Basin (Diem et al. 2014; Hua et al. 2019), and the lack of observations to validate the model outputs and reanalysis data (Washington et al. 2013; Alsdorf et al. 2016) represent a major challenge for scientific studies over the Congo. A limitation of this study therefore includes the poor correlation between different observation and reanalysis datasets over the Congo Basin, especially for moisture fields (Lee and Biasutti 2014). The fact that only one reanalysis dataset was used represents another limitation of this study. But, the data requirements for the analysis performed for this study are very specific, i.e., daily data at 12:00 UTC for specific pressure levels at a fine resolution. Therefore, only one reanalysis dataset was analyzed.

2.3 Methods

2.3.1 Thunderstorm detection

In order to evaluate thunderstorm activity and trends using satellite data, low T_b values (e.g., $T_b < -50$ °C) were used to detect cold cloud top temperatures, which may be used to quantify thunderstorm spatial extent and intensity. The lower the T_b, the deeper the convection and the stronger the intensity of the storm (Raghavendra et al. 2018). In order to detect intense thunderstorms over the Congo, cold cloud fraction with T_b between − 50 and − 70 °C was estimated from the re-gridded GridSat-B1 data by calculating the percentage (%) of pixels with T_b between − 50 and − 70 °C within each 0.98° × 0.98° grid.

2.3.2 The Gálvez -Davison index (GDI) its sub-indices

The GDI was calculated as a measure of thunderstorm potential over the Congo Basin. It consists of three different sub-indices analyzing different physical processes and a terrain correction, and is calculated as follows:

$$GDI = CBI + MWI + II + TC \qquad \text{Eq. (2.1)}$$

where the three sub-indices are the Column Buoyancy Index (CBI) considering the availability of heat and moisture in the middle and lower troposphere, the Mid-Tropospheric Warming Index (MWI) considering stabilizing and destabilizing effects of mid-level ridges and troughs, and the Inversion Index (II) considering entrainment of dry air and stabilization associated with trade wind inversions. There is also an optional terrain correction (TC) that can be added. GDI values range from around − 20 to + 45, indicating the thunderstorm potential. GDI values of − 20 indicate fair conditions and shallow convection producing very light, isolated rain. GDI values around + 45 indicate a high potential for scattered to widespread thunderstorms.

In order to calculate the GDI and its sub-indices, temperature and specific humidity at four vertical levels, i.e., 950 hPa, 850 hPa, 700 hPa, and 500 hPa were obtained from the ERA-I data. Those four vertical levels are used to define three layers, i.e., A, B, and C. A evaluates the conditions at 950 hPa, B evaluates the conditions averaged over 850 hPa and 700 hPa, and C evaluates the conditions at 500 hPa (Gálvez and Davison 2016). Specific humidity and temperature data were used in order to obtain relative humidity for each level (Bolton 1980; Brock and Richardson 2001). The formulas used to derive mixing ratios (r), potential temperature (θ), and equivalent potential temperature (θ_e) proxies for each layer (Betts and Dugan 1973; Bolton 1980; Gálvez and Davison 2016), which are needed to calculate the GDI, are documented in Appendix A.

2.3.3 Column buoyancy index (CBI)

The CBI analyzes moisture availability and temperature of the layers A and C by calculating the θ_e of those layers. The CBI is an enhancement factor and produces positive values. It is the only sub-index of the GDI producing positive values. The higher the CBI is, the larger is the potential for deep convection. Deep convection is characterized by a warm and moist mid tropospheric layer (ME) which is being reinforced by a warm and moist layer in the lower troposphere (LE). A high CBI therefore indicates the presence of a deep moist layer, leading to deep convection and potential heavy rainfall. The CBI is calculated as follows:

$$ME = \theta_{e(C)} - \beta \qquad \text{Eq. (2.2)}$$

$$LE = \theta_{e(A)} - \beta \qquad \text{Eq. (2.3)}$$

$$CBI = \begin{cases} \gamma \times LE \times ME, & LE > 0 \\ 0, & LE \leq 0 \end{cases} \qquad \text{Eq. (2.4)}$$

where $\beta = 303\,K$ is an empirical constant, which is used to set a lower boundary for the availability of heat and moisture in the boundary layer, and $\gamma = 6.5\,x\,10^{-2}\,[K^{-1}]$ is an empirical scaling factor used to obtain values comparable to the relatively better-known K-Index (Gálvez and Davison 2016).

2.3.4 Mid tropospheric warming/stabilization index (MWI)

By calculating the temperature of layer C, the MWI considers mid tropospheric stabilization induced by warm ridges and destabilization by cold troughs. The MWI is an inhibition factor producing negative values. If temperatures are higher than the threshold $\tau = 263.15\ K$, MWI values are negative, indicating strong inhibition of convection and stabilization of the layer by a warm ridge. The MWI is calculated as follows:

$$MWI = \begin{cases} \mu \times (T_{500} - \tau), & T_{500} - \tau > 0 \\ 0, & T_{500} - \tau \leq 0 \end{cases} \qquad \text{Eq. (2.5)}$$

where $\mu = -7\ [K^{-1}]$ is an empirical scaling factor which introduces a negative sign, and controls the relative weight of the MWI in the GDI formula (Gálvez and Davison 2016).

2.3.5 Inversion index (II)

The II aims to include the effects of trade wind inversions. Like the MWI, the II is an inhibition factor, producing negative values. The II considers the stabilizing effects of inversions and dry air entrainment, which act to inhibit convection. A stability factor (II_S) is calculated by taking the difference in temperature between 950 and 700 hPa, with lower values of II_S indicating stronger stabilization. To take dry air entrainment into account, the difference in θ_e between the layers A and B is considered, and a drying factor (II_D) is calculated. The lower and more negative II_D, the larger the decrease of θ_e with height, indicating the occurrence of dry air and subsidence, leading to inhibition of convection. A low II_S and II_D leads to a low value for II and represents an inhibition of convection and vice-versa. The II is calculated as follows:

$$II_S = T_{950} - T_{700} \qquad \text{Eq. (2.6)}$$

$$II_D = \theta_{e(B)} - \theta_{e(A)} \qquad \text{Eq. (2.7)}$$

$$II = \begin{cases} 0, & II_S + II_D > 0 \\ \sigma \times (II_S + II_D), & II_S + II_D \leq 0 \end{cases} \qquad \text{Eq. (2.8)}$$

where $\sigma = 1.5\ [K^{-1}]$ is an empirical factor to control the weight of the II in the GDI formula (Gálvez and Davison 2016).

2.3.6 Terrain correction (TC)

To improve visualization over higher terrain, a TC factor can be added, which may be calculated as follows:

$$TC = P_3 - \frac{P_2}{P_{SFC} - P_1} \qquad \text{Eq. (2.9)}$$

where $P_1 = 500\ [hPa]$, $P_2 = 9000\ [hPa]$, $P_3 = 18$ which are empirical constants, and P_{SFC} is the surface pressure (hPa) (Gálvez and Davison 2016). The TC was not included in the GDI calculation in this study since the study region only experienced relatively small spatial variations in topography from 12 to 25° E (e.g., Raghavendra et al. 2022). Furthermore, the mean surface pressure within the Congo Basin is ~ 960 hPa which results in a relatively small value of TC ≅ 1.5, and dynamic fields such as surface pressure show relatively little variability in the tropics especially for seasonal timescales. Therefore, neglecting the TC term has an insignificant impact on the results presented in this paper. To clarify, the TC term should be included if the analysis or forecast period is under two weeks especially at higher elevations.

2.3.7 Wind shear

Since the Coriolis parameter and the horizontal temperature gradient are small near the equator, dynamic–thermodynamic indices such as the Eady growth rate (e.g., Raghavendra and Milrad 2019) are of little use. However, dynamics such as wind shear should not be ignored when diagnosing thunderstorms since vertical wind shear influences the structure and organization of convective systems, as well as their evolution (Marion and Trapp 2019; Raghavendra et al. 2022). Vertical wind shear can organize convection into convective clusters and squall lines producing intense precipitation and extending the lifetime of convective systems (Robe and Emanuel 2001; Anber et al. 2014). Wind shear also advects moisture and temperature which impact thermodynamic stability (Robe and Emanuel 2001). Therefore, a relatively simple approach was used to calculate and analyze the vertical wind shear, i.e., $Wind\ shear = |\vec{V}_{500}| - |\vec{V}_{850}|$.

2.3.8 Trend analysis

To quantify long-term changes of thunderstorm activity over the Congo, seasonal trends and interannual variability of cold cloud fraction, the GDI and its sub-indices, and wind shear were calculated. The linear trend was estimated based on least square regression at both the grid and regional levels. The statistical significance (p-value) of the linear regression was evaluated using the two-tailed Student's test.

2.4 Results

2.4.1 More vigorous thunderstorms diagnosed by cold cloud top temperatures

In order to quantify changes in thunderstorm activity using satellite data, the cold cloud fraction (%) with T_b ranging between − 50 and − 70 °C was calculated. This served as a method to quantify intense thunderstorms over the Congo, as intense storms are characterized by $T_b < -50$ °C. Figure 2.1 a–d shows spatial patterns of the seasonal climatology and trends in cold cloud fraction, indicating an increase in cold cloud fraction over large parts of the study region for all seasons. The seasonal cycle can also be observed in Fig. 2.1 a–d. The north- and southward movement of the tropical rain belt is visible, as the tropical rain belt is characterized by enhanced convection and therefore higher percentages of cold cloud fraction. The green contours show the climatological values of the cold cloud fraction (%). The highest values, representing the tropical rain belt, are located south of the equator in DJF, and then shift northwards to the equator in MAM. In JJA, the highest values lie north of the equator in JJA, and then shift back south again during SON (Nicholson 2018).

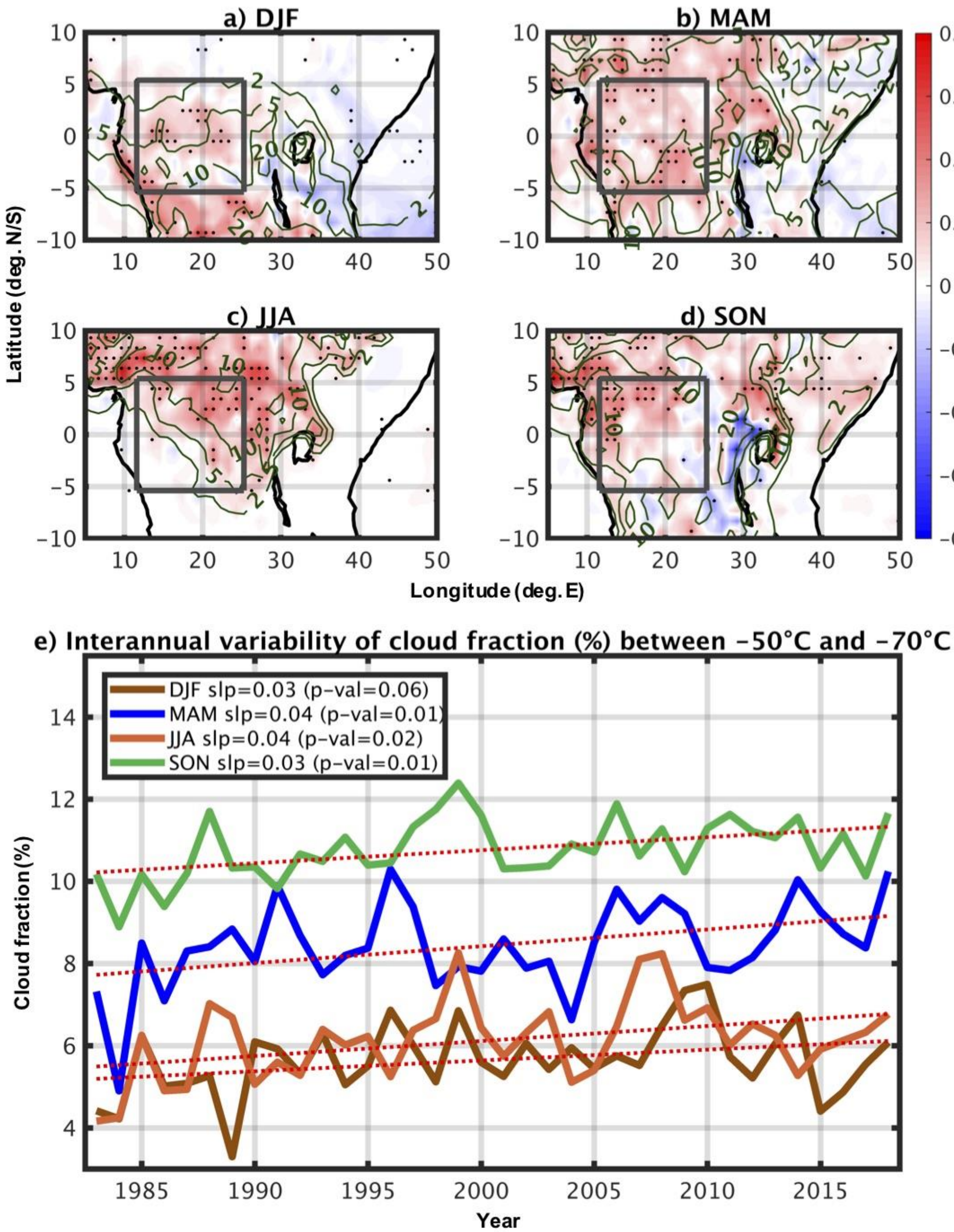

Figure 2.1: (**a**)-(**d**) Seasonal trends in cloud fraction (% yr^{-1}) for T_b between -50°C and -70°C at 15:00 UTC from 1983–2018. Gray boxes (5°N-5°S and 12°E-25°E) represent the Congo basin. Trends significant at $p < 0.05$ are shown using a black dot. The green lines show the climatological values of the cloud fraction (%) from 1983–2018. (**e**) Interannual variability and trends of the seasonal mean cloud fraction with T_b ranging from -50°C to -70°C at 15:00 UTC from 1983–2018 over the Congo basin.

2.4.2 Changes in GDI and its sub-indices

Seasonal trends in GDI show a significant increase over large parts of the Congo (Fig. 2.2a–d), with the GDI significantly increasing during all seasons (0.1–0.17 $year^{-1}$; $p < 0.10$). The largest increase of 0.17 $year^{-1}$ is detected in MAM and JJA, followed by SON with an increase of 0.12 $year^{-1}$, and DJF with the lowest increase of 0.1 $year^{-1}$ (Fig. 2.2e). This increase in GDI suggests a significant increase in thunderstorm activity over the Congo during all seasons, which is consistent with the trends detected in cold cloud fraction. Aiming to discover the physical mechanisms responsible for the increase in thunderstorm activity, the different sub-indices of the GDI were analyzed separately. First, the observed trends in the GDI sub-indices are presented, and later complimented by an explanation for each trend detected in the GDI.

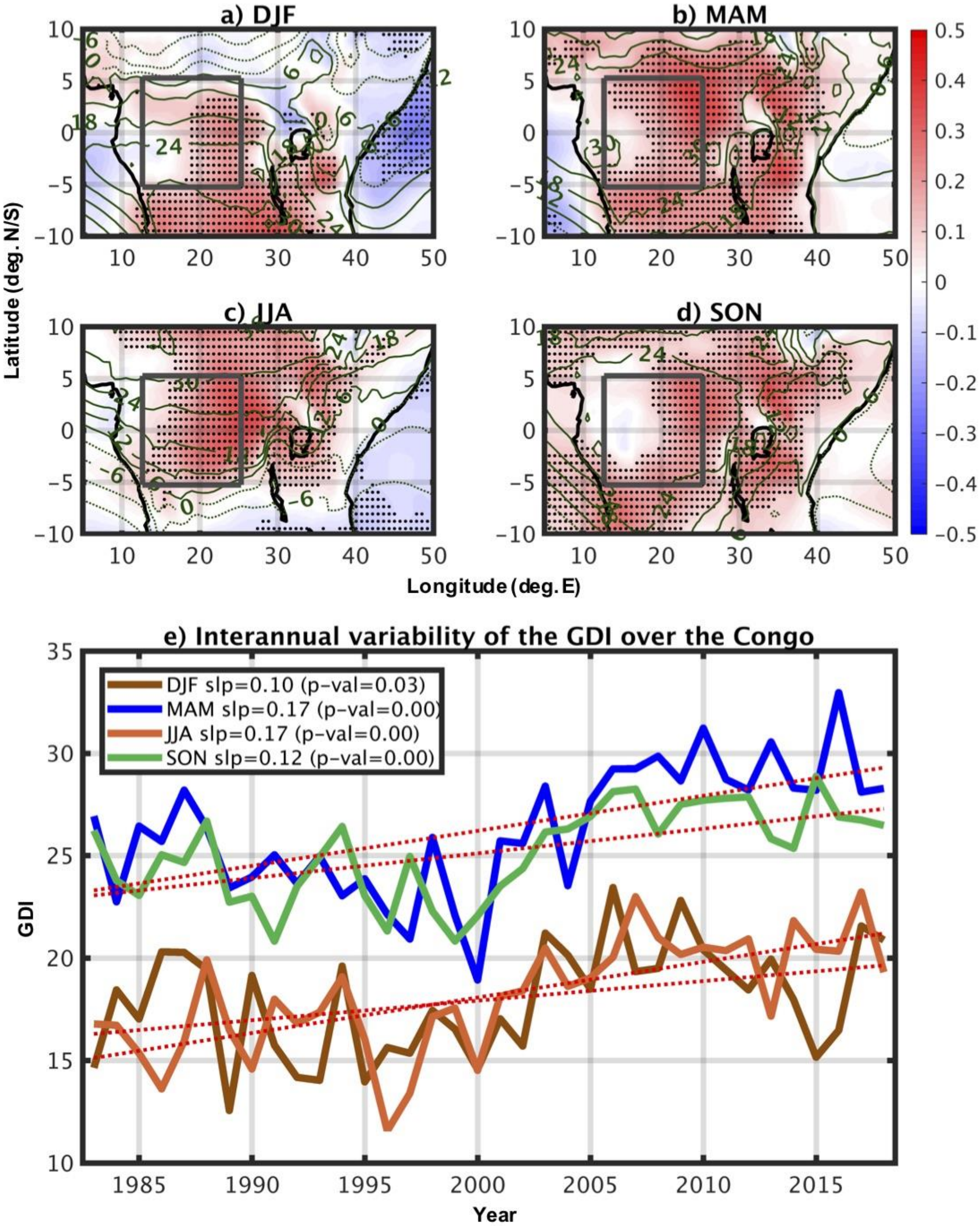

Figure 2.2: (**a**)-(**d**) Seasonal trends in GDI (GDI yr^{-1}) at 12:00 UTC from 1983–2018. Gray boxes (5°N-5°S and 12°E-25°E) represent the Congo basin. Trends significant at $p < 0.05$ are shown using a black dot. The green lines show the climatological values of the GDI from 1983–2018. (**e**) Interannual variability of the GDI at 12:00 UTC from 1983–2018 over the Congo basin.

The CBI shows a small but insignificant decrease over most of the Congo during all seasons (Fig. 2.3a–e). This leads to the conclusion that the interannual variability of the CBI does not contribute to the increase in thunderstorm activity. In contrast to that, the MWI is becoming weaker over most parts of the Congo, with the strongest and most significant trend in JJA, followed by MAM and SON, with DJF exhibiting the weakest trend (Fig. 2.4a–d). The interannual variability indicates a trend of 0.10 $year^{-1}$ ($p < 0.10$) in JJA, 0.09 $year^{-1}$ ($p < 0.10$) in MAM and 0.05 $year^{-1}$ ($p < 0.10$) in SON. The trend for DJF is not significant at $p < 0.10$ (Fig. 2.4e). Thus, the MWI likely contributes to the increasing thunderstorm activity in MAM, JJA and SON.

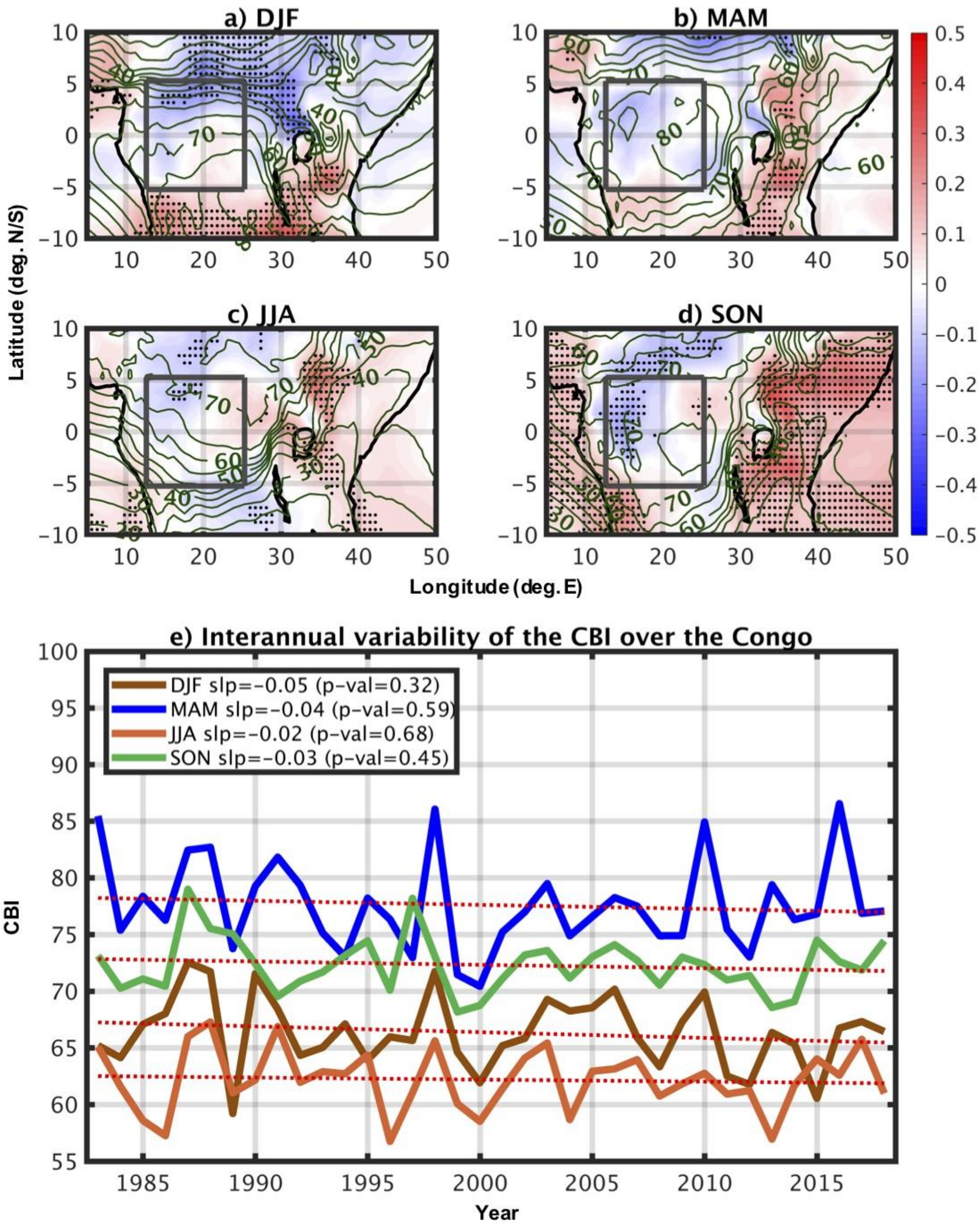

Figure 2.3: (**a**)-(**d**) Seasonal trends in CBI (CBI yr^{-1}) at 12:00 UTC from 1983–2018. Gray boxes (5°N-5°S and 12°E-25°E) represent the Congo basin. Trends significant at $p < 0.05$ are shown using a black dot. The green lines show the climatological values of the CBI from 1983–2018. (**e**) Interannual variability of the CBI at 12:00 UTC from 1983–2018 over the Congo basin.

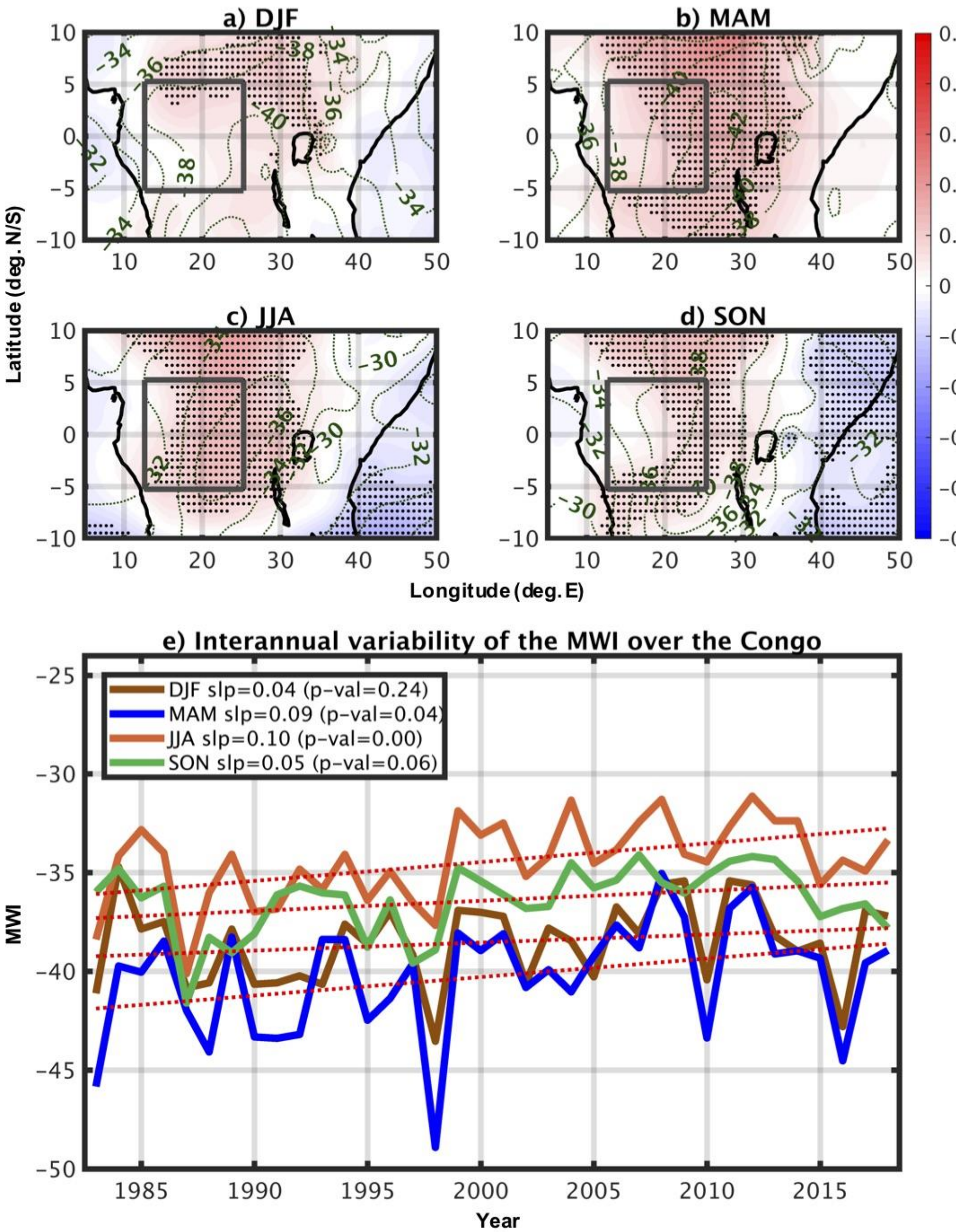

Figure 2.4: (**a**)-(**d**) Seasonal trends in MWI (MWI yr^{-1}) at 12:00 UTC from 1983–2018. Gray boxes (5°N-5°S and 12°E-25°E) represent the Congo basin. Trends significant at $p < 0.05$ are shown using a black dot. The green lines show the climatological values of the MWI from 1983–2018. (**e**) Interannual variability of the MWI at 12:00 UTC from 1983–2018 over the Congo basin.

The II is also becoming weaker during all seasons with significant trends in almost the entire study region (Fig. 2.5a–d). The interannual variability shows trends of 0.10–0.11 $year^{-1}$ ($p < 0.10$) during all seasons (Fig. 2.5e). Since the II is the sum of two terms i.e., II_D and II_S, these terms were also analyzed separately. The II_D became weaker over the entire study region (Fig. 2.6 a–d), and the linear trend in the II_D increased by 0.07–0.08 $year^{-1}$ ($p < 0.10$) during all seasons as well (Fig. 2.6e). A smaller II_D suggests that the θe gradient is decreasing with height and the entrainment of dry air over the inversion is becoming less frequent. This ultimately results in enhanced convection and thunderstorm activity (James and Markowski 2010). The II_S shows an increasing trend over most of the Congo Basin, and the interannual variability increased by 0.03–0.07 $year^{-1}$ (Fig. 2.7) depending on the season, with DJF exhibiting the largest increase, followed by MAM, JJA and SON. These findings indicate that the temperature gradient between 950 and 700 hPa is increasing, leading to a decrease in stability of the column and therefore supporting an increase in tropical convection.

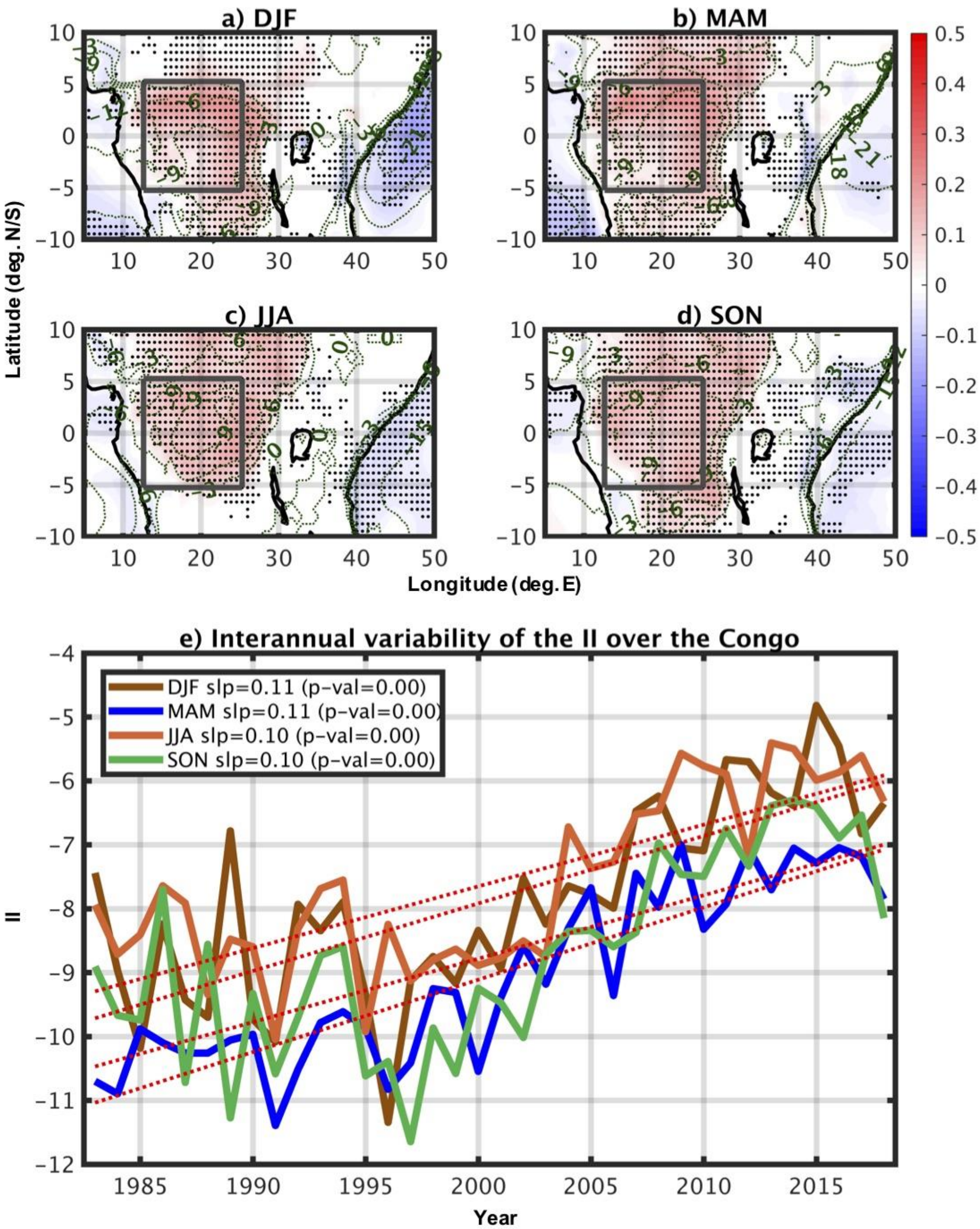

Figure 2.5: (**a**)-(**d**) Seasonal trends in II (II yr^{-1}) at 12:00 UTC from 1983–2018. Gray boxes (5°N-5°S and 12°E-25°E) represent the Congo basin. Trends significant at $p < 0.05$ are shown using a black dot. The green lines show the climatological values of the II from 1983–2018. (**e**) Interannual variability of the II at 12:00 UTC from 1983–2018 over the Congo basin.

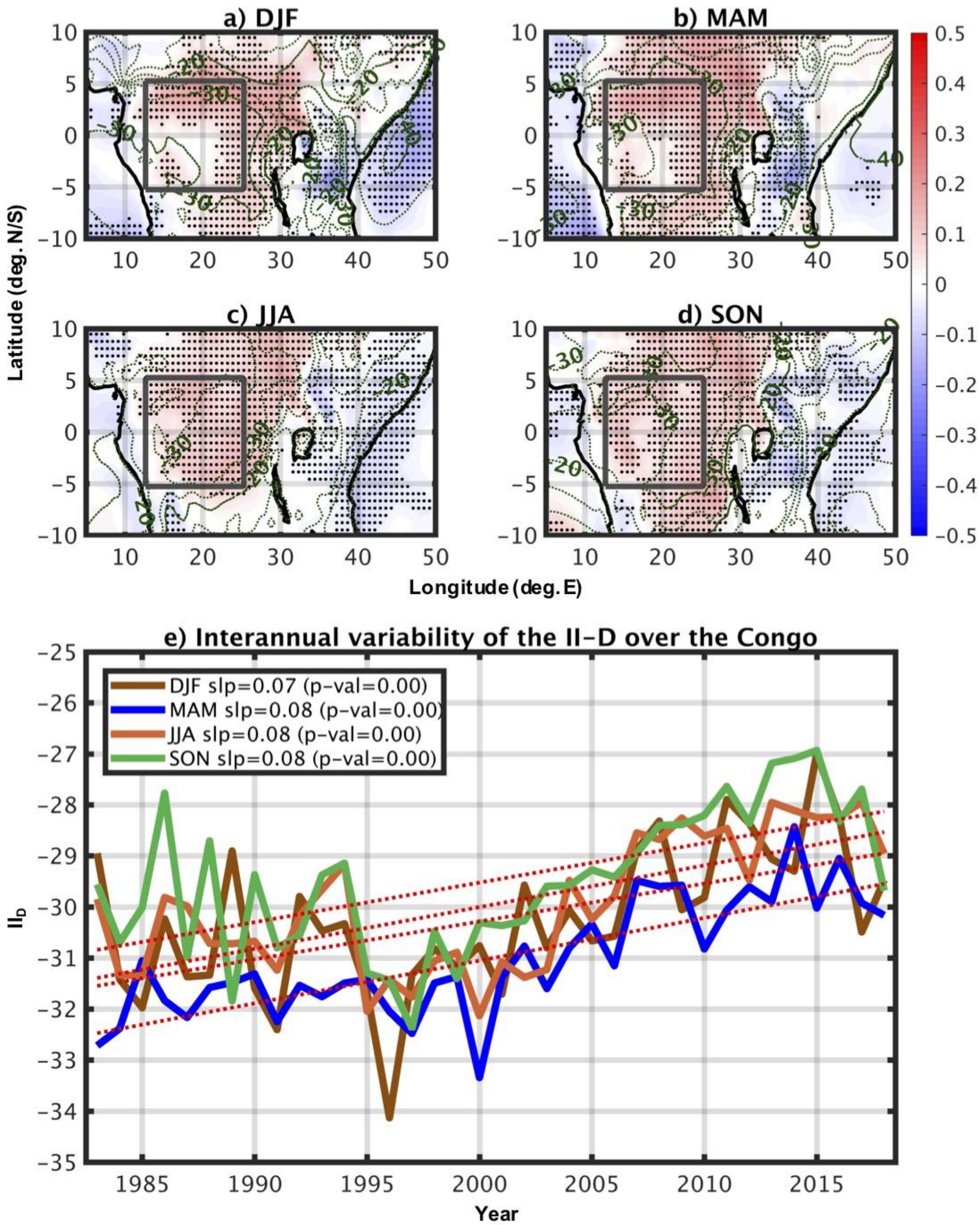

Figure 2.6: (**a**)-(**d**) Seasonal trends in II_D ($II_D\ yr^{-1}$) at 12:00 UTC from 1983–2018. Gray boxes (5°N-5°S and 12°E-25°E) represent the Congo basin. Trends significant at $p < 0.05$ are shown using a black dot. The green lines show the climatological values of the II_D from 1983–2018. (**e**) Interannual variability of the II_D at 12:00 UTC from 1983–2018 over the Congo basin.

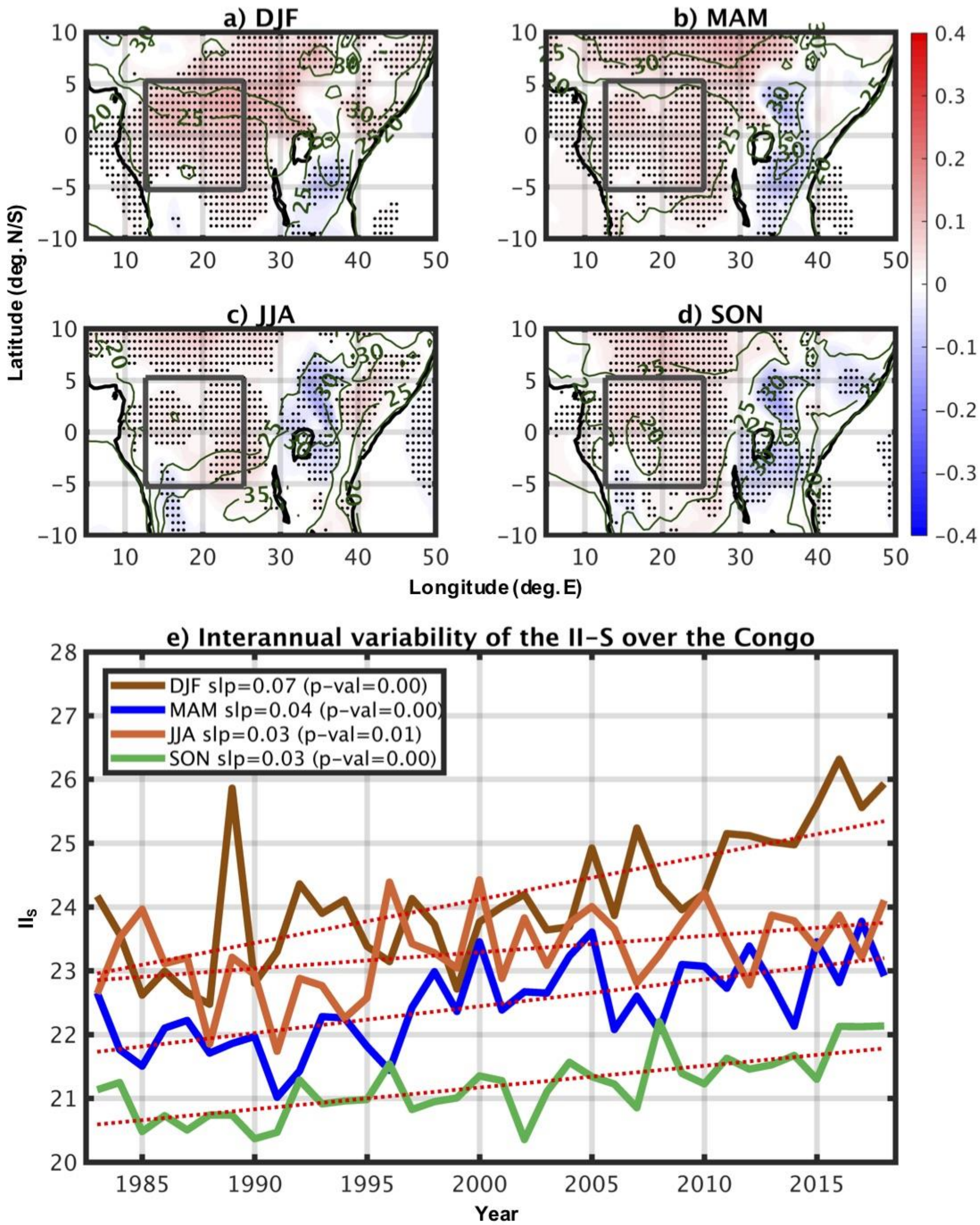

Figure 2.7: (**a**)-(**d**) Seasonal trends in II_S ($II_S\ yr^{-1}$) at 12:00 UTC from 1983–2018. Gray boxes (5°N-5°S and 12°E-25°E) represent the Congo basin. Trends significant at $p < 0.05$ are shown using a black dot. The green lines show the climatological values of the II_S from 1983–2018. (**e**) Interannual variability of the II_S at 12:00 UTC from 1983–2018 over the Congo basin.

2.4.3 Wind shear

Wind shear was found to be increasing significantly over the Congo during all seasons besides DJF. An increase of 0.03–0.07 ms^{-1} $year^{-1}$ ($p < 0.10$) is shown with the largest increase in SON, followed by JJA and MAM (Fig. 2.8). This presents an additional factor potentially contributing to the increase in thunderstorm activity since wind shear and orography significantly influence convection and precipitation over the Congo Basin. The unique African orography with the East African highlands and the Ethiopian highlands located in the northeast of the Congo modifies wind patterns by blocking tropical easterlies (zonal wind) and intensifying meridional wind around the mountain. This increase in wind shear potentially results in well-organized and intense thunderstorms over the Congo Basin (Marion and Trapp 2019; Raghavendra et al. 2022).

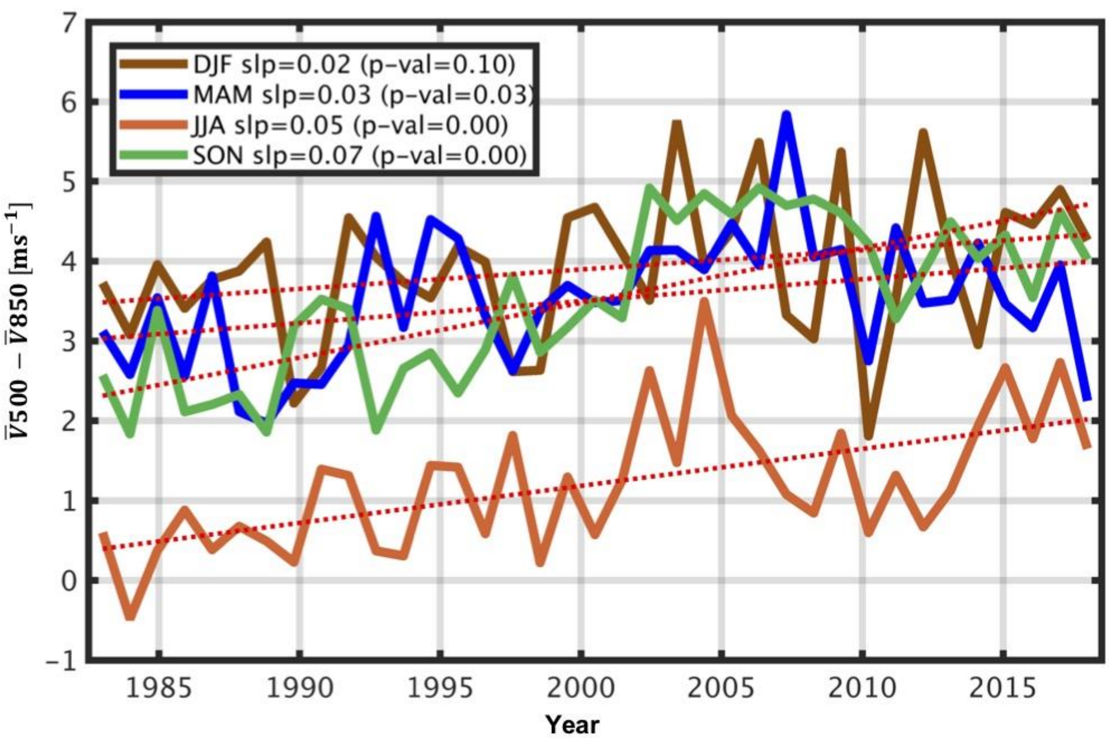

Figure 2.8: Interannual variability in wind shear between 500hPa and 850hPa (m/s yr^{-1}) at 12:00 UTC from 1983–2018 over the Congo basin.

2.5 Discussion and conclusion

In this study, thunderstorm activity over the Congo is analyzed using satellite-derived cold cloud top temperatures and the GDI including its sub-indices (CBI, MWI, and II). The GDI is a thermodynamic index developed to better diagnose tropical convection, with the CBI analyzing the availability of heat and moisture in the middle and lower troposphere, the MWI considering stabilizing and destabilizing effects of mid-level ridges and troughs, and the II considering entrainment of dry air and stabilization associated with trade wind inversions. The results show an increasing trend in convective activity over the Congo during all seasons from 1983 to 2018, which is consistent with previous findings indicating an increase in the extent and intensity of thunderstorms over equatorial Africa (e.g., Raghavendra et al. 2018; Taylor et al. 2018; Hart et al. 2019). The increase in thunderstorm activity is found to be the result of three processes: (1) a cooling of the 500 hPa temperature, which may be attributable to an increase in cold troughs, diagnosed using the MWI, (2) an increase in the temperature gradient between 700 and 950 hPa, diagnosed using the II_S, and (3) a decrease of the θ_e gradient with height indicating a decrease of dry air entrainment, diagnosed using the II_D. In addition, an increase in wind shear also appears to contribute to the increase in thunderstorm activity from March–November.

Notwithstanding uncertainties in both satellite and reanalysis datasets (Sect. 2.2.3), the trends of the GDI and its sub-indices are in good agreement with observations, including in-situ and satellite observations over the study region (e.g., Bush et al. 2020). The temperature profile over the study region (Fig. 2.9) shows the increase in the occurrence of cold troughs at 500 hPa diagnosed using the MWI, and the increase in the temperature gradient between 700 and 950 hPa diagnosed using the II_D. In addition, the relative humidity profile (Fig. 2.10) indicates a drying trend of the lower levels (i.e., Congo Basin) and a moistening of the upper levels. The θ_e profile over the study region is shown in Fig. 2.11 in order to evaluate the combined trends in temperature and moisture. The decrease of the θ_e gradient with height diagnosed using the II_D is associated with a decrease of θ_e in the lower troposphere (i.e., the Congo) and an increase of θ_e in the mid/upper troposphere, resulting mostly from a change in moisture (i.e., a decrease in moisture in the lower troposphere and an increase in the mid/upper troposphere) rather than a change in temperature (Soden et al. 2005; Su et al. 2006; Fu 2015; Bush et al. 2020).

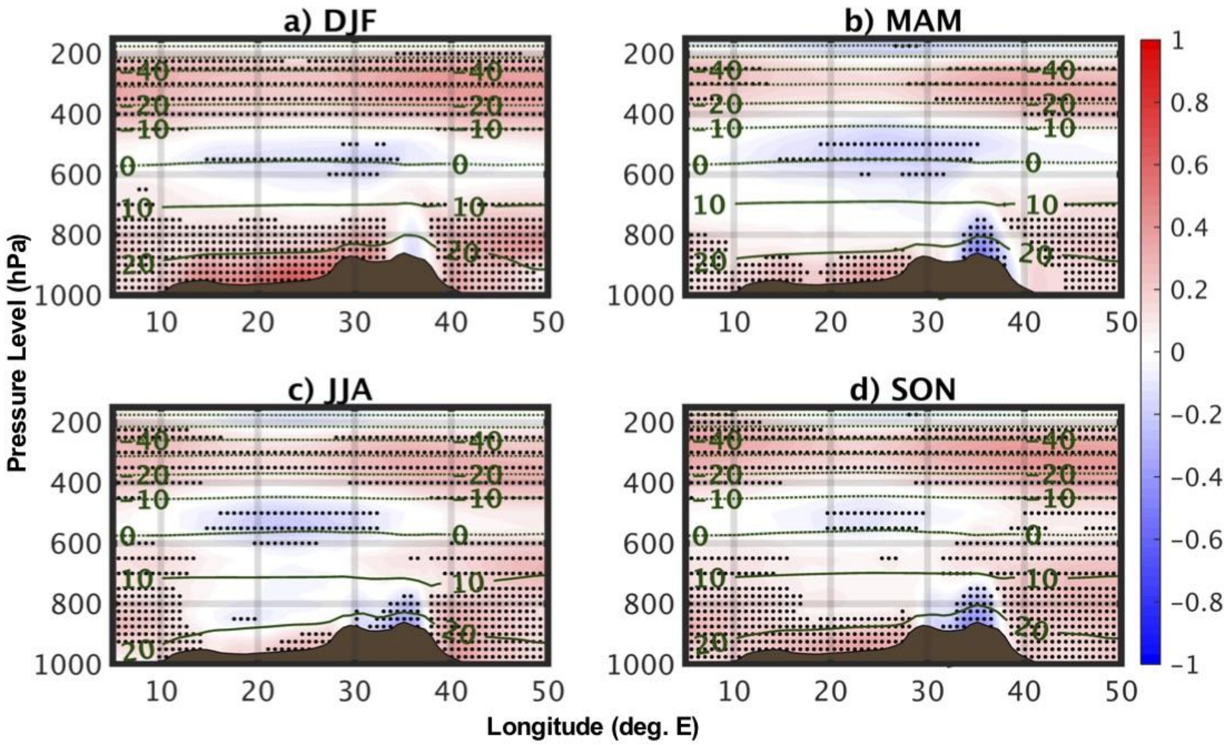

Figure 2.9: Seasonal trends in temperature (10^{-1} × °C yr^{-1}) at 12:00 UTC from 1983–2018. Trends significant at $p < 0.05$ are shown using a black dot. The green lines show the climatological values (°C) from 1983–2018.

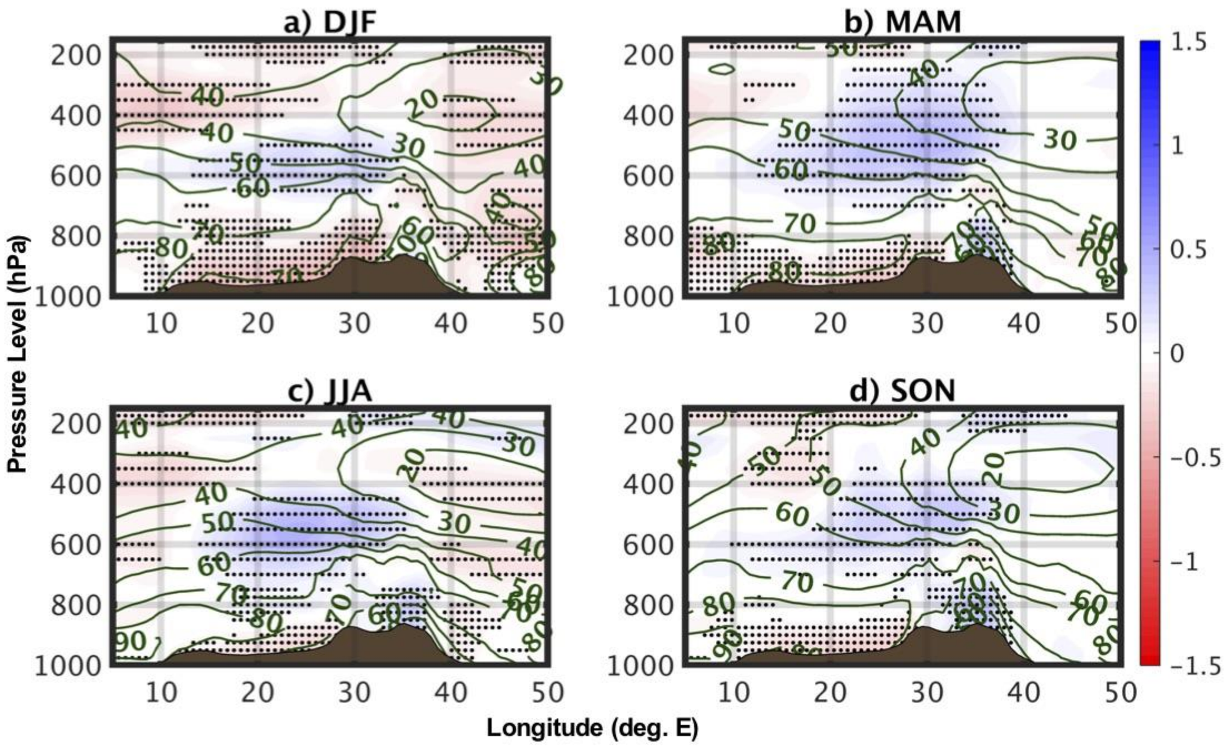

Figure 2.10: Seasonal trends in relative humidity (% yr^{-1}) at 12:00 UTC from 1983–2018. Trends significant at $p < 0.05$ are shown using a black dot. The green lines show the climatological values from 1983–2018.

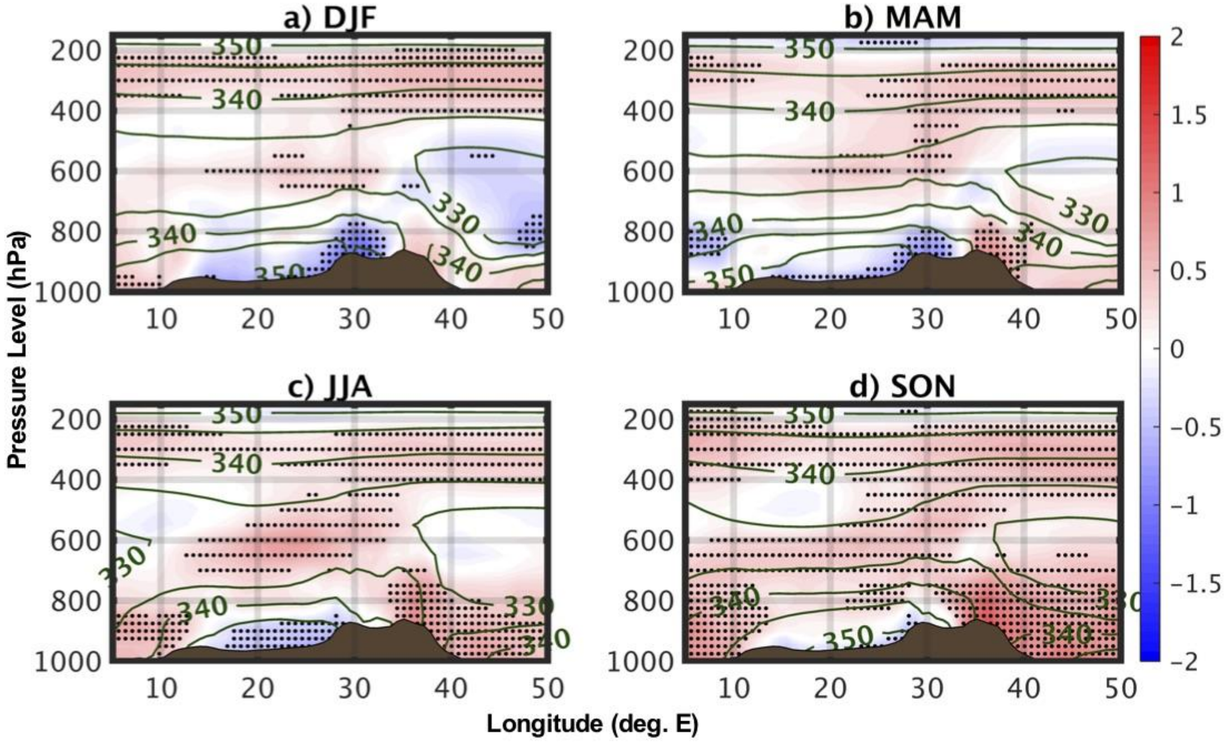

Figure 2.11: Seasonal trends in θ_e ($10^{-1} \times \mathrm{K}\ yr^{-1}$) at 12:00 UTC from 1983–2018. Trends significant at $p < 0.05$ are shown using a black dot. The green lines show the climatological values (K) from 1983–2018.

The frequent occurrence of cold troughs and cooling at 500 hPa may be a result of an increase in the occurrence of Kelvin waves over the Congo as detected by Raghavendra et al. (2019). An increase in the occurrence of Kelvin waves may lead to an increase in cold ridges at 500 hPa and thus also enhance deep convection over the Congo Basin (Sinclaire et al. 2015; Schlueter et al. 2019a, b). On the other hand, a decrease in the θ_e gradient with height may be the combined effect of two processes, a decrease in vegetation greenness and water content associated with droughts over the Congo, and vegetation greening over the East African highlands region (e.g. Hawinkel et al. 2016; Musau et al. 2018; Zhao et al. 2018). Moisture recycling is a crucial process in the tropical rainforests where evapotranspiration contributes substantially to regional precipitation (e.g. Dyer et al. 2017). The large-scale forest browning observed over the Congo, reducing evapotranspiration and decreasing rainfall (Zhou et al. 2014; Hua et al. 2016; Jiang et al. 2019), may reduce the regional moisture supply and thus dry the lower troposphere. The greening over the East African highlands potentially leads to a moistening of the air parcels over the highlands (Musau et al. 2018) before being advected over the Congo Basin by the easterly winds, moistening the air layers aloft the Congo. This could be one reason for the moistening of the mid-troposphere and a decrease in the θ_e gradient with height.

The drying trend in the lower levels (i.e., the Congo Basin) and moistening trend in the mid- and upper troposphere (Fig. 2.10) may also be the consequence of the increase in deep convection, transporting moisture upwards, drying the lower levels and moistening the mid/upper troposphere. This possibly causes an increase in deep convection, as the vertical gradient in θ_e is relaxed, which further destabilizes the vertical column and promotes a positive feedback mechanism resulting in taller and more intense thunderstorms. This hypothesis is complemented by previous works such as Soden and Fu (1995) and Zelinka and Hartmann (2009), showing that enhanced tropical convection in a warming climate is responsible for the increased upper-tropospheric relative humidity, with deep convection being the primary source of high clouds and free-tropospheric water vapor through moisture transport to the mid/upper troposphere. The upward transported moisture may then be advected away from the Congo by the poleward flow of the Hadley cell or easterly flow at higher altitudes (Byrne and Schneider 2016). This may possibly lead to less rainfall given the high water recycling ratio over the Congo (Dyer et al. 2017) and could potentially explain the decrease in rainfall detected over the Congo (e.g., Fu 2015; Raghavendra et al. 2018). Further, Figs. 2.9, 2.10, 2.11 suggest that the lifted condensation level (LCL) may have shifted to higher altitudes due to surface drying. Prein and Heymsfield (2020) showed that the melting height level and warm cloud depth has increased over the Congo, possibly affecting cloud microphysics and rainfall characteristics. This supports the hypothesis of a higher LCL, reducing the rainfall reaching the surface, and ultimately causing the drying trend over the Congo Basin as more water or ice particles falling out of a cloud may vaporize before reaching the ground (virga).

In summary, the increase in thunderstorm activity over the Congo Basin is found to be the result of a cooling of the 500 hPa temperature, an increase in the temperature gradient between 700 and 950 hPa, and a decrease of the θ_e gradient with height. The cooling of the 500 hPa temperature may be attributable to an increase in cold troughs, which is hypothesized to be the consequence of an increase in the occurrence of Kelvin waves over the Congo (e.g., Raghavendra et al. 2019). The decrease of the θ_e with height is shown to be the effect of a decrease in moisture in the lower levels and an increase in moisture in the mid and upper levels (Fig. 2.10). The decrease in moisture in the lower levels is assumed to be a direct effect of the drying trend over the Congo, while the moistening of the mid/upper levels is hypothesized to be a result of a greening and moistening of the East African Highlands (e.g., Musau et al. 2018), from where moist air is being advected over the Congo. Further, the upward transport of moist air during deep convection is hypothesized to additionally destabilize the column and enhance convective processes. The upward transported moisture potentially being advected away by the Hadley cell, and less rainfall reaching the surface due an elevation of the LCL and melting level likely result in a decreasing trend in rainfall and enhanced drying trend over the Congo.

Figure 2.12 summarizes the key findings of this work, including the observed changes in atmospheric temperature and moisture from 1983 to 2018 leading to the detected increase in thunderstorm activity (Fig. 2.12a, b), trends found in the GDI and its sub-indices including their impacts posed on atmospheric stability (Fig. 2.12c). It also includes a schematic of the proposed possible physical mechanisms, linking enhanced thunderstorm activity to the observed drying trend found over the Congo (Fig. 2.12d). In conclusion, thunderstorm activity over the Congo has increased, while rainfall has decreased significantly. The increasing trend in thunderstorm activity may be linked to an increase in the occurrence of cold troughs at 500 hPa, an increase of the temperature gradient between 700 and 950 hPa, and a decrease of the θ_e gradient with height. These mechanisms were also linked together in a positive feedback loop (Fig. 2.12d) which potentially explain the increase in thunderstorm activity and the decrease in surface rainfall and vegetation over the Congo. The enhanced convective activity likely moistens the mid/upper troposphere, and moisture may be transported away from the Congo Basin by the poleward flow of the Hadley cell and the tropical easterlies. This transport of moisture away from the Congo which is characterized by a large water recycling ratio could be one possible reason for the observed decrease in rainfall.

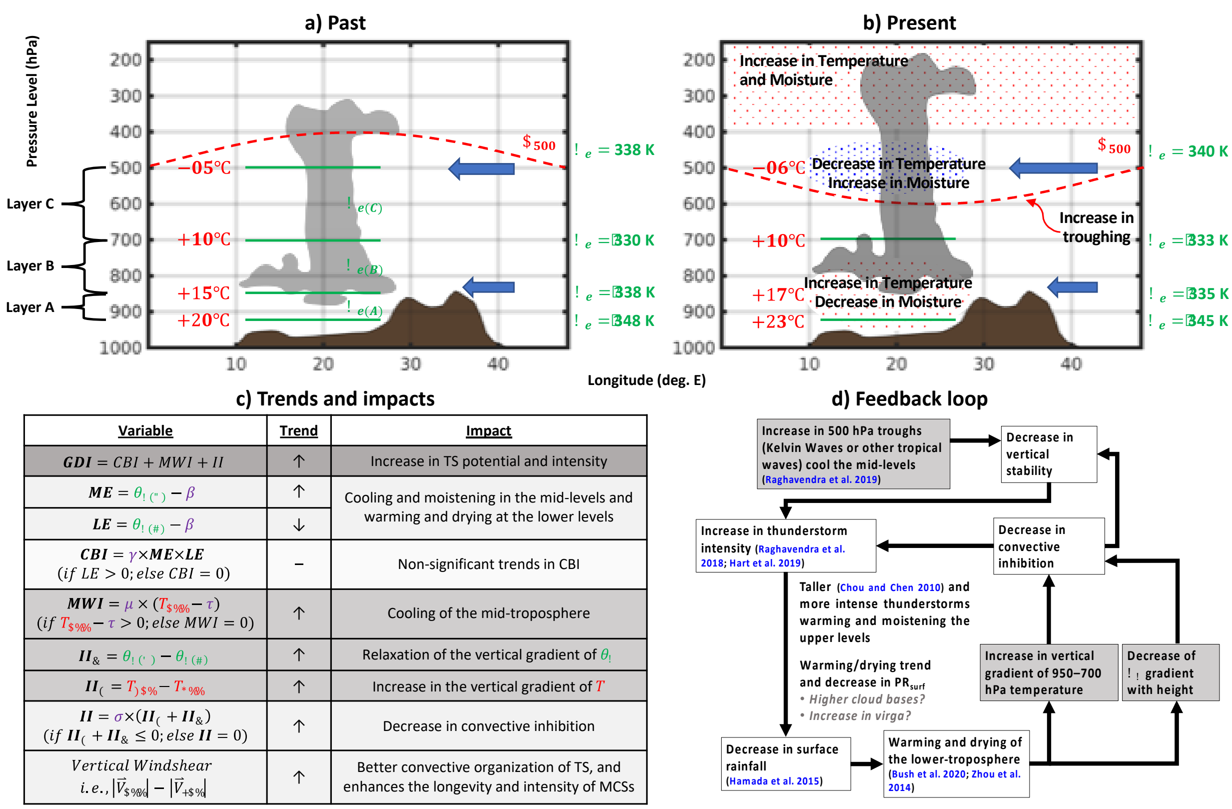

Figure 2.12: (**a–b**) Schematic of changes in temperature and moisture (diagnosed using the GDI) and wind shear from 1983–2018 leading to the observed increase in thunderstorm activity. (**c**) Diagnosed trends of the GDI and its sub-indices and their impacts on atmospheric temperature, moisture and stability. (**d**) Feedback loop of proposed factors leading to taller and more intense thunderstorms, in turn impacting atmospheric conditions and further enhancing deep convection.

From a future climate perspective, significantly more work is necessary to understand rainfall and vegetation characteristics over the Congo Basin. From an observations and historical climate standpoint, there is considerable spread in rainfall estimates amongst datasets (Washington et al. 2013). While studies such as Fotso-Nguemo et al. (2018) have shown the relatively well-known increases in heavy rainfall events in a warmer climate using GCMs for central Africa, the complex orography and overall uncertainties amongst GCMs over the Congo Basin is non-trivial (e.g., Haensler et al. 2013; Washington et al. 2013; Raghavendra et al. 2020; 2022). Therefore, the need for high-resolution regional climate models (e.g., Tamoffo et al. 2019) and convection allowing simulations (Stratton et al. 2018) are necessary to further expand our understanding of both the present and future climate for Africa (especially the Congo Basin).

Appendix A: Calculation of θ_e proxies for each layer from specific humidity and temperature, used to calculate the GDI

First, relative humidity (RH) was calculated at every level using specific humidity (q) and temperature (T) from the ERA-I dataset:

$$e^* = 6.112\, exp\left[\frac{17.76T}{T + 243.5}\right] \quad \text{Eq. (A1)}$$

$$q^* = 0.622\,\frac{e^*}{P} \quad \text{Eq. (A2)}$$

$$RH = \frac{q}{q^*} \times 100 \quad \text{Eq. (A3)}$$

where e^* is the saturated vapor pressure (hPa) and T is the temperature in °C (Bolton 1980). q^* is the saturation specific humidity and P is the atmospheric pressure (hPa) (Brock and Richardson 2001).

Potential temperature (θ; K) and mixing ratios (r; kg kg^{-1}) were then calculated for each layer using RH (Gálvez and Davison 2016).

Layer A:

$$\theta_A = \theta_{950} = T_{950}\left(\frac{1000}{950}\right)^{\frac{2}{7}} \quad \text{Eq. (A4)}$$

$$P_{ws_{950}} = 6.116441 \times 10^{\left[\frac{7.591386 \times T_{950}}{T_{950}+240.7263}\right]} \quad \text{Eq. (A5)}$$

$$P_{w_{950}} = Pws_{950} \times \frac{RH_{950}}{100} \quad \text{Eq. (A6)}$$

$$r_A = \frac{621.9907}{1000} \times \frac{Pw_{950}}{950 - Pw_{950}} \quad \text{Eq. (A7)}$$

Layer B:

$$\theta_B = 0.5(\theta_{850} + \theta_{700})$$

$$= 0.5\left[T_{850}\left(\frac{1000}{850}\right)^{\frac{2}{7}} + T_{700}\left(\frac{1000}{700}\right)^{\frac{2}{7}}\right] \quad \text{Eq. (A8)}$$

$$P_{ws_{850}} = 6.116441 \times 10^{\left[\frac{7.591386 \times T_{850}}{T_{850}+240.7263}\right]} \quad \text{Eq. (A9)}$$

$$P_{ws_{700}} = 6.116441 \times 10^{\left[\frac{7.591386 \times T_{700}}{T_{700}+240.7263}\right]}$$ Eq. (A10)

$$P_{w_{850}} = Pws_{850} \times \frac{RH_{850}}{100}$$ Eq. (A11)

$$P_{w_{700}} = Pws_{700} \times \frac{RH_{700}}{100}$$ Eq. (A12)

$$r_{850} = \frac{621.9907}{1000} \times \frac{Pw_{850}}{850 - Pw_{850}}$$ Eq. (A13)

$$r_{700} = \frac{621.9907}{1000} \times \frac{Pw_{700}}{700 - Pw_{700}}$$ Eq. (A14)

$$r_B = 0.5(r_{850} + r_{700})$$ Eq. (A15)

Layer C:

$$\theta_C = \theta_{500} = T_{500}\left(\frac{1000}{500}\right)^{\frac{2}{7}}$$ Eq. (A16)

$$P_{ws_{500}} = 6.116441 \times 10^{\left[\frac{7.591386 \times T_{500}}{T_{500}+240.7263}\right]}$$ Eq. (A17)

$$P_{w_{500}} = Pws_{500} \times \frac{RH_{500}}{100}$$ Eq. (A18)

$$r_C = \frac{621.9907}{1000} \times \frac{Pw_{500}}{500 - Pw_{500}}$$ Eq. (A19)

where P_{ws} = saturation vapor pressure, P_w = partial pressure of water vapor (Gálvez and Davison 2016).

The θ_e was then calculated, where the following formula from Betts and Dugan (1973), simplified by Bolton (1980) was chosen since the calculation for θ_e is non-trivial:

$$\theta_e = \theta \exp(\frac{L_o r}{C_{pd} T_{LCL}}) \qquad \text{Eq. (A20)}$$

where $L_o = 2.69\ x\ 10^6\ J\ kg^{-1}$ is the latent heat of vaporization, $C_{pd} = 1005.7\ J\ kg^{-1} K^{-1}$ is the specific heat of dry air at constant pressure, and T_{LCL} is the temperature in K at the lifted condensation level LCL.

T_{LCL} was then replaced by the 850hPa temperature (K) to work around the complex calculation for T_{LCL}, which results in the following calculation of θ_e used to calculate the GDI:

$$\theta_e = \theta \exp\left(\frac{L_o r}{C_{pd} T_{850}}\right) \qquad \text{Eq. (A21)}$$

Gálvez and Davison (2016) tested replacing T_{LCL} by the 850hPa temperature and only found very small differences on the final GDI values. Therefore, this simplification was used in this study as well.

For each layer, θ_e proxies are then calculated using Eq. A21:

Layer A: $$\theta_{e(A)} = \theta_A \exp \frac{L_o r_A}{C_{pd} T_{850}}$$ Eq. (A22)

Layer B: $$\theta_{e(B)} = \theta_B \exp \frac{L_o r_B}{C_{pd} T_{850}} + \propto$$ Eq. (A23)

Layer C: $$\theta_{e(C)} = \theta_C \exp \frac{L_o r_C}{C_{pd} T_{850}} + \propto$$ Eq. (A24)

where $\propto = -10\ (K)$ is an empirical adjustment constant aiming to limit excessive GDI values in regions with plentiful moisture at and above 850hPa (Gálvez and Davison 2016).

CRediT authorship contribution statement:

Kathrin Alber: Conceptualization, Methodology, Software, Validation, Formal analysis, Investigation, Data Curation, Writing – Original Draft, Visualization. **Ajay Raghavendra:** Conceptualization, Methodology, Data Curation, Writing – Review & Editing. **Liming Zhou:** Supervision, Conceptualization, Writing – Review & Editing, Funding acquisition. **Yan Jiang:** Methodology, Software, Writing – Review & Editing. **Heather Sussman:** Formal Analysis, Methodology, Writing – Review & Editing. **Stephen Solimine:** Data Curation, Writing – Review & Editing

CHAPTER 3:

A shift in the diurnal timing and intensity of deep convection over the Congo Basin during the past 40 years

This chapter addresses question 2) in section 1.3 by analyzing GridSat-B1 and MODIS satellite datasets in conjunction with ERA5 reanalysis data. Diurnal variations of cloudiness and deep convection from 1979 to 2019 were investigated during all four seasons. Additionally, connections with the warming and drying trend observed over the region are explored, where associations with trends in precipitation efficiency and connections to the observed decrease in precipitation were evaluated. The hypothesis of this study includes that the amplitude of deep convection has increased as a result of a decrease of clouds in the morning, and more vigorous convection in the afternoon. These changes are hypothesized to be associated with the observed drying trend over the Congo.

3.1 Introduction

The diurnal cycle is one of the most fundamental modes of atmospheric variability attributable to large variations in the solar forcing over the course of the day (Yang and Slingo 2001). For the rainfall in the tropics, the maximum is reached during the mid- to late afternoon over land and at nighttime over oceans. The maximum rainfall in the afternoon over land is a result of surface solar heating during the day, destabilizing the atmosphere and subsequently encouraging the onset of convection (Yang and Smith 2006). Over most tropical land areas, mornings are relatively clear, followed by a rapid afternoon buildup of convective clouds associated with a maximum in rainfall and a more gradual decay of clouds during the night (Garreaud and Wallace 1997). Using water vapor absorption band radiance data from geostationary satellites, Soden (2000) found significant diurnal variations in the upper tropospheric relative humidity in the tropics over both land and oceans, where the variations over land are out of phase with those over the oceans. Tian et al. (2004) showed large diurnal variations in deep convection, precipitation, and high clouds over deep convective regions. They indicated that upper tropospheric relative humidity peaks around midnight over the oceans and at 03:00 local solar time (LST) over land, with stronger diurnal variations of deep convection over land, which maximizes in the late afternoon and early evening hours.

Central Africa is a hotspot for thunderstorms and one of the most convective regions in the world, characterized by intense thunderstorm activity (Zipser et al. 2006). The Congo Basin, situated in Equatorial Central Africa, is home to the Congo rainforest, the second largest rainforest in the world. Naturally, thunderstorm activity over the Congo is largely influenced by the diurnal cycle, with a morning minimum and a peak in convection and convective rainfall in the late afternoon between 16:00 and 19:00 LST (Yang and Slingo 2001; Jackson et al. 2009). As most precipitation over the tropics stems from convection (Dai, 2006), the majority of the Congo rainfall originates from deep convection and mesoscale convective systems (MCSs) (Jackson et al. 2009). However, although the Congo experiences some of the most intense thunderstorms and a higher lightning flash rate compared to other tropical regions (Washington et al. 2013), it receives less precipitation than other equatorial regions like Amazonia or the Indonesian maritime continent. Additionally, surface temperatures in Africa have been rising and are projected to further increase (James and Washington 2013; Engelbrecht et al. 2015). Furthermore, studies found that the Congo has experienced a large-scale and long-term drying trend, associated with an increase in dry season length (Jiang et al. 2019) and a decrease in mean precipitation since the 1980s (Zhou et al. 2014; Hua et al. 2016, Hua et al. 2018). Counterintuitively, the number, intensity and size of thunderstorms over the Congo have increased (Raghavendra et al. 2018; Alber et al. 2021a) despite the decreasing rainfall trend. Hamada et al. (2015) explained this relationship by showing a weak linkage between heavy rainfall and tall thunderstorms, arguing that the tallest thunderstorms do not necessarily produce the most intense rainfall events.

As large parts of the tropical cloudiness and rainfall can be explained by the diurnal cycle (Yang and Slingo 2001), which is mainly controlled by surface heating, one important question is whether the long-term drought may has modified the diurnal cycle of clouds and deep convection over the Congo. Identifying the diurnal changes in clouds and deep convection over the region promises to enhance our understanding of rainfall patterns and variability as well as associated thunderstorm activity, and may thereby help to reconcile the observed inverse trends in deep convection and rainfall. The goals of this study therefore are to analyze the diurnal cycle of deep convection over the Congo, to investigate its changes from 1979 to 2019, and to ultimately link the changes found in the diurnal cycle of deep convection to the observed decrease in precipitation. The data used is presented in section 3.2 and the methods are described in section 3.3. In section 3.4 we present our results followed by a summary in section 3.5.

3.2 Data

The study domain is the Congo Basin, defined as the area from 5°N to 5°S and 12°E to 30°E. Four datasets were used in this study, 1) the Gridded Satellite (GridSat-B1) (Knapp 2008; Knapp et al. 2011), 2) MODerate Resolution Imaging Spectroradiometer (MODIS) (Wan et al. 2015a; Wan et al. 2015b), 3) ERA5 reanalysis (Hersbach et al. 2020), and 4) NOAA Climate Prediction Center Precipitation data (CPC) (Sun et al. 2018). All seasons, i.e., December, January, February (DJF), March, April, May (MAM), June, July, August (JJA), and September, October, November (SON) were investigated. MAM and SON are the two wet seasons while DJF and JJA are the two dry seasons receiving lower amounts of precipitation (Pokam et al. 2012; Dyer et al.

2017) as a result of the seasonal shift of the tropical rain belt (Nicholson 2018). All times of day are indicated in West Africa Standard Time (GMT +1).

3.2.1 GridSat-B1 satellite data

Climate Data Record quality (NRC, 2004) infrared (IR) channel (11 μm) T_b data sampled by the European Meteorological (MET) series of geostationary satellites from the International Satellite Cloud Climatology Project (ISCCP; Schiffer and Rossow 1983) was used in this study. The GridSat-B1 T_b data is available at a 0.07° × 0.07° spatial and 3-hourly temporal resolution (Knapp 2008; Knapp et al. 2011). While the maximum time span available from the GridSat-B1 dataset is from 1981 to present, only the years from 1985 to 2019 were utilized here because of high frequencies of missing data between 1982 and 1985 (Raghavendra et al. 2020). As the atmosphere is almost transparent at 11 μm, the satellite measured radiance was used to derive T_b for cloud top (cloudy-sky) or surface (clear-sky) temperatures.

3.2.2 MODIS land surface temperature satellite data

MODIS land surface temperature from both Aqua (Wan et al. 2015a) and Terra (Wan et al. 2015b) satellites was further incorporated in this study. The Aqua and Terra satellites are equipped with the MODIS instruments and image the Earth's surface in 36 spectral bands between 0.405 and 14.385 μm at three spatial resolutions (250 m, 500 m, 1000 m). Terra passes the equator at 10:30 and 22:30 LST, and Aqua passes the equator at 01:30 and 13:30 LST. The MODIS land surface temperature from 2003 to 2019 was obtained from NASA's Land Processes Distributed Active Archive Center (LP DAAC) (e4ftl01.cr.usgs.gov). The MODIS tiles h19v08, h19v09, h20v08 and h20v09, covering the spatial area 10°N to 10°S and 10°E to 30°E, were remapped to 5°N to 5°S and 12°E to 30°E to match the study region. Since daily data often contains missing values, the 8-day composites at 1 km resolution from collection 6 were used (Aqua: MYD11A2;

Terra: MOD11A2), providing the best quality clear-sky (cloud-free) land surface temperature measurements from each 8-day period.

3.2.3 ERA5 reanalysis data

The ERA5 dataset (Hersbach et al. 2020) was used to obtain several variables for the time span from 1979 to 2019 at a $0.25° \times 0.25°$ spatial resolution, i.e., 2-m temperature (T2m), 2-m dew point (D2m), precipitation, cloud base height, and total column water. Additionally, specific humidity and temperature at 4 different pressure levels (i.e., 950 hPa, 850 hPa, 700 hPa and 500 hPa) were used. The time period 1979–2019 was chosen to maximize the temporal coverage. Although the same time period as used for the GridSat-B1 (1985–2019) could have been chosen instead, the results do not change significantly if using the shorter time period. All variables besides precipitation and total column water were obtained at a 3-hourly temporal resolution to match the satellite acquisition times of the GridSat-B1 T_b to ensure the consistency between observed and reanalysis data in terms of temporal resolution. Precipitation and total column water were utilized at a 1-hourly resolution to calculate precipitation efficiency. The ERA5 total column water is defined as the total amount of water including vapor, cloud water and cloud ice, integrated vertically from the ground to the nominal top of the atmosphere. Further, the ERA5 cloud base height, the height above surface of the base of the lowest layer of clouds, is defined as the height of the lowest level with a cloud fraction greater than 1% and a condensate content greater than 1×10^{-6} kg kg^{-1}, where the lowest model layer is not utilized to exclude fog. The temperature and specific humidity at the four pressure levels were utilized to calculate the Gálvez-Davison Index (see section 3.3.2), and the T2m and D2m served to retrieve the 2-m relative humidity (RH2m) using the improved Magnus formula (Alduchov and Eskridge 1996). The ERA5 precipitation is provided by the Global Precipitation Climatology Project (GPCP) based on satellite data and the Global Precipitation Climatology Centre (GPCC) which also includes rain-gauge observations.

Although other reanalysis products could have been utilized for this analysis, it is difficult to identify the most accurate dataset over the Congo Basin due to the extremely limited surface observations such as gauge stations and radiosonde networks. However, Hua et al. (2019) showed that the bias and root-mean-square error associated with the ERA-Interim reanalysis dataset is comparable to other reanalysis products, and Gleixner et al. (2020) found that the ERA5 matched the observations over Africa even better than the ERA-Interim data. Therefore, the ERA5 dataset was decided to be appropriate for this study.

3.2.4 CPC precipitation data

To compare ERA5 hourly reanalysis precipitation to daily gauge-based products, the NOAA Climate Prediction Center (CPC) global unified gauge-based daily precipitation was further used, where gauge observations were merged with satellite derived data (Sun et al. 2018). The dataset was provided by the NOAA/OAR/ESRL PSL and was obtained online (psl.noaa.gov/) at a 0.5° × 0.5° spatial resolution.

3.3 Methods

3.3.1 Thunderstorm and cloud detection

To detect thunderstorm activity, the GridSat-B1 data was used and the fraction of pixels with T_b lower than −50 °C (e.g., Alber et al. 2021a) within each 0.07° × 0.07° grid over the study domain was estimated from the GridSat-B1 data. The fraction of pixels with T_b lower than −50 °C was defined as cold cloud fraction (CCF). Since deep tropical convection is characterized by lower values of T_b, the CCF was used to represent areas in which deep convection occurs (Taylor et al. 2017; Hart et al. 2019). To detect the total cloud fraction (TCF), the fraction of pixels with T_b lower than +10 °C within each 0.07° × 0.07° grid was further calculated. The TCF was used to estimate the amount of all cloud types, including mid- to low-level clouds. Although the threshold +10 °C was used for this study, other thresholds (i.e., 0 °C, +5 °C, +15 °C) have been tested as well and showed similar results.

3.3.2 Gálvez-Davison Index

To measure the thunderstorm potential over the region, the Gálvez-Davison Index (GDI) was used (e.g., Alber et al. 2021a). The GDI is a thermodynamic index, developed by Michael Davison and José Gálvez at NOAA's Weather Prediction Center (WPC). This index can forecast convection in the tropics more accurately than traditional indices by focusing on thermodynamic processes rather than dynamical processes. The GDI, a unitless parameter, is used diagnostically, where higher values indicate a higher potential for thunderstorms. To calculate the GDI, temperature and specific humidity values are needed at four different levels, i.e., at 950 hPa, 850 hPa, 700 hPa, and 500 hPa (Gálvez and Davison 2016). In this study, ERA5 temperature and specific humidity data at these levels were used at a 3-hourly resolution for the GDI calculation. A complete derivation and explanation of the GDI is presented in Gálvez and Davison (2016) and Alber et al. (2021a).

3.3.3 Precipitation efficiency

Precipitation efficiency was used to evaluate how efficiently the convective systems produce precipitation by measuring how much of the water condensing in a rising column of air eventually reaches the surface as precipitation (Lau and Wu 2003; Sui et al. 2007; Lutsko and Cronin 2018). While there are numerous techniques to calculate precipitation efficiency, in this study the ratio between rainfall and total column water was used to estimate the precipitation efficiency. More specifically, the hourly ERA5 precipitation values were summed up to daily total precipitation, and the daily average ERA5 total column water was calculated from the hourly total column water.

To determine the precipitation efficiency, the total daily precipitation was divided by the daily average total column water (Sellers 1965; Market et al. 2003).

3.3.4 Diurnal cycle analysis

The seasonally averaged diurnal cycles were calculated for T2m, RH2m, and cloud base height from the ERA5 dataset for the years 1979–2019, and for T_b, CCF and TCF from the GridSat-B1 product for the years 1985–2019. Temporal changes of the diurnal cycles of T_b, CCF, TCF, T2m, RH2m, cloud base height, and GDI were analyzed by comparing the averages and 95% confidence intervals of two groups with different time periods. The first group was calculated by averaging over the first third of the time span analyzed, i.e., 1985–1996, while the second group represented the average of the last third of the time span analyzed, i.e., 2008–2019. This method helped to analyze changes in the diurnal cycle by determining if the 95% confidence interval of first third is significantly different from the 95% confidence interval of the last third, where the 95% confidence intervals were determined by multiplying the standard error with the 95% probability intervals of the t-distribution at each timestep. The diurnal cycles were calculated using a 3–24-hour spectral filter. The discrete Fourier transform (DFT) was applied to the anomaly data using a fast Fourier transform (FFT) in order to extract the diurnal cycles (e.g., Frigo and Johnson 1998, Frigo and Johnson 2005; Tian et al. 2004). To do so, the 3-hourly data was first interpolated to 1-hourly resolution by applying the spline interpolation method to acquire more datapoints for a more detailed analysis and to prevent spectral aliasing by using a 3-hour filter. This interpolation of the 3-hourly to 1-hourly data may introduce some uncertainties associated with indicating specific hours of the day after interpolating. Additionally, since thunderstorms over the Congo Basin normally propagate from the East African Highlands westwards over the Congo Basin, the time of peak convection (e.g., highest percentage of CCF) is earlier in the eastern parts of the study domain compared to the western areas. As time averages over the whole domain were used for this study, the peak times of CCF deviate slightly from the indicated values depending on the region.

The diurnal T_b amplitude was further obtained by subtracting the values averaged over 12:00–13:00 LST from the values averaged over 18:00–19:00 LST, where 12:00–13:00 LST is the time of maximum T_b or minimum convection, and the values at 18:00–19:00 LST represent the lowest T_b values when the CCF is highest, and convection is deepest. The diurnal T2m amplitude was calculated by subtracting the values averaged over 04:00–06:00 LST, i.e., the time of minimum T2m, from the values averaged over 13:00–15:00 LST, i.e., the time of maximum T2m. To calculate the diurnal MODIS land surface temperature amplitude, the MODIS data was interpolated to 2-hourly data since the equator passing times of Aqua and Terra are not ideal to calculate the diurnal land surface temperature amplitude and the available times do not match the times used to calculate the T2m ERA5 amplitude. After interpolating the dataset, the values at 05:30 LST and the values averaged over 13:30 and 15:30 LST (i.e., 14:30 LST) were chosen to calculate the diurnal land surface temperature amplitude.

3.3.5 Trend analysis

The linear trends of the ERA5 and CPC precipitation, ERA5 precipitation efficiency, and the diurnal amplitudes of the GridSat-B1 T_b, MODIS land surface temperature and ERA5 T2m were determined in order to identify changes of the different variables. Linear trends were calculated based on least squares regression and the statistical significance (p-value) of the linear regression was evaluated using the two-tailed Student's t-test.

3.4 Results

The seasonally averaged diurnal T_b cycles in Fig. 3.1a show generally higher T_b values during the two dry seasons and lower values during the two wet seasons. The T_b is highest at 12:00

LST during SON (1.2 °C), and at 13:00 LST during DJF (4.8 °C), MAM (2.3 °C), and JJA (7.0 °C), while it is lowest at 20:00 LST during JJA (−3.3 °C) and SON (−11.3 °C), at 21:00 LST during MAM (−11.2 °C), and at 03:00 LST during DJF (−6.3 °C). Fig. 3.1b is similar to Fig. 3.1a but for the CCF, with a maximum at 18:00 LST during JJA (9.0%) and SON (16.7%), and at 19:00 LST during DJF (10.3%) and MAM (16.8%). The lowest percentage of CCF is recorded at 11:00 LST during SON (3.1%), and at 12:00 LST during DJF (2.3%), MAM (3.3%) and JJA (1.5%). The CCF is generally higher during the two wet seasons than the two dry seasons. Fig. 3.1c shows a minimum in TCF at 13:00 LST during JJA (39.6%), and at 14:00 LST during DJF (44.6%), MAM (50.0%) and SON (52.2%), while the maximum is at 04:00 LST during all seasons (68.5% for DJF; 75.2% for MAM; 60.2% for JJA; 77.6% for SON). Overall, the highest T_b values at 12:00–13:00 LST and the lowest TCF values at 13:00–14:00 LST indicate a minimum in cloud cover around noon and in the early afternoon, while the maximum in CCF at 18:00–19:00 LST suggests that convection is deepest around sunset. Consequently, the minimum in the diurnal cycle of deep convection and convective rainfall is recorded right after noon and the maximum around sunset.

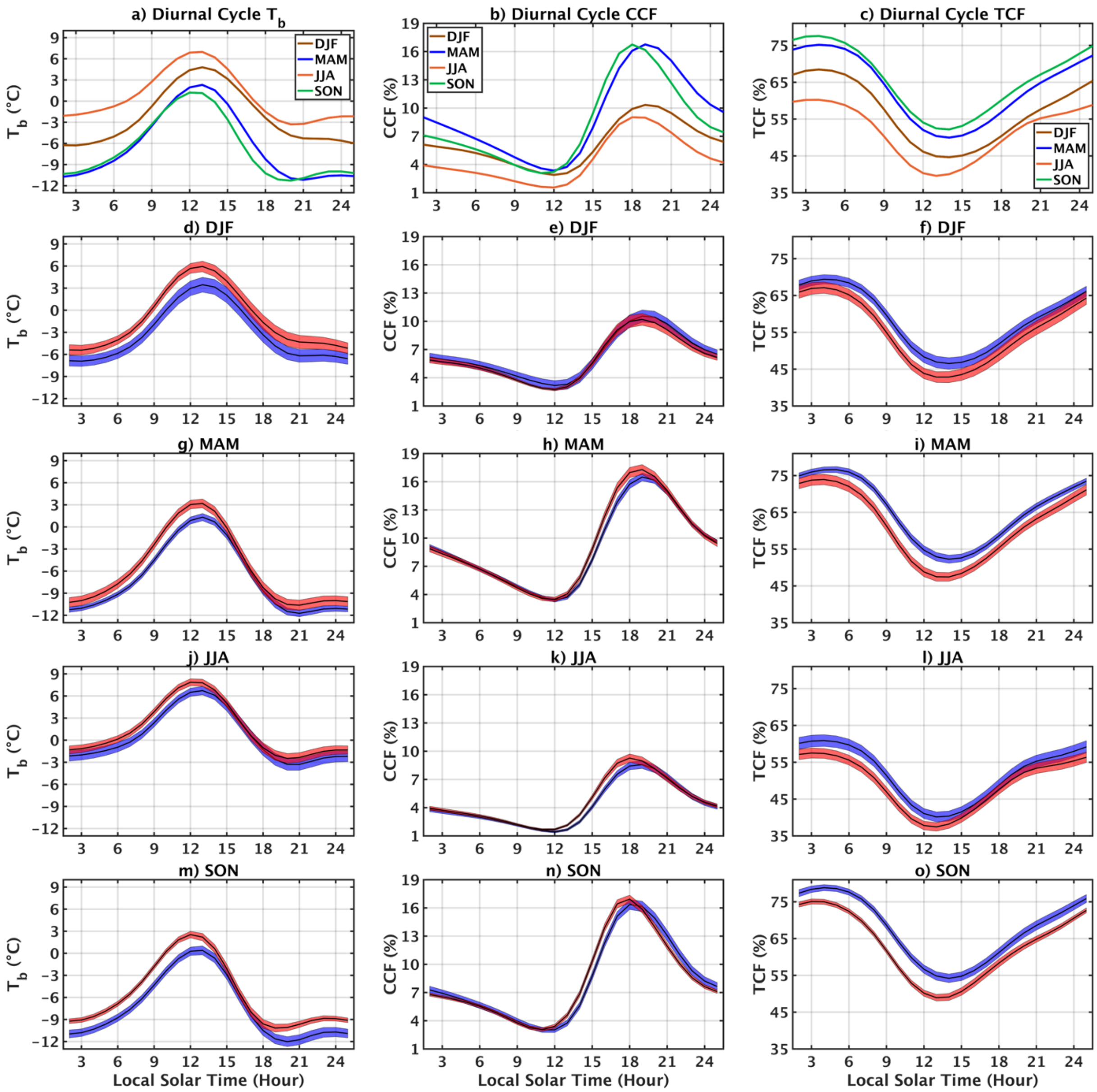

Figure 3.1: Diurnal cycles of (**a**), (**d**), (**g**), (**j**), (**m**) GridSat-B1 T_b (°C), (**b**), (**e**), (**h**), (**k**), (**n**) GridSat-B1 CCF (%), and (**c**), (**f**), (**i**), (**l**), (**o**) GridSat-B1 TCF (%). Averaged over the study domain. (**a**), (**b**) and (**c**): Seasonal averages over the years 1985–2019. (**d**)-(**o**): Averages over the years 1985–1996 and 2008–2019 (black lines) with the respective 95% confidence intervals shown separately, where the blue color represents the years 1985–1996 and the red color represents the years 2008–2019.

To investigate changes in the diurnal cycles of T_b, CCF and TCF, the diurnal cycles averaged over the years 1985–1996 (first third) and 2008–2019 (last third) are shown in Figs. 3.1d–o, together with the respective 95% confidence intervals. For the T_b (Figs. 3.1d, g, j and m), values have increased during the last third when compared to the first third during all seasons, especially in the morning and early afternoon hours until around 14:00 LST. More specifically, the 95% confidence intervals indicate significant differences ($p < 0.05$) between the first and last third from 02:00–15:00 LST and 20:00–21:00 LST during DJF, 02:00–14:00 LST and 22:00–23:00 LST during MAM, 07:00–13:00 LST during JJA, and 01:00–14:00 LST and 19:00–24:00 LST during SON. Consequently, the T_b has increased significantly during all seasons in the mornings, possibly due to a decrease of clouds in the morning and early afternoon, as well as in the late evening. Further, the amount of CCF has increased, mainly in the afternoon hours (Figs. 3.1e, h, k and n). While the 95% confidence intervals of the first and last third are not different during DJF, they are different from 14:00–18:00 LST during MAM, 12:00–17:00 LST during JJA, and 13:00–17:00 LST during SON, indicating a shift to a higher percentage of CCF in the afternoon during all seasons besides DJF, suggesting that thunderstorm activity in the afternoon has been increasing. This is consistent with previous studies showing an intensification of MCSs during the month of February (Taylor et al. 2018), and a general increase in mean convective activity across Africa (Hart et al. 2019). Changes in TCF (Figs. 3.1f, i, l and o) confirm that the amount of clouds has been decreasing in the morning hours, where the 95% confidence intervals of the first and last third are different from 06:00–15:00 LST during DJF, 03:00–24:00 and 01:00 LST during MAM, 02:00–13:00 LST during JJA, and 01:00–24:00 LST during SON, with lower TCF during the later period. Overall, the increased T_b and decreased TCF in the morning, and the increased CCF during the afternoon suggest a decreasing trend in clouds in the morning and a tendency towards stronger and more intense convection in the afternoon in recent years.

To corroborate the above changes of the diurnal cycles of clouds and deep convection obtained from satellite data, the same analysis was conducted using ERA5 T2m and RH2m from 1979 to 2019. Figs. 3.2a and b show the seasonally averaged diurnal cycles of T2m and RH2m, with a T2m maximum at 14:00 LST during all seasons (29.3 °C for DJF; 29.0 °C for MAM; 28.0 °C for JJA; 27.7 °C for SON), and a minimum at 04:00 LST during SON (21.1 °C), 05:00 LST during MAM (21.9 °C), and at 06:00 LST during DJF (21.2 °C) and JJA (20.9 °C). The RH2m maxima are recorded at 04:00 LST during SON (96.4%), 05:00 LST during MAM (95.7%), and at 06:00 LST during DJF (92.2%) and JJA (94.6%), while the RH2m minima are at 14:00 LST during all seasons (57.3% for DJF; 65.4% for MAM; 63.5% for JJA; 68.1% for SON). Furthermore, changes in the diurnal RH2m and T2m cycles (Figs. 3.2c–j) indicate a general warming and drying trend, where the T2m has increased significantly during all hours of the day and all seasons. The RH2m increased during all hours and seasons as well, besides at 07:00 LST during DJF where the changes are not significant.

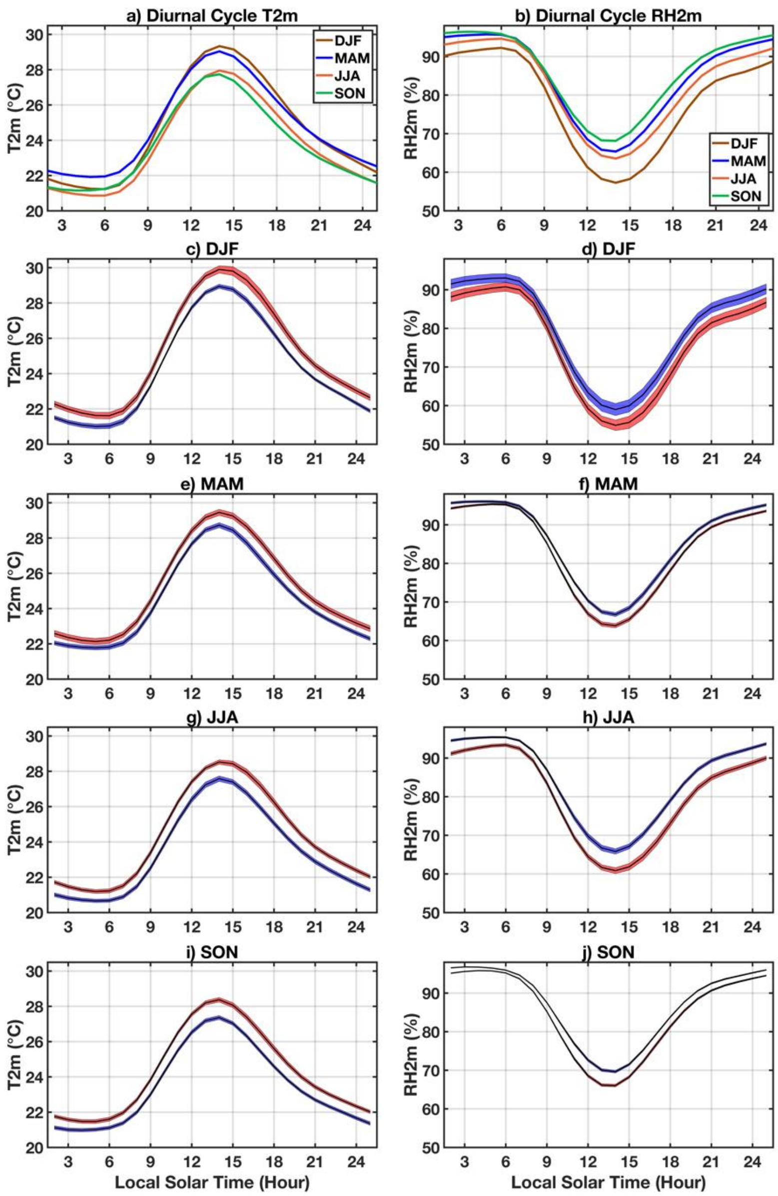

Figure 3.2: Diurnal cycles of (**a**), (**c**), (**e**), (**g**), (**i**) ERA5 T2m (°C), and (**b**), (**d**), (**f**), (**h**), (**j**) ERA5 RH2m (%). Averaged over the study domain. (a) and (b): Seasonal averages over the years 1979–2019. (**c**)-(**j**): Averages over the years 1985–1996 and 2008–2019 (black lines) with the respective 95% confidence intervals shown separately, where the blue color represents the years 1985–1996 and the red color represents the years 2008–2019.

The increase in T_b in the morning hours and in CCF during the afternoon are also illustrated in Figs. 3.3a and b, while Figs. 3.3c and d show the general increase of the T2m and the decrease of the RH2m. More specifically, the T_b increased significantly ($p < 0.05$) in the morning during all months besides February, May and June, while trends in the afternoon are insignificant (Fig. 3.3a). Additionally, trends in CCF (Fig. 3.3b) show significant increases in the afternoon during all months except January, February and December. This is generally consistent with the results from Fig. 3.2, confirming that T_b has increased in the morning while convection intensified in the afternoon.

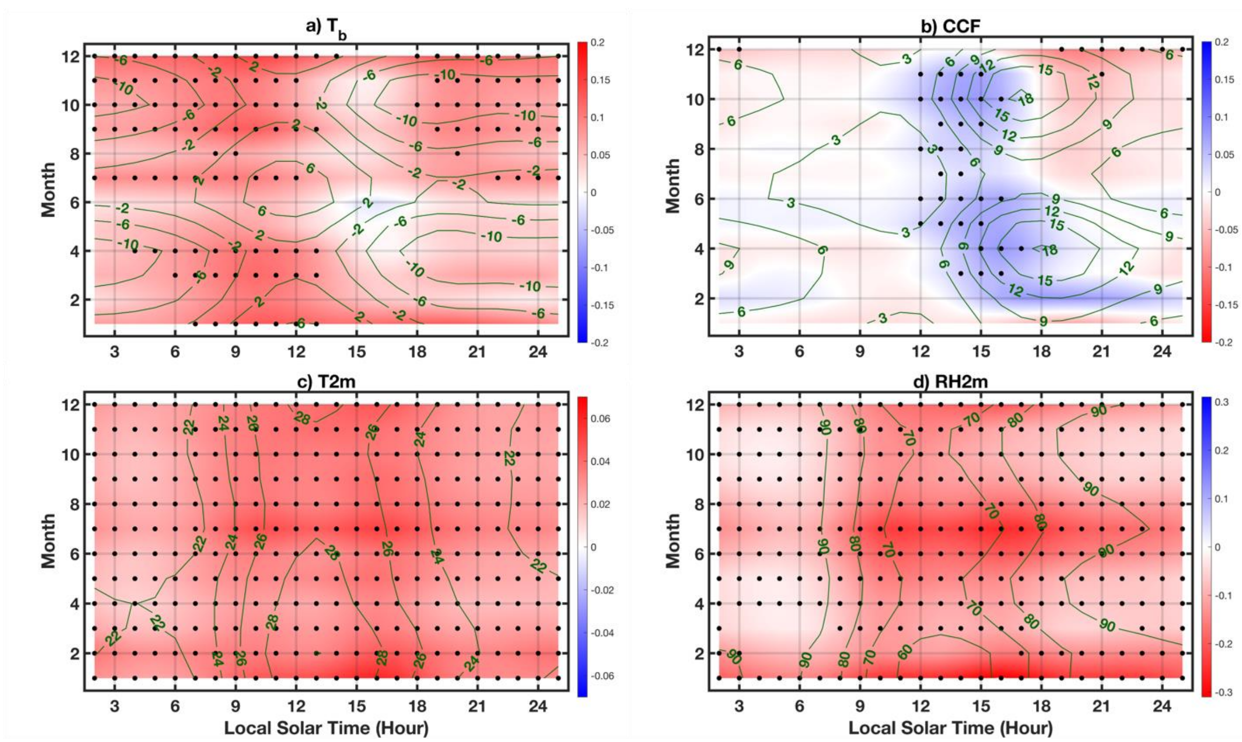

Figure 3.3: Trends in (**a**) GridSat-B1 T_b (°C year^{-1}) from 1985–2019, (**b**) CCF (% year^{-1}) from 1985–2019, (**c**) ERA5 T2m (°C year^{-1}) from 1979–2019, and (**d**) ERA5 RH2m (% year^{-1}) from 1979–2019. Averaged over the study domain. Trends significant at $p < 0.05$ are shown using a black dot. The green lines show the climatological values of T_b (°C) and CCF (%) from 1985–2019, and ERA5 T2m (°C) and RH2m (%) from 1979–2019.

To investigate changes in thunderstorm potential, the diurnal cycles of the GDI averaged over the first (1985–1996) and last (2008–2019) third are shown in Fig. 3.4, together with the according 95% confidence intervals. While there are no significant changes during DJF, the GDI increased significantly ($p < 0.05$) in the afternoon from 13:00–17:00 LST during MAM, from 15:00–18:00 LST during JJA, and from 11:00–17:00 LST during SON. As the GDI is used as a forecasting tool, this confirms that thunderstorm potential has increased in the afternoon and evening hours, complementing the findings in Fig. 3.1, Fig. 3.3.

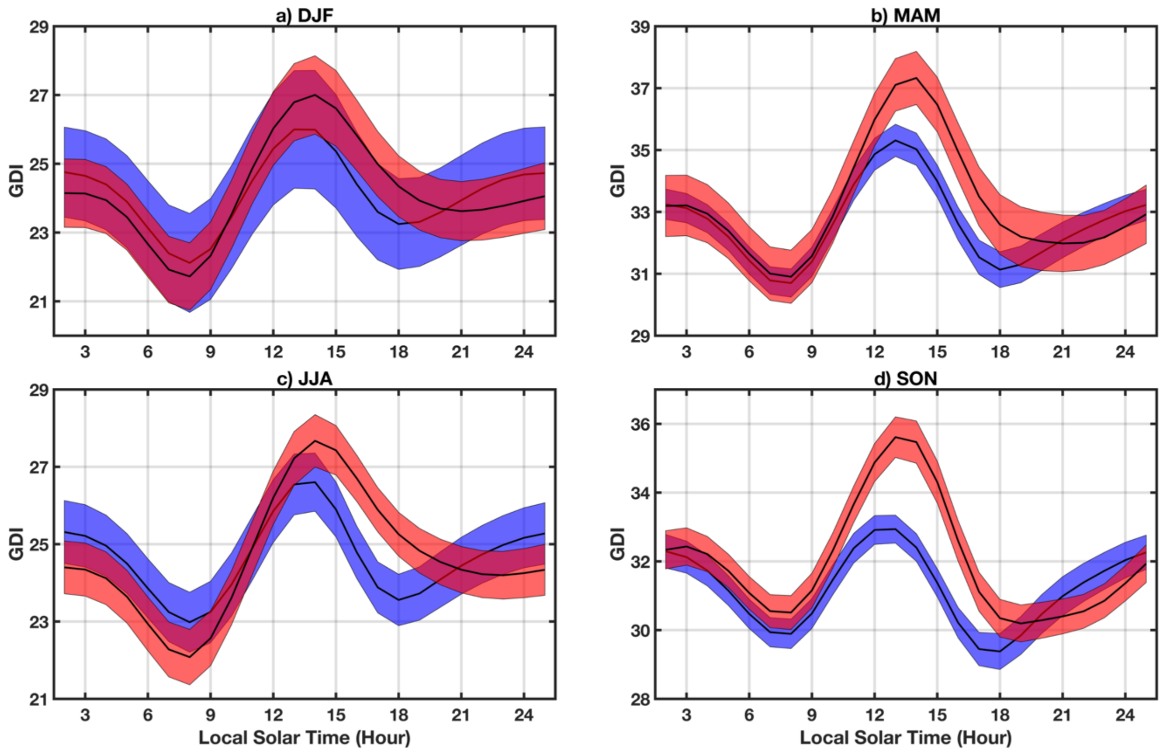

Figure 3.4: Diurnal cycles of the GDI averaged over the study domain. Averages over the years 1985–1996 and 2008–2019 (black lines) with the respective 95% confidence intervals shown separately, where the blue color represents the years 1985–1996 and the red color represents the years 2008–2019.

Table 3.1 lists the trends of the CCF for the years 1985–2019 and the hours 13:00–19:00 LST. The CCF has increased significantly ($p < 0.05$) from 14:00–17:00 LST during all seasons except DJF. More specifically, the increase in CCF is largest at 16:00 LST during JJA (4.18×10^{-2}% year^{-1}) and SON (6.65×10^{-2}% year^{-1}), and at 17:00 LST during MAM (6.65×10^{-2}% year^{-1}) while DJF does not show any significant trends. Consequently, thunderstorms have intensified the most during the afternoon buildup period, and not during the time of maximum deep convection around sunset. The increased thunderstorm intensity during the buildup period may possibly be a result of the surface warming and drying trend associated with the long-term Congo drought and the subsequent decrease in cloud cover in the morning, leading to increased heating and an earlier onset of convection since the convective temperature is reached earlier. The increase in T2m might eventually lead to a shift in the maximum of CCF to an earlier time of day. Fig. 3.5 confirms this hypothesis, where the blue boxplots represent the percentage of CCF averaged over the years 1985–1996 (first third) at 13:00–19:00 LST, and the red boxplots show the same for the years 2008–2019 (last third). The results in Fig. 3.5 are consistent with the trends listed in Table 3.1. The notches of the boxplots of the first and last third for DJF overlap for all times, indicating that they are not significantly different. During MAM, the CCF increased significantly ($p < 0.05$) from 14:00–18:00 LST. For JJA and SON, the differences between the first and last third are significant ($p < 0.05$) from 13:00–17:00 LST, indicating increased CCF in the afternoon hours during all seasons besides DJF. Additionally, the maximum percentage of CCF generally shifted to earlier in the day during all seasons.

Table 3.1. Trends in CCF ($10^{-2} \times \% \text{ yr}^{-1}$) for the different seasons and hours in the afternoon from 1985 to 2019. Values significant at the 95% level are indicated by an asterisk (*).

	DJF	MAM	JJA	SON
13 LST	−1.29	1.52	1.66*	3.35*
14 LST	−0.62	3.11*	2.69*	5.12*
15 LST	0.01	4.90*	3.67*	6.39*
16 LST	0.37	6.31*	4.18*	6.65*
17 LST	0.14	6.65*	3.75*	5.41*
18 LST	−0.80	5.51*	2.15	2.47
19 LST	−2.01	3.54	0.37	−1.04

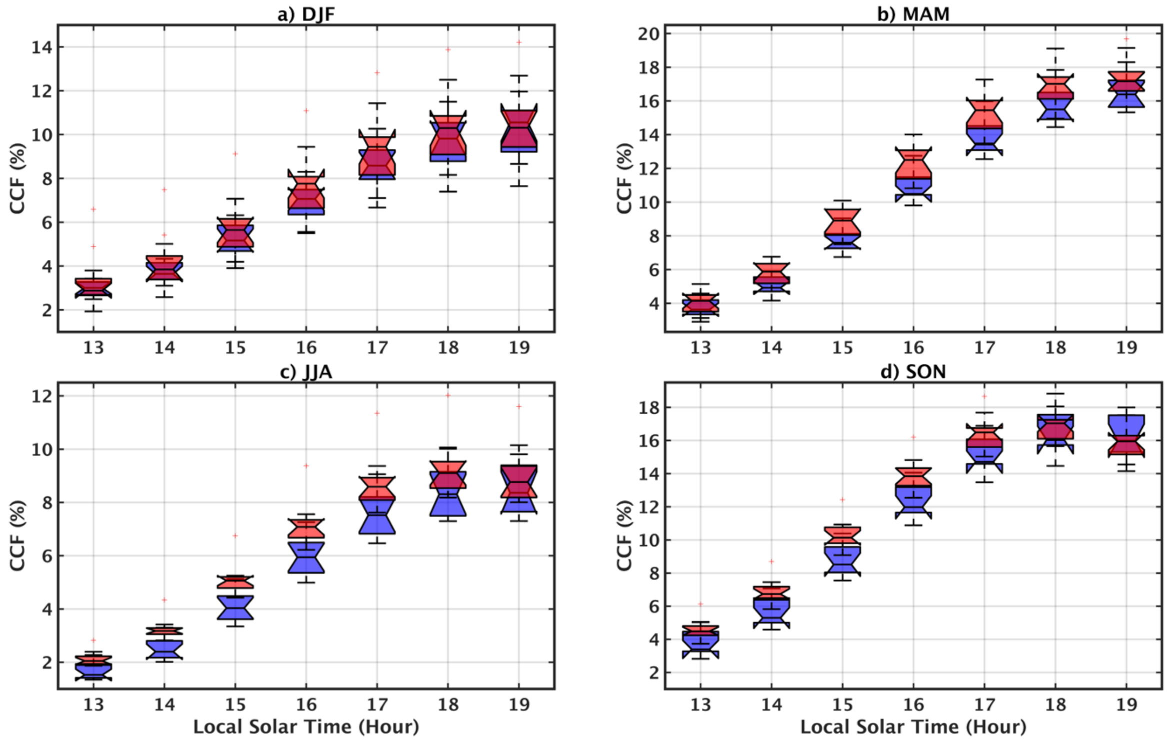

Figure 3.5: CCF (%) at the different times of day (LST) averaged over the first third (1985–1996; blue color) and the last third of the time period analyzed (2008–2019; red color) for the different seasons. Averaged over the study domain. The central black bar on each box represents the median, the edges of the box indicate the 25th and the 75th percentiles, and the notches represent the 95% confidence intervals of the median. The upper and lower whiskers show the variability outside the upper and lower quartiles while outliners are plotted as red crosses.

The interannual variability and linear trends of the diurnal T_b amplitude are displayed in Fig. 3.6. The diurnal T_b amplitude has increased significantly ($p < 0.05$) during all seasons besides JJA, with the largest increase during MAM (0.06 °C year^{-1}), followed by DJF (0.03 °C year^{-1}) and SON (0.03 °C year^{-1}). Consistent with the trends of the diurnal T_b amplitude, the diurnal T2m amplitude has increased by 0.01 °C year^{-1} ($p < 0.05$) during DJF and MAM, and 0.02 °C year^{-1} ($p < 0.05$) during JJA and SON (Fig. 3.7, solid lines). The trends of the ERA5 T2m diurnal amplitude are further compared to the MODIS land surface temperature (Fig. 3.7, dashed lines). The diurnal land surface temperature amplitude shows a significant increasing trend during DJF (0.04 °C; $p < 0.05$) and SON (0.05 °C; $p < 0.10$). The increase found during all seasons in the

T2m diurnal amplitude, during DJF, MAM and SON in the T_b diurnal amplitude, and during DJF and SON in the land surface temperature diurnal amplitude complement the findings from Fig. 3.4, Fig. 3.5, indicating an increase in the diurnal amplitude due to a decrease of clouds in the morning and more vigorous convection in the afternoon, which may be caused by the increased heating and drying observed over the region.

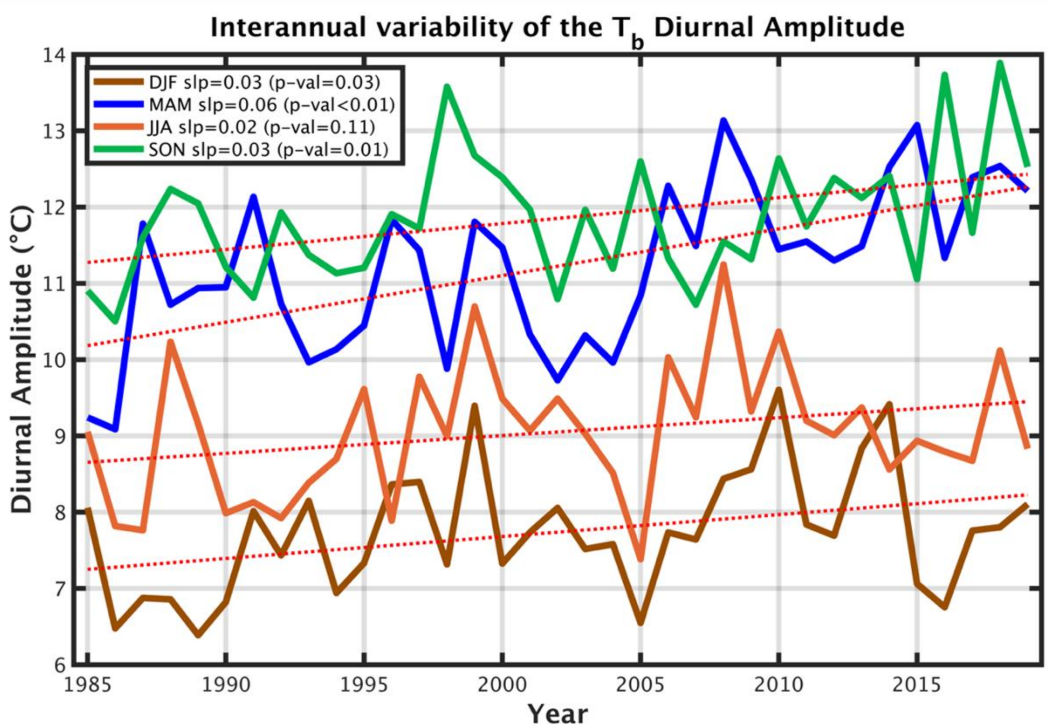

Figure 3.6: Interannual variability and linear trends (°C year^{-1}) of the diurnal amplitude of GridSat-B1 T_b (12:00–13:00 LST vs. 18:00–19:00 LST) from 1985–2019, averaged over the study domain.

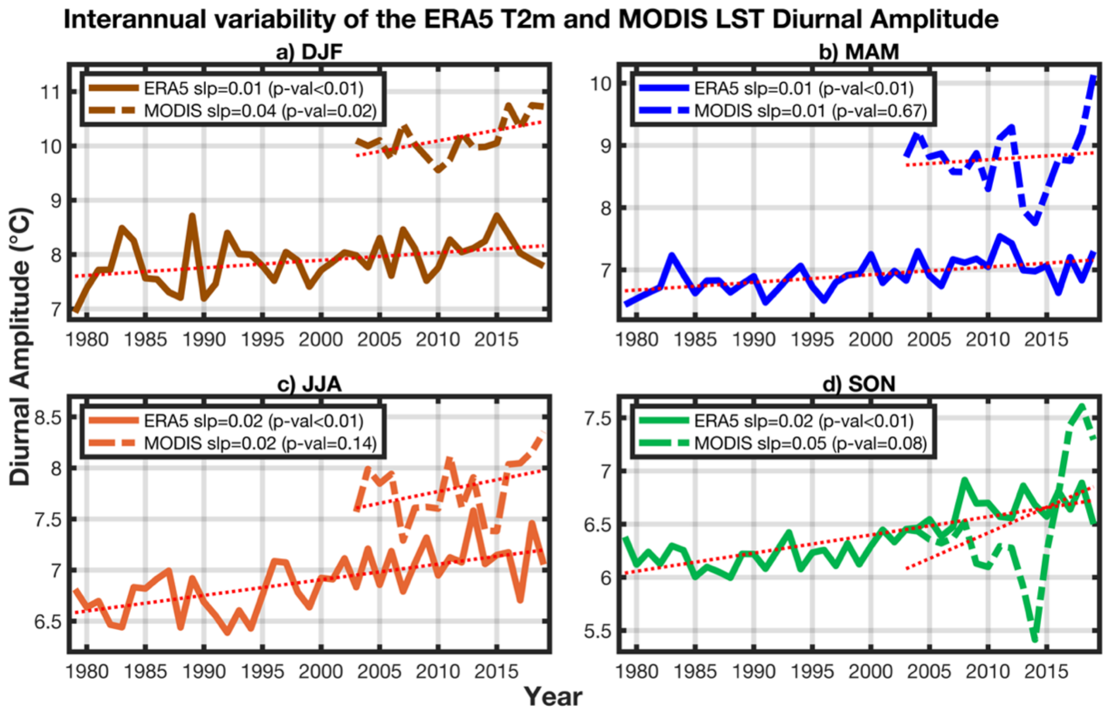

Figure 3.7: Solid lines: Interannual variability and linear trends (°C year^{-1}) of the diurnal amplitude of ERA5 T2m (04:00–06:00 LST vs. 13:00–15:00 LST) from 1979–2019. Dashed lines: Interannual variability and linear trends (°C year^{-1}) of the diurnal amplitude of MODIS land surface temperature (05:30 LST vs. 13:30–15:30 LST) from 2003–2019. Averaged over the study domain.

Fig. 3.8a illustrates the diurnal variations in cloud base height for the different seasons, with a minimum in the morning hours and a maximum in the evening. More specifically, the minimum is recorded at 08:00 LST during SON (445.9 m), 10:00 LST during MAM (785.8 m) and JJA (869.3 m), and at 11:00 LST during DJF (1387.0 m). The maxima are at 23:00 LST during all seasons (2432.7 m for DJF; 1899.6 m for MAM; 1765.1 m for JJA; 1615.1 m for SON). Figs. 3.8 b–e further show a general increase in cloud base height during all hours of the day during MAM, JJA and SON, and from 01:00–10:00 LST and 22:00–24:00 LST during DJF. The increase is most pronounced during the early morning hours and can be explained by the surface warming and drying trend in the study region, as increasing the T2m and decreasing the RH2m will raise the lifted condensation level and ultimately increase the cloud base height.

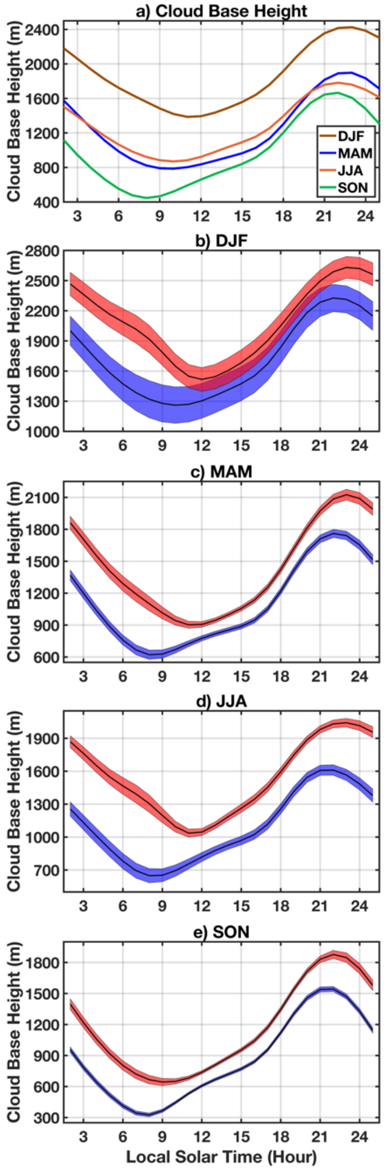

Figure 3.8: Diurnal cycles of the ERA5 cloud base height (m) averaged over the study domain. (**a**): Seasonal averages over the years 1979–2019. (**b**)-(**e**): Averages over the years 1985–1996 and 2008–2019 (black lines) with the respective 95% confidence intervals shown separately, where the blue color represents the years 1985–1996 and the red color represents the years 2008–2019.

Consistent with the observed drought over the Congo, the trends of both the ERA5 and CPC precipitation are decreasing during all seasons (Figs. 3.9a–d). Further, the trends in precipitation efficiency (Fig. 3.9e) have decreased significantly during all seasons, with the strongest decrease of −0.10% year^{-1} ($p < 0.05$) during DJF, MAM and SON, followed by a decrease of −0.08%

year^{-1} ($p < 0.05$) during JJA. The decreasing precipitation efficiency may be a result of the increased cloud base height, leading to an increase in virga and less precipitation reaching the surface (see more discussion in Section 3.5).

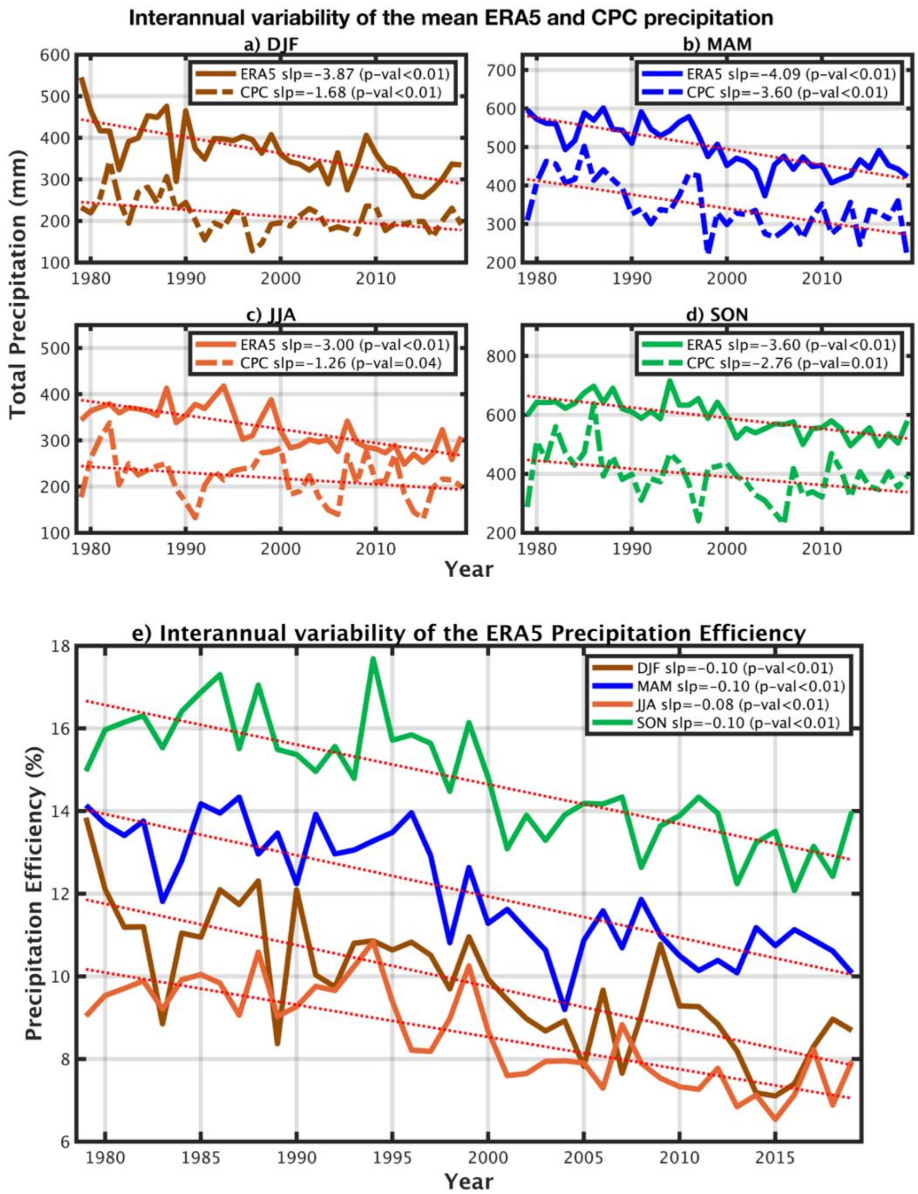

Figure 3.9: (**a**)-(**d**) Interannual variability and linear trends (mm year^{-1}) of the seasonal mean precipitation from hourly ERA5 and daily CPC data from 1979–2019. The ERA5 data is averaged over the study domain, and the CPC data is averaged over the domain 5.25°N to 5.25°S and 12.25°E to 30.25°E. (**e**) Interannual variability and linear trends (% year^{-1}) of the precipitation efficiency, calculated using hourly ERA5 precipitation and ERA5 total column water.

3.5 Discussion and conclusions

In this study, changes in the diurnal cycles of clouds, deep convection and other variables including T2m and RH2m were analyzed over the Congo Basin from 1979 to 2019. The aim of this analysis is to explain and link the changes in the diurnal cycle of deep convection, the decrease in precipitation, and the drying trend observed over the region. The diurnal cycles of T_b, CCF, TCF, T2m, RH2m, cloud base height and GDI were calculated, and their changes were identified and analyzed using a 3–24-hour spectral filter. Furthermore, the long-term trends of the diurnal T_b, land surface temperature, and T2m amplitudes, the CCF, precipitation and precipitation efficiency were investigated.

The results show a maximum in T_b at 12:00–13:00 LST and a minimum in TCF at 13:00–14:00 LST, while a maximum in CCF was found at 18:00–19:00 LST, indicating a minimum in clouds around noon and in the early afternoon, and a peak in deep convection around sunset. Additionally, trends show that the T_b has increased and the TCF has decreased in the morning, suggesting a decrease of cloudiness during the morning hours. In the afternoon, the GDI and CCF have increased where the strongest increase in CCF was detected at around 16:00 LST. This shows increased thunderstorm activity, especially during the afternoon build up period, which is consistent with previous findings showing increased MCS intensity over the Congo (e.g., Raghavendra et al. 2018; Taylor et al. 2018) and enhanced mean convective activity across Africa (Hart et al. 2019). Furthermore, the maximum in CCF shifted to earlier in the day, suggesting that the increased heating and the decrease of clouds in the morning may lead to an earlier onset of convection. Results also show that the diurnal amplitude of convection over the Congo has increased, with the increase in the T_b amplitude reaching from 0.03 °C year^{-1} to 0.06 °C year^{-1}, depending on the season. This may be the combined effect of the decrease in clouds found in the morning and an increase of deep convection in the afternoon.

The enhanced convection found in the study region during recent years may be caused by the observed long-term warming and drying trend over the Congo. Alber et al. (2021a) showed that the increase in thunderstorm activity over the Congo might be the result of an increase in the occurrence of cold troughs at 500 hPa, an increase of the temperature gradient between 700 and 950 hPa, and a decrease of the equivalent potential temperature gradient with height. While the increase in the occurrence of cold troughs is potentially the effect of an increased occurrence of Kelvin waves (Raghavendra et al. 2019), the increase of the temperature gradient and the decrease of the equivalent potential temperature gradient, reducing the vertical stability, may be the result of the observed warming and drying trend of the surface. The enhanced heating and drying during recent years could explain the decrease of clouds in the morning hours and the decrease in the vertical stability of the atmosphere, ultimately enhancing thunderstorm intensity over the region. Consistent with our results, previous studies (e.g., Taylor et al. 2017; Hart et al. 2019) found that MCS frequency is highly correlated with land surface temperatures. Taylor et al. (2017) showed intensified Sahelian MCSs as a result of Saharan warming during the months of June–September. They further demonstrate an asymmetric increase in North African temperatures with increased surface warming in the Northern Hemisphere, which might be correlated to the increase in convective activity found over Africa (Hart et al. 2019). Furthermore, other factors like changes in the mid-latitude circulation may have also contributed to the intensifying convection observed over the Congo (Taylor et al. 2018). For example, upper-level troughs forming over Iberia and Northern Africa during the months of November–March have been found to be related to strong MCS events by Ward et al. (2021). The warming and drying of the surface over the Congo could have further led to the observed increase in cloud base height and the subsequent increase in virga, resulting in more precipitation being vaporized before reaching the surface. This might have caused the recorded decrease in precipitation efficiency (-0.08 to -0.10% year^{-1}), resulting in the observed decrease of precipitation at the surface, reaching from -3.00 mm year^{-1} to

-4.09 mm year^{-1} according to the ERA5 reanalysis dataset, and from -1.26 mm year^{-1} to -3.60 mm year^{-1} according to the CPC dataset. The decrease in precipitation may also be a result of more intense thunderstorms that do not necessarily produce large amounts of precipitation, which has been documented by Hamada et al. (2015) using the Tropical Rainfall Measuring Mission spaceborne radar observations. Therefore, the increased number of thunderstorm cells with increased convective activity observed over the Congo (Raghavendra et al. 2018) possibly also contributes to the decrease in precipitation observed over the region. Additionally, dry air advection from North Africa into the Congo, reduced low-level moisture transport and enhanced subsidence over the Congo Basin may further reduce relative humidity and decrease precipitation over the region (Jackson et al. 2009; Hua et al. 2016).

Based on our results, we propose some potential feedback mechanisms (Fig. 3.10) that may help to explain the contrasting trends in deep convection and precipitation over the Congo. The observed drought, enhancing surface warming and drying, may have caused the detected decrease in clouds during the morning, which increases the T_b. These changes may further result in an earlier onset of convection as the convective temperature is reached earlier, and could explain the stronger, more intense convection in the afternoon, ultimately increasing the diurnal amplitude. Additionally, the drying trend possibly caused the increase of the cloud base height and the subsequent increase in virga, decreasing the precipitation efficiency and accelerating the warming and drying at the surface as less precipitation reaches the ground.

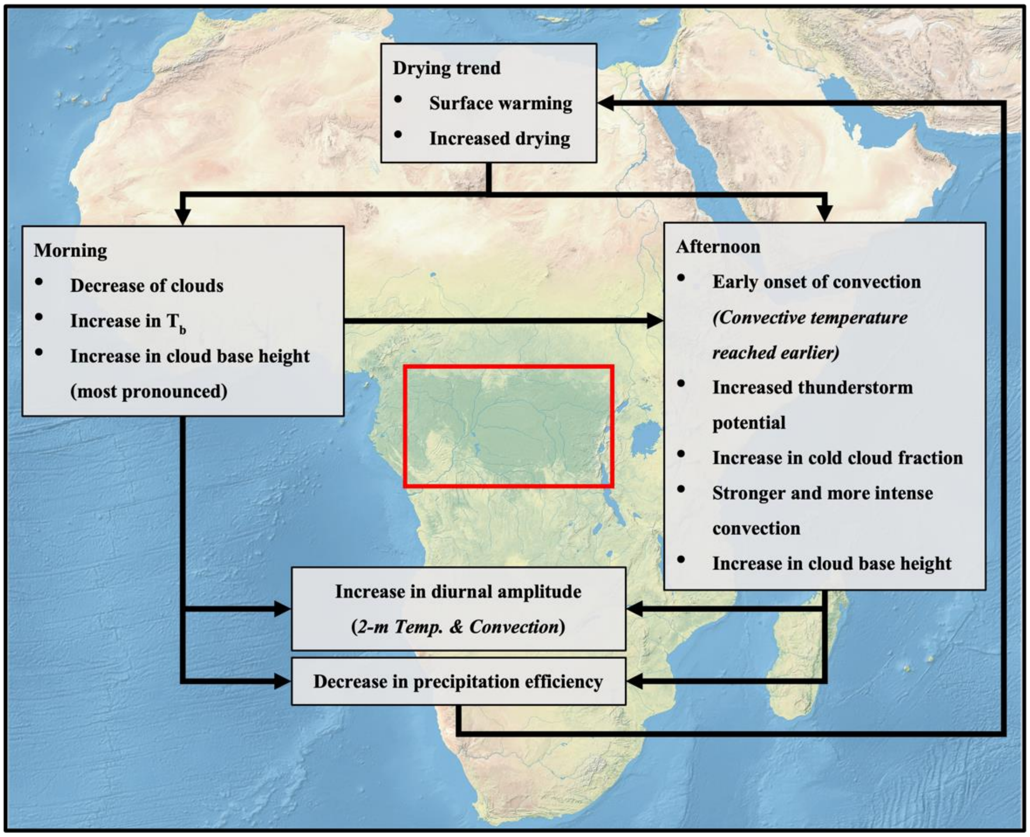

Figure 3.10: Proposed potential feedback mechanisms leading to the observed increase in thunderstorm activity, the decrease in precipitation observed at the surface, and the increase in the diurnal amplitude of T2m and convection over the Congo Basin, including a decrease in clouds in the morning and an increase in convection in the afternoon. The study domain is indicated by the red box (Image credits: Background picture made with Natural Earth).

In summary, our results showed that the diurnal amplitude of convection over the Congo has increased due to the combined effect of an increase of T_b and a decrease in TCF in the morning, and an increase of deep convection in the afternoon. In the morning, T_b has increased while the cloud cover has decreased, possibly due to the observed warming and drying trend in the study region. The surface warming may also enhance the vertical temperature gradient and decrease the equivalent potential temperature gradient with height, resulting in a decrease in convective inhibition, as suggested by Alber et al. (2021a). The decrease in convective inhibition may have caused the increase in thunderstorm activity in the afternoon. While convection has become stronger, precipitation has been shown to decrease. The decrease in precipitation may be a result of more intense thunderstorm cells producing lower amounts of rainfall, as well as the increased surface warming and drying observed over the region, leading to an increase of the cloud base height and a decrease in precipitation at the surface.

CRediT authorship contribution statement:

Kathrin Alber: Conceptualization, Methodology, Software, Validation, Formal analysis, Investigation, Data Curation, Writing – Original Draft, Visualization. **Liming Zhou:** Supervision, Conceptualization, Writing – Review & Editing, Funding acquisition. **Ajay Raghavendra:** Conceptualization, Methodology, Data Curation, Writing – Review & Editing.

CHAPTER 4:

Influence of the Madden-Julian Oscillation on the diurnal cycles of convection and precipitation over the Congo Basin

This work addresses question 3) in section 1.3 and analyzes the impacts of the MJO on the diurnal cycles of convection and precipitation over the Congo and explores possible mechanisms leading to the observed changes by using GridSat-B1, TRMM, and ERA5 data. The hypothesis includes that the MJO modulates precipitation and convection over the region, increasing clouds and rainfall, and delaying peak convection during the enhanced phase. During the suppressed phase the opposite will happen, with a decrease in convection and precipitation and a shift of peak convection to earlier in the day. Circulation changes induced by the MJO are hypothesized to be associated with the observed changes.

This article was published in Atmos. Res., 294, Alber, K., Zhou, L., Roundy, P.E., and Solimine, S.L., Influence of the Madden-Julian Oscillation on the diurnal cycles of convection and precipitation over the Congo Basin, 0169-8095, Copyright Elsevier (2023).

4.1 Introduction

The Congo Basin situated in equatorial tropical Africa is one of the most convective regions in the world and has the second largest latent heating rate from convection after the Maritime continent (MC) (Washington et al. 2013; Feng et al. 2021). Convection and rainfall over the Congo are predominately associated with surface solar heating, resulting in a strong diurnal cycle of clouds and precipitation with a minimum in clouds in the morning and a peak in clouds and convection in the late afternoon and early evening hours (Jackson et al. 2009; Alber et al., 2021b; Hartman 2021). Several previous studies have shown that convection varies diurnally, and that the diurnal variations also differ spatially. Different techniques and datasets have been utilized to investigate the diurnal cycles of tropical convection and precipitation. For example, Hendon and Woodberry (1993) used brightness temperature (T_b) derived from 11 μm satellite radiance measurements lower than 230 K as a threshold to isolate deep convection. Nesbitt and Zipser (2003) used Tropical Rainfall Measuring Mission (TRMM) satellite precipitation measurements to highlight variations in rainfall over tropical land areas, while Yang and Slingo (2001) used global 0.5° and 3-hourly satellite infrared data to provide a climatology of the diurnal cycle of convection and surface temperature in the tropics.

According to Lazri et al. (2014), the life cycle of a convective system can generally be divided into three stages, i.e., growth, maturity, and dissipation. The cycle begins with the vertical growth of a convective core with intensifying vertical updrafts. During this stage, the cloud top height increases, the cloud expands horizontally, and the cloud optical thickness increases while precipitation droplets grow. During the maturity stage, both updrafts and downdrafts exist simultaneously, where evaporating precipitation cools surrounding areas which favors downdrafts while the anvil expands. During the dissipation stage, updrafts weaken and begin to disappear while the anvil reaches a maximum and begins to dissipate and the cloud droplet radius decreases. In the young portions of the cloud, defined by vigorous vertical motion, precipitation is mostly convective where precipitation particles increase the size and mass by collection of cloud water through coalescence and/or riming and the particles fall in heavy showers. In the older regions of the cloud when the vertical motions weaken, precipitation is more stratiform and drifts to the ground more slowly as the particles increase their mass by vapor diffusion (Houze Jr. 1997).

Precipitation and convection over the tropics can be influenced by various modes of variability such as the Madden-Julian Oscillation (MJO), El Niño Southern Oscillation (ENSO) and Indian Ocean Dipole (IOD) (Otto et al. 2013; Hart et al. 2019; Raghavendra et al. 2020; Jiang et al. 2021). The MJO (Madden and Julian 1971, Madden and Julian 1972) is one of the most fundamental modes of atmospheric variability and is the leading mode of intraseasonal variability in the tropics (Dias et al. 2017). It is characterized as an eastward moving planetary-scale signal, associated with strong convection that originates in the Indian Ocean and moves along the equatorial Indian and western-central Pacific Oceans, recurring every 30–90 days (Zhang 2005; Kim et al. 2008). Convection is increased during the MJO enhanced phase and decreased during the MJO suppressed phase. It has also been shown that the MJO interacts with the diurnal cycle (Slingo et al. 2003; Sakaeda et al. 2017). However, the modulation of precipitation by the MJO varies in different regions of the world, and studies disagree on how the MJO affects the diurnal cycle phase and amplitude of rainfall and convection depending on the region. While the diurnal amplitude is found to be decreased during the MJO enhanced phase over the islands of the MC, it is shown to increase over the oceans of the MC during the same phase (Sui et al. 1992; Sui et al. 1997; Rauniyar and Walsh 2011; Oh et al. 2012), suggesting that the MJO impacts the diurnal cycles of rainfall and convection differently over land and the ocean. Furthermore, studies analyzing the influence of the MJO on the diurnal phase show contradictive results. For example, Oh et al. (2012) and Rauniyar and Walsh (2011) identified the MJO's influence on the diurnal phase, while Tian et al. (2006) and Suzuki (2009) found no relationship between the two at all.

Over the Congo, Raghavendra et al. (2020) found a significant relationship between the MJO and rainfall during October through March from 1979 to 2018, showing that the MJO significantly impacts rainfall over the region. They utilized the daily MJO real-time multivariable (RMM) phase index data (Wheeler and Hendon 2004), where RMM phase 2 was regarded as the MJO enhanced phase and RMM phases 5 and 6 were regarded as the MJO suppressed phase over the region. The study showed that the number of days in the MJO suppressed phase increased significantly by 0.34 days year^{-1} from 1979 to 2018, while no significant trends for the number of MJO enhanced days were found. The study concluded that the decreasing trend in the number of MJO dry days may contribute to the observed decrease in rainfall by 13.6% and may thereby help to partially explain the large-scale and long-term drying trend documented during the past three decades over the Congo (Zhou et al. 2014; Hua et al. 2016, Hua et al. 2018; Jiang et al. 2019). Interestingly, in contrast to this drying trend, several studies such as Taylor et al. (2018), Raghavendra et al. (2018), and Alber et al. (2021a) also showed an increase in thunderstorm intensity over the Congo during the past 20 to 30 years.

However, despite being the second largest rainforest on earth, the Congo remains understudied compared to other major rainforests such as the Amazon (Zhou et al. 2014; Alsdorf et al. 2016). Although the impacts of the MJO on African climate have been analyzed, most studies have focused on Eastern Africa (e.g., Pohl and Camberlin 2006; Berhane and Zaitchik 2014; Vashisht and Zaitchik 2022; Maybee et al. 2022; Talib et al. 2023), Southern Africa (e.g., Hart et al. 2013) or Western Africa (e.g., Alaka and Maloney 2012; Sossa et al. 2017). To the best of our knowledge, no studies have been conducted yet to investigate how the MJO may influence the diurnal variations of convection and rainfall over the Congo. This study therefore aims to shed light on the yet unanswered question of how the MJO might impact the diurnal cycles of convection and precipitation over the Congo and investigates the physical mechanisms leading to the observed changes. The results of this analysis will fill the knowledge gap regarding the variability of Congo rainfall and convection and may ultimately help to answer open questions about the long-term drying trend over the Congo. The data used is presented in section 4.2, the methods are described in section 4.3, the results are presented in section 4.4, followed by a summary and conclusion in section 4.5.

4.2 Data

For this study, three different datasets were used, i.e., Gridded Satellite (GridSat-B1) (Knapp 2008; Knapp et al. 2011), TRMM precipitation (Huffman et al. 2007), and ERA5 reanalysis data (Hersbach et al. 2020), where the time period 1985–2019 was investigated. Although the MJO impacts convection and precipitation during all seasons, the months October through March (ONDJFM) were chosen for the analysis because the MJO signal is stronger and the RMM amplitude is generally higher during these months (Zhang and Dong 2004; Raghavendra et al. 2020). Additionally, this period includes both the wet and dry seasons over the Congo since the analysis captures the entire December–February (DJF) dry season, the start of the March–May (MAM) wet season, and most of the September–November (SON) wet season (Nicholson 2018), resulting in the analysis capturing three wet months and three dry months. It is worth noting that the MJO's impacts on convection do not differ significantly between the three dry vs. wet months and we therefore decided to combine these 6 months into one single ONDJFM study period for brevity and clarity. Comparing the modulation of convection by the MJO during all four seasons, i.e., DJF, MAM, JJA, and SON (not shown), also indicated similar results for all seasons besides JJA when the differences between the two MJO phases are more pronounced from noon through the afternoon instead of the nighttime and morning hours. The study domain, i.e., the Congo Basin, is defined as the area from 5°N to 5°S and 12°E to 30°E and is depicted by the black boxes in Fig. 4.1. The diurnal cycle data are indicated in Coordinated Universal Time (UTC).

4.2.1 GridSat-B1 satellite data

The GridSat-B1 infrared channel (11 μm) brightness temperature (T_b) dataset derived from the International Satellite Cloud Climatology Project (ISCCP; Schiffer and Rossow 1983) was used in this study to identify convective clouds. This Climate Data Record quality, long-term T_b dataset was sampled from the European Meteorological (MET) series of geostationary satellites. Since the atmosphere is almost transparent at 11 μm, the satellite measured radiance was utilized to derive T_b for cloud top (i.e., cloudy-sky) or surface (i.e., clear-sky) temperatures. The dataset is available at a 0.07° × 0.07° spatial and 3-hourly temporal resolution from 1981 to present

(Knapp 2008; Knapp et al. 2011). However, only the data from 1985 to 2019 was used here due to the high frequency of missing data between 1982 and 1985 (Raghavendra et al. 2020).

4.2.2 TRMM precipitation data

TRMM satellite precipitation estimates, i.e., TRMM 3B42 and TRMM 2A23, were analyzed to investigate the diurnal cycle of precipitation. The TRMM satellite was launched in November 1997, carrying a precipitation radar (i.e., an active microwave sensor), allowing the sampling throughout the diurnal cycle (Zipser et al. 2006). For the TRMM 3B42, rainfall estimates were acquired from NASA's Goddard Earth Sciences Data and Information Services Center (https://disc.gsfc.nasa.gov/datasets/TRMM_3B42_7/summary), available from 1998 to 2019 at a 3-hourly temporal resolution and a 0.25° × 0.25° spatial resolution. Studies such as Munzimi et al. (2015) and Nicholson et al. (2019) showed that the dataset performs well over the Congo. Additionally, the TRMM precipitation radar rain characteristics (TRMM 2A23) version 7 orbital data were used to provide rain type classification information, i.e., stratiform and convective precipitation. The dataset was acquired from the University of Washington TRMM Database (UWTD) (http://trmm.atmos.washington.edu), available from 1998 to 2013 and interpolated to a 0.05° × 0.05° spatial resolution and to a 1-hourly temporal resolution.

The differentiation between stratiform and convective precipitation in the TRMM 2A23 dataset was made using an algorithm developed by Awaka et al. (1997), where the precipitation type was classified into "stratiform", "convective" and "other" by using two different methods, i.e., the vertical profile method (V-method) and the horizontal pattern method (H-method). The V-method first attempts to detect a bright band (BB) and the precipitation is classified as stratiform if a BB is found. If no BB is detected, the algorithm looks for a strong radar echo which will classify the precipitation as convective. If neither a BB nor a strong radar echo is detected, the precipitation is classified as "other". For the H-method, the radar first aims to detect a convective core and then classifies the precipitation type around the core by examining horizontal patterns of the maximum reflectivity factor. The precipitation classification performed by the two methods is then merged and a final classification is made (Awaka et al. 1997).

It is worth pointing out that the TRMM precipitation data is estimated during the passage of the TRMM satellite over the study region. Thus, the values are relative due to the low sampling frequency of TRMM which is about 0.5 times day^{-1} near the equator, making it imperative to use measurements over several years to be able to sample the diurnal cycle (Jackson et al. 2009).

4.2.3 ERA5 reanalysis

The ERA5 reanalysis dataset (Hersbach et al. 2020) was used to obtain the variables needed to calculate the Gálvez-Davison Index (GDI), i.e., temperature and specific humidity data at 950 hPa, 850 hPa, 700 hPa, and 500 hPa (see section 4.3.3 for a more detailed explanation of the GDI). Additionally, divergence, vertical velocity, U and V wind, relative humidity, and temperature data were acquired in intervals of 50 hPa from 100 hPa to 1000 hPa. For comparison to the TRMM satellite precipitation, ERA5 total precipitation was obtained as well. The data was used at a $0.25° \times 0.25°$ spatial resolution and an hourly temporal resolution from 1985 to 2019 to match the timespan utilized for the GridSat-B1 data. Due to the scarcity of surface observations (e.g., gauge stations and radiosonde networks) over the Congo, it is difficult to identify the most accurate reanalysis dataset over the region. However, it has been shown that the bias and root-mean-square error associated with the ERA-Interim reanalysis dataset is comparable with other reanalysis products over the region (Hua et al. 2019). Additionally, Gleixner et al. (2020) found that the correlation in temperature and precipitation between the ERA5 data and observations improved when compared to the ERA-Interim reanalysis data over Africa.

4.3 Methods

4.3.1 MJO Identification

The daily MJO real-time multivariable (RMM) phase index data (Wheeler and Hendon 2004) from the Bureau of Meteorology in Australia (http://www.bom.gov.au/climate/mjo/) was used to suggest the phases of the MJO. The RMM index, based on a pair of empirical orthogonal functions (EOFs) of the combined fields of outgoing longwave radiation (OLR), 850 hPa and 200 hPa zonal winds averaged from 15°N to 15°S, is widely used to monitor the MJO (Wheeler and Hendon, 2004). Days with an RMM index amplitude >1 were regarded as active MJO days, while days with an RMM index amplitude <1 were considered as inactive MJO days (LaFleur et al. 2015). RMM phases 1 and 2 were defined as the MJO enhanced convective phase, and phases 5 and 6 were considered as the MJO suppressed convective phase over the Congo (Gottschalck et al. 2010; Zaitchik, 2017). A total of 912 days were identified as MJO enhanced days while 1148 days were identified as MJO suppressed days.

4.3.2 GridSat-B1 cloud fraction

To quantify convection, the cold cloud fraction (CCF) was derived from the GridSat-B1 data, by calculating the fraction of grid points with $T_b < -50$ °C within the study domain (e.g., Raghavendra et al. 2018; Alber et al. 2021b). The CCF represents areas in which deep convection occurs since tropical deep convection is characterized by very cold T_b values (Taylor et al. 2017; Hart et al. 2019). Additionally, the cloud fractions with $T_b > -50$ °C and < -25 °C, and $T_b > -25$ °C and < 0 °C were calculated to investigate the diurnal cycles of warmer clouds.

4.3.3 Gálvez-Davison Index

For comparison to the GridSat-B1 CCF, the GDI was derived from the ERA5 reanalysis data to estimate convection. The GDI is calculated by using temperature and specific humidity values at 4 different levels (i.e., 950 hPa, 850 hPa, 700 hPa, and 500 hPa), where ERA5 temperature and specific humidity data was used for the calculation in this study. The GDI is a thermodynamic index, developed by Michael Davison and José Gálvez at NOAA's Weather Prediction Center (WPC) (Gálvez and Davison 2016), aiming to improve forecasts of tropical convection since the skill of traditional stability indices is limited in the tropics. The GDI focusses on thermodynamic processes in the mid- and low troposphere rather than dynamical processes and consists of several different sub-indices evaluating different processes that dominate the variability of convection. It consists of three different sub-indices, the Column Buoyancy Index (CBI) considering the availability of heat and moisture in the middle and lower troposphere, the Mid-Tropospheric Warming Index (MWI) accounting for the stabilizing and destabilizing effects of mid-level ridges and troughs, and the Inversion Index (II) analyzing the entrainment of dry air and stabilization associated with trade wind inversions. The higher the GDI value, the more intense and more likely are thunderstorms and convection. Alber et al. (2021b) showed that trends in the GDI over the Congo are consistent with trends in CCF, and Miller et al. (2019) found that the GDI's skill is considerably higher in forecasting rainfall over Puerto Rico than other stability indices such as CAPE or the K-Index. A complete derivation of the GDI can be found in Gálvez and Davison (2016) and Alber et al. (2021b).

4.3.4 Diurnal cycle calculation

To quantify the impacts of the MJO on the diurnal cycles of convection and precipitation, the diurnal cycles of the GridSat-B1 CCF, the ERA5 derived GDI, and TRMM and ERA5 precipitation for the MJO enhanced and suppressed convective phases were calculated. To highlight the impacts of the MJO on the diurnal cycles, the relative mean differences (RMD) between MJO enhanced and suppressed phases were further calculated by dividing the difference between the two phases by the climatological mean, resulting in a dimensionless quantity. To calculate the diurnal cycles for different variables, the discrete Fourier transform (DFT) was applied to the anomaly data using a fast Fourier transform (FFT) and a 3–24-h spectral filter was applied. Additionally, the 95% confidence intervals of the diurnal cycles were derived by multiplying the standard error with the 95% probability intervals at each timestep. The diurnal cycles of convective and stratiform precipitation derived from the TRMM 2A23 data were calculated by dividing the stratiform and convective precipitation fraction, respectively, by the daily sum of all precipitation, resulting in the stratiform and convective precipitation data being displayed as percentage of the daily total precipitation. As suggested by Negri et al. (2002), a 4-h smoothing was then applied to reduce errors due to the high sampling variability of the TRMM data. Because of the high frequency of missing values in the TRMM 2A23 dataset, the diurnal cycles of stratiform and convective precipitation were calculated using climatological means and were not derived using Fourier analysis. To investigate the physical mechanisms leading to the observed changes in precipitation and deep convection, the time-height cross sections of divergence, vertical velocity, relative humidity, wind speed, and temperature were calculated for the MJO suppressed and enhanced phases, where the according values were averaged over all MJO enhanced days and all MJO suppressed days, respectively. Additionally, the difference between the two MJO phases for each variable was computed separately. To highlight the variations across the day, the diurnal variations of the differences were calculated as follows: For each pressure level, the diurnal average of the difference was calculated first. Then, the diurnal average was subtracted from the difference at each hour and according pressure level.

4.4 Results

4.4.1 Spatial and temporal anomalies associated with the MJO phases

The MJO enhanced and suppressed convective phases are associated with different cloud and rainfall anomaly patterns over the Congo rainforest (Fig.4.1 a–d). During the MJO suppressed phase, a decrease in CCF and a decrease in precipitation of up to 2 mm day^{-1} across some parts of the Congo Basin can be observed over the study region, with the exception of a very small area of slightly increased CCF and precipitation values along the western rift valley and some small areas of increased precipitation areas scattered through the study region (Fig. 4.1a and c). During the enhanced phase, CCF and precipitation are increased over most of the study area, where precipitation increases by up to 1.5 mm day^{-1} in some parts of the study area. Some exceptions include the same area along the western rift valley, showing slightly decreased CCF values (Fig. 4.1b), and smaller patches of decreased precipitation throughout the study domain including along the rift valley (Fig. 4.1d). The anomalies along the western rift valley could be a result of the unique topography in that region, where the altitude increases >1000 m from the Congo Basin up to the East African Highlands. It is also worth noting the strong MJO induced precipitation anomalies outside the study domain along the Gulf of Guinea, which could be an area of future research, where Zaitchik (2017) suggests that the influence of the MJO on West African rainfall might be linked to African Easterly Wave activity during boreal summer.

As for the temporal variations of the number of enhanced and suppressed MJO days, Fig. 4.1e shows that the number of suppressed MJO days has been increasing from 1985 to 2019, while the number of enhanced MJO days has been decreasing slightly but insignificantly. As suggested by Raghavendra et al. (2020), the increase in MJO suppressed days could be a contributing factor to the decrease in precipitation and therefore the drying trend observed over the region. In Fig. 4.1f, the temporal variability of MJO enhanced and suppressed days is shown by month for our study period from 1985 to 2019. The total number of suppressed MJO days per month varies between 161 (March) and 218 (January). For the enhanced phase, the numbers range from 110 days (December) to 203 days (March).

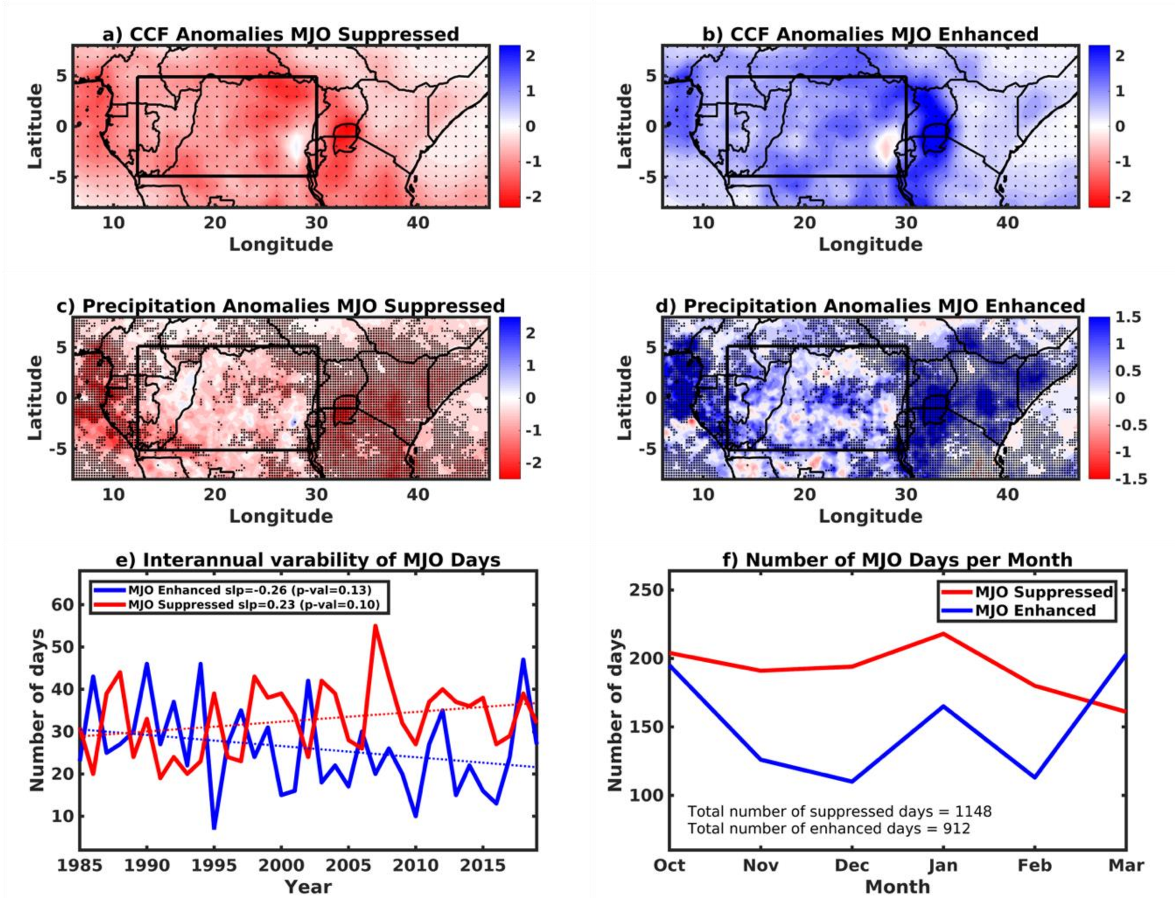

Figure 4.1: (**a–d**): Anomalies of (**a**), (**b**) 3-hourly GridSat-B1 CCF (%) and (**c**), (**d**) daily TRMM precipitation (mm) for the MJO enhanced phase (top) and the MJO suppressed phase (middle) from 1985–2019. The study region (i.e., the Congo Basin) is represented by the black box. The black dots indicate that the values during the enhanced and suppressed phase are significantly different from each other at $p < 0.05$ (determined using a two-sample t-test). (**e**): Interannual variability of the number of enhanced (blue) and suppressed (red) MJO days over the study region during ONDJFM. (**f**): Number of enhanced (blue) and suppressed (red) MJO days per month from 1985–2019 averaged over the study region.

4.4.2 Influence of the MJO on the diurnal cycles of convection and rainfall

The diurnal cycles of CCF and the GDI, indicating deep convection, are shown in Fig. 4.2a and b for the MJO enhanced convective (blue) and suppressed convective (red) phases as well as the climatology (black). Convection peaks in the afternoon, followed by a decrease in clouds during the night and a minimum in the morning, where the CCF and GDI values are generally higher during the MJO enhanced phase and lower during the suppressed phase, as would be expected. According to the purple line representing the RMD between the two MJO phases (right y-axis), the difference is lowest in the afternoon (0.2 for the CCF and 0.093 for the GDI) and increases during the nighttime until it peaks at 09:00 UTC for the CCF (0.65) and at 07:00 UTC for the GDI (0.123). The small difference in timing between the CCF and the GDI could be the result of how the GDI was developed for the operational analysis and forecasting of tropical convection, and the atmosphere is evaluated before convection occurs, where radiative and evaporative cooling induced by clouds will weaken the GDI. Therefore, the GDI is showing the highest values right before peak convection.

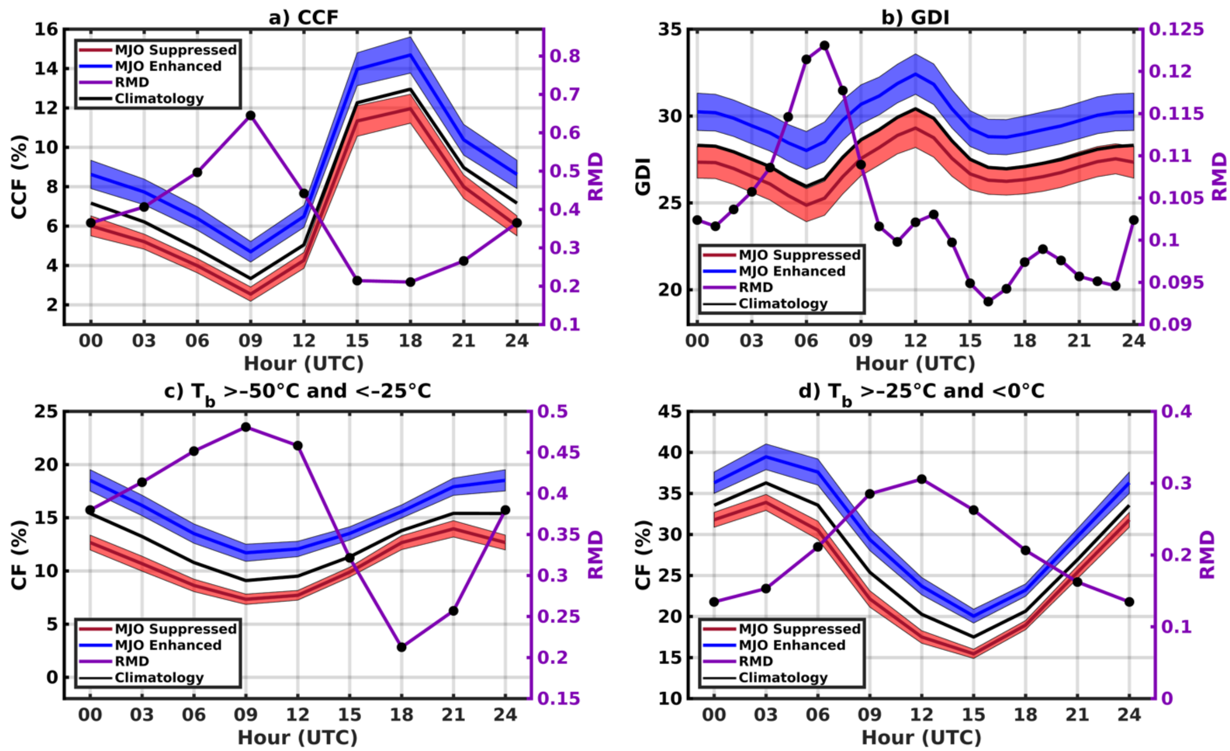

Figure 4.2: Diurnal cycles of (**a**) GridSat-B1 CCF, (**b**) ERA5 GDI, (**c**) GridSat-B1 cloud fractions with T_b between -50°C and -25°C, and (**d**) GridSat-B1 cloud fractions with T_b between -25°C and 0°C averaged over the study region from 1985–2019. The red line shows the distribution for the MJO suppressed phase, the blue line shows the distribution for the MJO enhanced phase, and the black line indicates the climatology, and the purple line represents the RMD between the enhanced and suppressed phase (right y-axis). The 95% confidence intervals are indicated by the blue and red shadings. The black dots indicate that the difference is significant at $p < 0.05$.

In addition to the analysis of MJO induced changes on cold clouds (i.e., CCF), the impacts of the MJO on warmer cloud fractions were investigated next, where Fig. 4.2c and d show the diurnal cycles of cloud fractions with T_b between −50 °C and −25 °C (Fig. 4.2c), and −25 °C and 0 °C (Fig. 4.2d) for both MJO phases. The cloud fraction with T_b between −50 °C and −25 °C peaks at 21:00 UTC during the suppressed phase and at 00:00 UTC during the enhanced phase, indicating a slightly delayed peak during the enhanced phase. A minimum is recorded at 09:00 UTC for both phases. For the cloud fractions with T_b between −25 °C and 0 °C, the maximum is slightly later at 03:00 UTC while the minimum is shown at 15:00 UTC for both phases. The RMDs between the enhanced and suppressed MJO phase are significant ($p < 0.05$) at all times for both cloud fractions, where the difference is highest at 09:00 UTC for the colder cloud fraction and at 12:00 UTC for the warmer fraction. These consistently and significantly higher fractions of clouds with cloud top temperatures higher than −50 °C during the MJO enhanced phase suggest that the MJO not only affects very cold clouds (i.e., CCF in Fig. 4.2a) but also greatly impacts warmer clouds.

In Fig. 4.3a and b, the impacts of the MJO on TRMM and ERA5 precipitation are analyzed, showing a peak in precipitation in the afternoon at 15:00 UTC for the TRMM and at 14:00 UTC for the ERA5 data, where precipitation amounts are generally higher for the ERA5 when compared to the TRMM data. A morning minimum is recorded at 09:00 UTC for TRMM, and at 06:00 UTC for the ERA5 data, which is consistent with the diurnal variations of the CCF and the GDI. As expected, the amount of precipitation is generally higher during the MJO enhanced phase, where the RMD between the two MJO phases is highest through the nighttime and the early morning for both datasets, with the difference peaking at 09:00 UTC for TRMM and at 07:00 UTC for ERA5, similar to the timing of the RMD of CCF and the GDI. Thus, the largest differences in precipitation and convective clouds between both MJO phases seem to occur during the nighttime and morning, when convective processes weaken. During this dissipating stage, the anvil cloud reaches maximal horizontal extent and begins to weaken, while the optical thickness of the cloud decreases, cloud top temperatures begin to increase, and the precipitation changes from convective to more stratiform. Therefore, the impacts of the MJO on stratiform and convective precipitation were investigated separately in a next step, where Fig. 4.3c and d show the diurnal cycles of convective (Fig. 4.3c) and stratiform (Fig. 4.3d) precipitation for the MJO enhanced and suppressed phases. The convective and stratiform precipitation is indicated as fractions of the daily sum of all precipitation, where 59.6% of all precipitation was classified as convective, 36.3% was classified as stratiform, and 4.1% was classified as other. Please note that the TRMM convective and stratiform precipitation data is available from 1998 to 2013 only, while the TRMM total precipitation is available from 1998 to 2019. Although the years 1998 to 2019 were used in this study for the TRMM total precipitation, the diurnal cycle of total precipitation is similar when using the timespan 1998 to 2013 only.

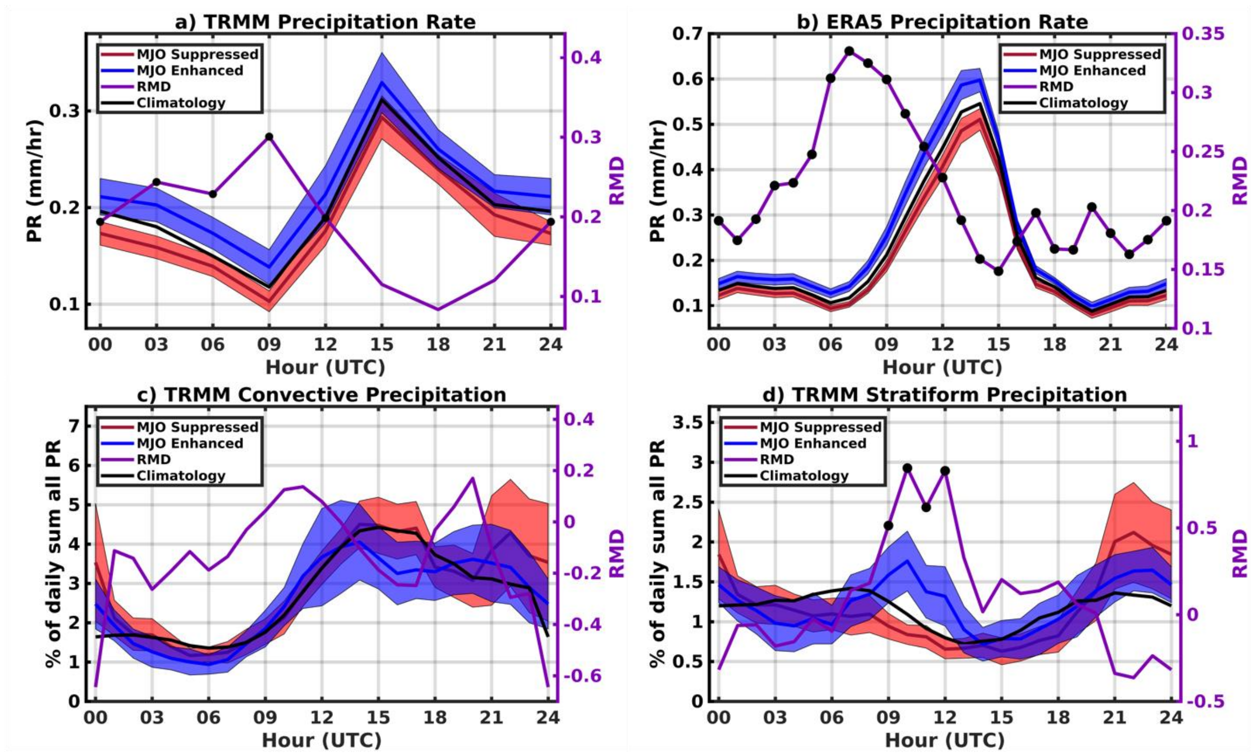

Figure 4.3: Diurnal cycles of (**a**) TRMM precipitation (1998–2019), (**b**) ERA5 precipitation (1985–2019), (**c**) TRMM convective precipitation contributions to the daily sum (1998–2013), and (**d**) TRMM stratiform precipitation contributions to the daily sum (1998–2013), averaged over the study region. The red line represents the distribution for the MJO suppressed phase, the blue line shows the distribution for the MJO enhanced phase, the black line indicates the climatology, and the purple line represents the RMD between the enhanced and suppressed phase (right y-axis). The 95% confidence intervals are indicated by the blue and red shadings. The black dots indicate that the difference is significant at $p < 0.05$. A 4-hour smoothing was applied to the data TRMM convective and stratiform precipitation data due to the high spatial variability of the TRMM 2A23 sampling.

The convective precipitation fractions for the MJO enhanced and suppressed phases are similar, where a minimum is recorded at around 06:00 UTC for both MJO phases. For the enhanced phase, a first maximum occurs around 14:00 UTC (4.0%) with a second smaller peak at 20:00 UTC (3.6%). During the suppressed phase, a first maximum is recorded around 14:00 UTC (4.5%), followed by a second peak at 22:00 UTC (4.3%). The stratiform precipitation fraction exhibits a minimum at 14:00 UTC during the enhanced phase (0.7%) and 15:00 UTC during the suppressed phase (0.6%), followed by an increase in precipitation with a maximum at 22:00 UTC during the suppressed phase (2.1%). For the enhanced MJO phase, a first maximum is recorded at 23:00 UTC (1.6%), followed by a second peak at 10:00 UTC (1.7%). The difference between the two phases is highest at that time, where the difference is significant ($p < 0.05$) between 09:00 and 12:00 UTC. These results suggest that the difference in precipitation between the MJO enhanced and suppressed phase shown in Fig. 4.3a is mainly due to the difference in the stratiform precipitation. Thus, the MJO may impact the stratiform precipitation more than convective precipitation.

4.4.3 Possible physical mechanisms responsible for the MJO induced modulations

To investigate the underlying physical processes leading to the observed differences in the diurnal cycles of precipitation and convection between the MJO enhanced and suppressed phases, two variables relevant to vertical circulation, i.e., horizontal divergence and vertical velocity, were investigated next (Fig. 4.4). Divergence and vertical velocity profiles are useful to gain information about heating profiles since they are tightly coupled and play an important role in large-scale tropical dynamics (Mapes and Lin 2005). The vertical and diurnal structures of divergence shown in Fig. 4.4a and c are similar for both MJO phases. For the upper tropospheric levels (100 hPa to 300 hPa), divergence is prominent during all hours of the day with the strongest values in the evening. From 300 hPa to 400 hPa, a band of convergent air motion is recorded. In the mid-levels from 400 hPa to 700 hPa, divergent air motion is evident from the nighttime through the early afternoon, where divergence is strongest between 08:00 UTC and 12:00 UTC. During the afternoon and evening, the airflow changes from divergent to convergent. In the levels below 700 hPa, the airflow is convergent during all times of day. The contour lines show that the biggest anomalies are recorded in the upper levels during all times of day and during the morning hours in the mid-levels, where divergence is anomalously strong in the mid-levels during the suppressed phase and in the upper levels during the enhanced phase.

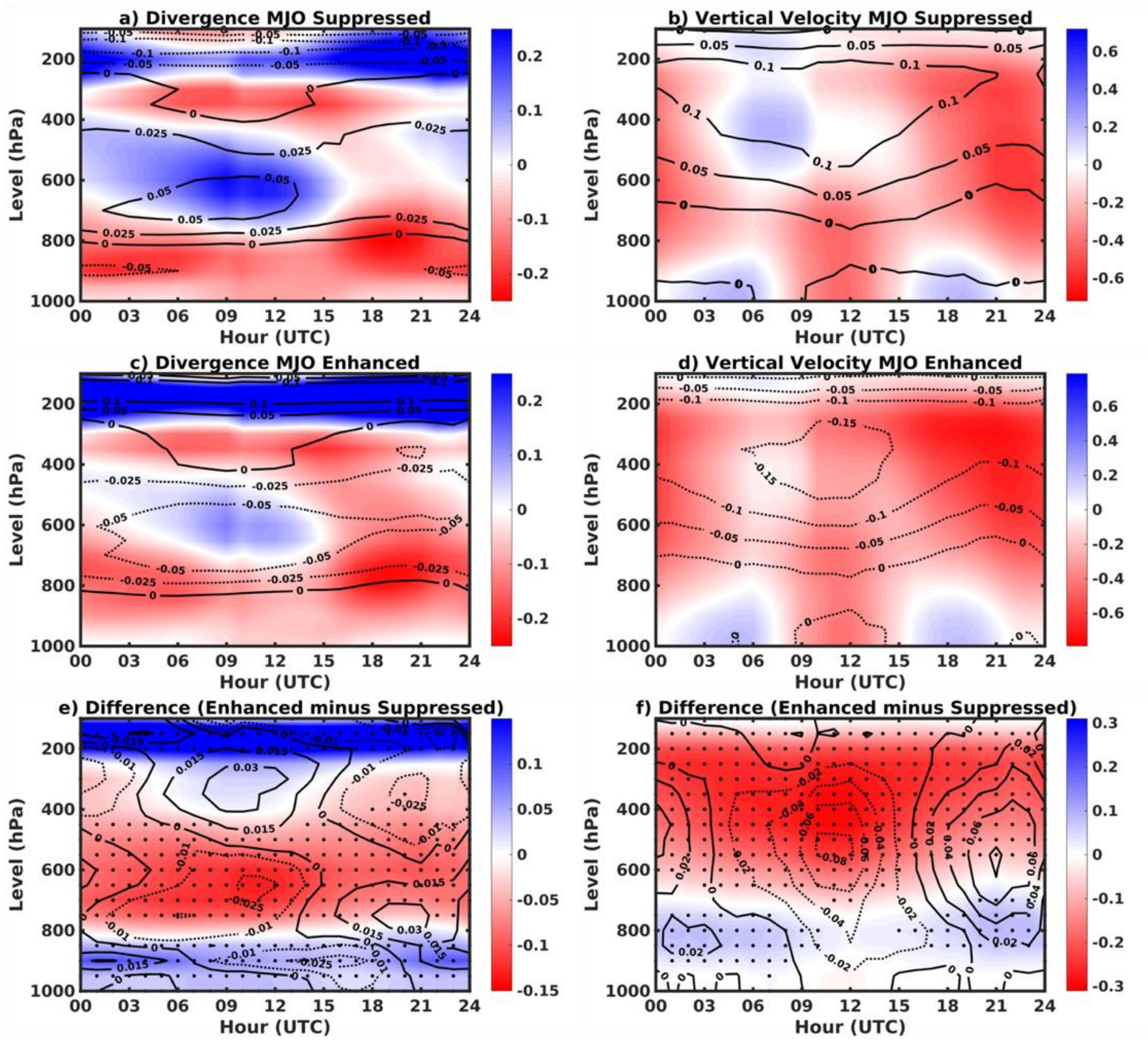

Figure 4.4: (**a–d**): Time-height cross sections of (**a**), (**c**) ERA5 divergence ($10^{-5} \times s^{-1}$) and (**b**), (**d**) ERA5 vertical velocity ($10^{-1} \times$ Pa s^{-1}) for the MJO suppressed phase (top) and the MJO enhanced phase (middle), averaged over the study region from 1985–2019. The shading represents the values averaged over all MJO suppressed days and all MJO enhanced days, respectively. The black contour lines indicate the anomalies (i.e., the difference between the MJO enhanced/suppressed days and all days during ONDJFM). (**e–f**): Difference between the MJO enhanced and suppressed phase for (**e**) ERA5 divergence and (**f**) ERA5 vertical velocity (shading) where the black dots indicate that the difference is significant at $p < 0.05$. The contour lines show the diurnal variations of the difference.

Looking at the time-height cross sections of vertical velocity (Fig. 4.4b and d), the diurnal patterns are similar during both MJO phases as well. The figures indicate evening and nighttime subsidence in the lowest levels (900 hPa to 1000 hPa), uplift in the low and mid-levels (600 hPa to 1000 hPa) from the late morning through the early afternoon, and strong rising motion during the afternoon and evening from the mid through the upper levels (200 hPa to 700 hPa). Additionally, there is subsidence evident during the suppressed phase from 100 hPa to 500 hPa from around 03:00 to 10:00 UTC, while the air motion is neutral or lightly upward during the enhanced phase at the same time and levels, besides a small area of subsidence at 100 hPa. This may lead to shallower convection and faster dissipation of the stratiform precipitation portions of the clouds during the suppressed phase. According to the contour lines, the largest anomalies for both phases are occurring around 400 hPa in the morning and early afternoon hours.

Although the vertical and diurnal divergence and vertical velocity structures are similar during the MJO enhanced and suppressed phase, important differences between the two phases can be observed, mostly related to the strength of the airflow, where Fig. 4.4e and f highlight those differences. Fig. 4.4e shows stronger upper-level divergence during all times of the day and weaker mid-level divergence at night during the MJO enhanced phase. Additionally, mid-level convergence is stronger in the afternoon and evening during the enhanced phase. These results suggest deeper convection and stronger stratiform precipitation portions of deep convection when the MJO is in its enhanced phase. The contour lines in Fig. 4.4e show variation from the diurnal average of the anomalies at each level and hour, highlighting the diurnal variations of the differences between the two MJO phases. For the upper levels, the variations are greatest from 03:00 UTC to 05:00 UTC, indicating that the differences are greatest during the nighttime. For the mid-levels, the differences are enhanced from around 09:00 UTC to 13:00 UTC, and for the lower levels, they are strongest from 00:00 UTC to 03:00 UTC. Overall, the differences in divergence between the two MJO phases are largest in the upper levels, followed by the mid and lower levels.

In the upper and lower levels, the differences are strongest during the nighttime. For the mid-levels, the differences are largest during the mid-morning, which is consistent with the time of peak changes in convection and precipitation shown in Fig. 4.2, Fig.4.3.

For the vertical velocity, the difference cross section (Fig. 4.4f) shows that there is generally more upward air motion during the enhanced phase from 100 hPa to around 700 hPa during all times of day, where the difference is most pronounced from about 09:00 UTC to 13:00 UTC. To a smaller extent, there is more subsidence during the enhanced phase in the lower levels. As shown by the contour lines indicating the variations across the day, the difference between the two MJO phases is largest from 09:00 UTC to 13:00 UTC from 400 hPa to 600 hPa, which is consistent with the time of the largest differences in precipitation and convection shown in Fig. 4.2. In the levels below 700 hPa, the largest differences are recorded from the evening through the early morning.

In summary, upward air motion is stronger during the MJO enhanced phase when compared to the suppressed phase, especially in the mid-levels and around noon. Additionally, upper-level divergence is stronger during the MJO enhanced phase. During the suppressed phase, nighttime and morning mid- and upper-level subsidence and mid-level divergence are pronounced. Regarding the diurnal variations, the largest differences in divergence and vertical velocity between the two MJO phases occur from the late morning through the early afternoon in the mid-levels which is consistent with the time of the largest differences in precipitation and convection, and during the nighttime in the lower (divergence and vertical velocity) and upper (divergence only) levels. Furthermore, the timing of peak TRMM and ERA5 precipitation and GridSat-B1 CCF is consistent with the strong upward vertical velocities as well as enhanced convergence in the low- and mid-levels and strong divergence in the upper levels derived from the ERA5 data, indicating that the two satellite datasets are generally consistent with the ERA5 reanalysis data.

To better explain the different impacts of the MJO on stratiform and convective precipitation, the time-height cross sections for wind speed, relative humidity, and temperature are shown in Fig. 4.5 since previous studies (e.g., Schumacher and Houze Jr. 2003; Schumacher and Houze 2006; Lin et al. 2004) suggest that wind shear and relative humidity play an important role in the formation of stratiform precipitation, and deep convection may also impact the temperature in the troposphere (Johnston et al. 2018). The diurnal wind speed patterns are relatively similar during both MJO phases (Fig. 4.5a and d). However, the diurnal structures are generally weaker during the enhanced phase. The contour lines, indicating the anomalies during the respective MJO phase, show the largest anomalies in the upper levels during both phases. Additionally, Fig. 4.5g shows that wind speeds are generally weaker in the mid-levels and stronger in the upper and lower levels during the enhanced phase. This may contribute to the increased production of stratiform precipitation during the enhanced phase since weaker mid-level winds may increase stratiform rain by decreasing entrainment in stratiform clouds through decreased sublimation and evaporation (Schumacher and Houze 2006). Furthermore, vertical wind shear appears to be stronger during the enhanced phase, which contributes to convective organization (Anber et al. 2014; Robe and Emanuel 2001) and may also increase stratiform precipitation (Saxen and Rutledge 2000). The diurnal variations of the differences between the two MJO phases (contour lines in Fig. 4.5g) are relatively small, where the highest differences are recorded from 18:00 UTC to 21:00 UTC in the upper levels, from 05:00 UTC to 10:00 UTC in the mid-levels, and from 00:00 UTC to 05:00 UTC in the lowest levels. The observed decrease in wind speed in the mid-levels during the enhanced phase, which is most pronounced during the mornings, might be another contributing factor to the increased stratiform precipitation during the morning.

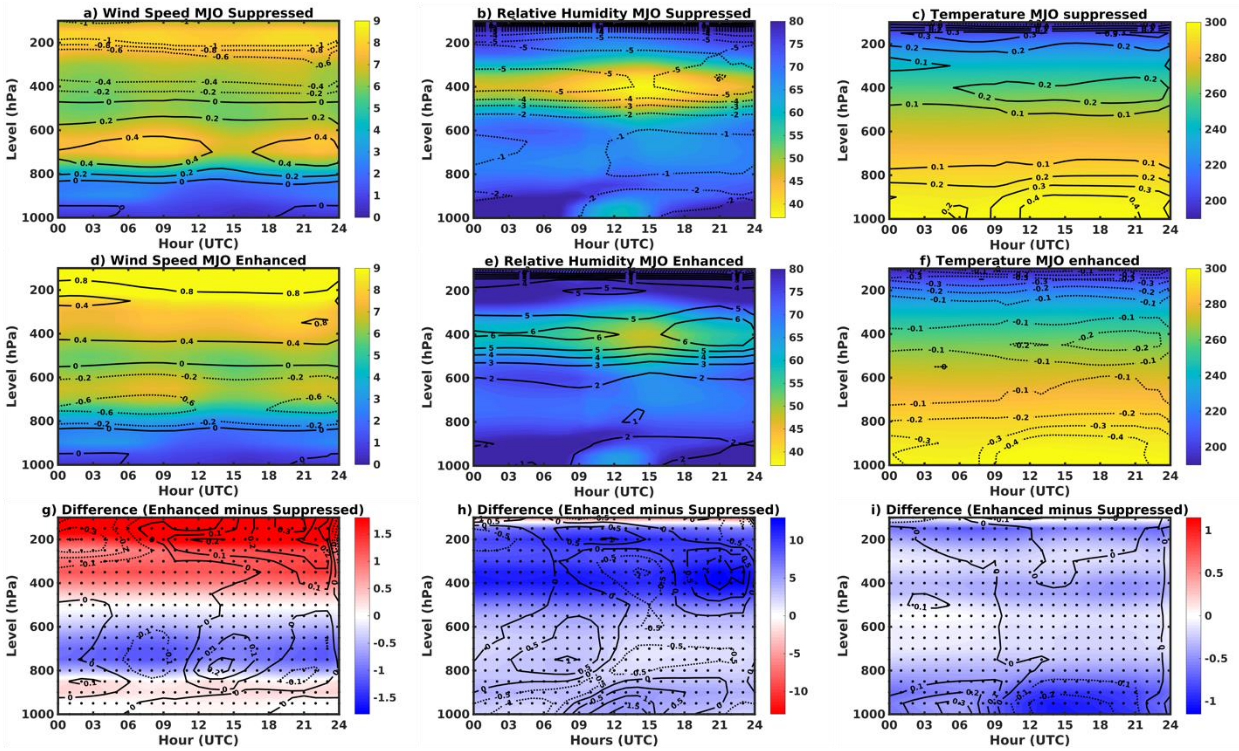

Figure 4.5: (**a–f**) Time-height cross section of (**a**), (**d**) ERA5 wind speed (ms^{-1}), (**b**), (**e**) ERA5 relative humidity (%), and (**c**), (**f**) ERA5 temperature for the MJO suppressed phase (top) and the MJO enhanced phase (middle), averaged over the study region from 1985–2019. The shading represents the values averaged over all MJO suppressed days and all MJO enhanced days, respectively. The black contour lines indicate the anomalies (i.e., the difference between the MJO enhanced/suppressed days and all days during ONDJFM). (**g-i**): Difference between the MJO enhanced and suppressed phase for (**g**) ERA5 wind speed, (**h**) ERA5 relative humidity, and (**i**) ERA5 temperature (shading) where the black dots indicate that the difference is significant at $p < 0.05$. The contour lines show the diurnal variations of the difference.

The relative humidity profiles (Fig. 4.5b, e, and h) show generally higher relative humidity during the enhanced phase. The contour lines in Fig. 4.5b and e, as well as the shading in Fig. 4.5h indicate that the differences between the two MJO phases are greatest around 400 hPa. Similar to the wind speed, the diurnal structures of relative humidity are weakened during the enhanced phase, where the area of lower relative humidity around 400 hPa is less pronounced during the enhanced phase. According to the contour lines in Fig. 4.5h indicating the diurnal variations of the difference, the highest differences are recorded in the evening from 100 hPa to 600 hPa, from

03:00 UTC to 10:00 UTC from 600 hPa to 800 hPa, and from 12:00 UTC to 15:00 UTC from 800 hPa to 1000 hPa. Thus, the higher relative humidity during the MJO enhanced phase, especially in the upper and mid-levels during the nighttime and morning, may help in enhancing precipitation during the MJO enhanced phase. The observed higher relative humidity during the enhanced phase may also be contributing to the observed increase in stratiform precipitation during that phase, since studies such as Schumacher and Houze (2006) propose that a moist atmosphere may assist stratiform growth.

The temperature profiles (Fig. 4.5c and f) show similar structures overall, with generally colder temperatures during the MJO enhanced phase where the greatest differences are recorded in the afternoon and early evening below 800 hPa (Fig. 4.5i). Increased deep convection during the MJO enhanced phase could possibly be leading to enhanced atmospheric cooling and cold convective downdrafts, resulting in a transport of cold air to the lower levels and subsequently lowering the air temperature near the surface. Additionally, evaporative and radiative cooling could also be contributing factors to the lower temperatures during the MJO enhanced phase (Schiro and Neelin 2018; Rooney et al. 2018).

Overall, the higher relative humidity and the lower wind speed in the mid-levels in the morning during the enhanced phase could both be factors contributing to the development of increased stratiform precipitation in the morning with convective cooling possibly leading to the observed lower temperatures during the enhanced phase.

4.5 Summary and discussion

This study analyzes the impacts of the MJO on the diurnal cycles of convection and precipitation from 1985 to 2019, using TRMM and GridSat-B1 satellite as well as ERA5 reanalysis data. Additionally, the physical mechanisms leading to the observed differences in the diurnal cycles between the MJO enhanced and suppressed phases are investigated using ERA5 vertical velocity, divergence, wind speed, relative humidity, and temperature data. Results show that the differences between the MJO enhanced and suppressed phases are largest during the nighttime and morning hours when convection is weakest and are possibly the result of circulation changes due to the MJO. Figure 4.6 summarizes the most important processes observed during the MJO enhanced and suppressed convective phase, respectively, and highlights the differences in clouds, precipitation, horizontal divergence, and vertical velocity between the two MJO phases, where the green arrows indicate the processes that are most important for the respective MJO phase compared to the other phase. During the MJO suppressed phase (Fig. 4.6a), subsidence is evident in the upper and mid-levels during the nighttime and morning hours (Fig. 4.4b), accompanied by strong divergence in the mid-levels (Fig. 4.4a). The observed subsidence and divergence may suppress convection, enhance the decay of convective clouds and the dissipation of the anvil while also inhibiting the vertical growth of new convective cores and vertical updrafts in the mid and upper levels. This will eventually result in more shallow convection and weakened stratiform precipitation portions of deep convection, ultimately leading to a decrease in stratiform precipitation (Fig. 4.3). During the enhanced phase (Fig. 4.6b), divergence in the upper levels is stronger, while nighttime and morning divergence in the mid-levels is much weaker (Fig. 4.4c). The air motion is generally upward with no observed subsidence in the mid- and upper levels (Fig. 4.4d), which may lead to the weaker mid-level divergence. This is possibly causing a slower decay of older convective clouds and dissipation of anvils during the nighttime and morning, and may encourage the growth of new convective cores, resulting in larger anvils and enhanced stratiform precipitation rates (Fig. 4.3). Additionally, mid-level rising air motions and convergence are enhanced in the afternoon and evening (Fig. 4.4d), which is possibly contributing to the increased and deeper afternoon convection as well as the increased precipitation amounts.

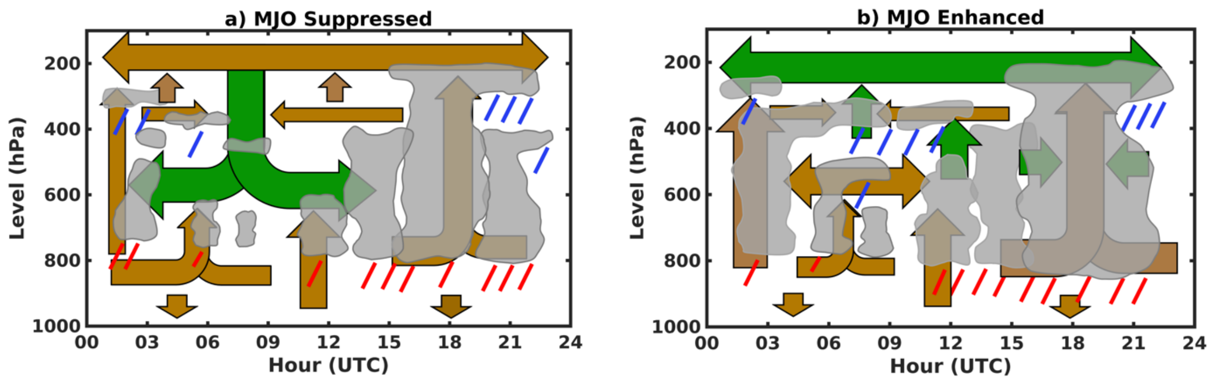

Figure 4.6: Schematic of the diurnal cycle for the (**a**) MJO suppressed and (**b**) MJO enhanced phase, for clouds, rainfall, and air motions (i.e., divergence and vertical motions), where the green colored arrows indicate dominant processes during the respective MJO phase compared to the other MJO phase, and the brown arrows indicate less important processes for the respective phase. Convective precipitation is indicated by the red lines at the bottom of the convective clouds and stratiform precipitation is represented by the blue lines at the anvils.

The above-described observed impacts of the MJO on the diurnal cycles of precipitation and convection over the Congo differ somewhat from the MJO's influence on other tropical regions close to the MJO's center. Oh et al. (2012) analyzed the impacts of the MJO on the diurnal cycle of rainfall over the western MC and found the largest impacts over land to occur during peak convection in the afternoon and not during the morning, showing an increased hourly maximum rain rate during the MJO enhanced phase when compared to the suppressed phase. The observed changes are attributed to anomalous low-level winds during the respective MJO phase, interacting with the monsoonal flow over the MC. Liu et al. (2022) also found the MJO to be interacting with the American and African monsoons through different mechanisms, for example by exciting Kelvin waves and mid-latitude teleconnections. While we found small changes in the diurnal amplitudes of precipitation or convection, Lu et al. (2019) showed that the difference between the MJO enhanced and suppressed phase over the MC mainly reveals itself in variations of the diurnal amplitude of precipitation, where the amplitude is larger during the enhanced phase and smaller during the suppressed phase. The differences are mainly attributed to changes in wind and moisture convergence and divergence patterns. Sakaeda et al. (2017) also observed a difference in the amplitude of the diurnal rainfall rates between both MJO phases over the MC, together with a delayed peak in rainfall during the MJO enhanced phase. Similar to our results, Sakaeda et al. (2017) also observed enhanced stratiform precipitation after peak convective rainfall during the enhanced phase, which might be causing the observed delay in peak rainfall. They conclude that convection is more organized during the MJO enhanced phase, leading to increased formation of stratiform anvil clouds with greater horizontal extents, which will contribute to increased total rainfall rates. The differences in the MJO's impacts over the Congo from other tropical regions such as the MC could be the result of differences in topography, where the MC consists of multiple islands of different sizes surrounded by the ocean, while the Congo basin sits in the center of the African continent containing dense tropical rainforest promoting intense convection, surrounded by land on three sides and the Atlantic Ocean in the west.

A limitation of this study is the usage of regional averaging over the entire study domain for the diurnal cycles and the atmospheric fields. This domain-wide averaging does not account for the fact that convection and precipitation varies spatially across the Congo basin and does not exclude grid-points which may not be raining. If including only the rainy points, for example during the enhanced phase, the specific divergence and vertical velocity patterns might be more pronounced when compared to including all grid points. Additionally, while this study discovers the impacts of the MJO on the diurnal cycles of convection and precipitation and explores some physical mechanisms leading to the observed changes, further work is needed to fully understand how the MJO modulates the diurnal variabilities of convection and rainfall. For example, explaining why the MJO is influencing the stratiform and convective precipitation differently could enhance our understanding about the MJO's impact on precipitation and may help to better resolve and simulate the MJO and associated variabilities in rainfall and convection, ultimately improving predictions of MJO modulated rainfall. Additional analysis on the impacts of the MJO on storm lifetime and initiation using high spatial and temporal resolutions data could also be useful to understand variations in the frequency, intensity, and duration of convective systems due to the MJO.

Overall, the results presented above answer the question of how the MJO, the most dominant intraseasonal variability in the tropics, impacts convection and precipitation over the Congo from a diurnal perspective and improve our understanding about factors influencing the diurnal cycle of convection and rainfall over tropical rainforests. Our findings are not only useful in identifying the main drivers of the observed long-term and large-scale drying trend that has been stressing the Congo Basin but also help in improving weather forecasts and model development. For example, one major finding of this study is that the impact of the MJO on convection and rainfall is greatest in the morning hours, influencing the stratiform portion of the rain more than the convective precipitation. Since the changes in rainfall and convection are largest during the morning hours when rainfall totals are usually lowest, the MJO could be used to predict exceptionally high precipitation rates in the morning. Additionally, considering that the MJO modulates convective and stratiform precipitation differently could help to predict the modulation of rainfall by the MJO more accurately.

CRediT authorship contribution statement:

Kathrin Alber: Conceptualization, Methodology, Software, Validation, Formal analysis, Investigation, Data curation, Writing – original draft, Visualization. **Liming Zhou:** Conceptualization, Writing – review & editing, Funding acquisition. **Paul E. Roundy:** Conceptualization, Writing – review & editing. **Stephen L. Solimine:** Data curation, Writing – review & editing

CHAPTER 5:

Impacts of drying soils on atmospheric stability and the diurnal cycle of convection over the Congo Basin

This chapter addresses research question 4) in Chapter 1.3 by using the WRF model to understand how a decrease in soil moisture influences atmospheric stability and convection. Two sets of simulations using different soil moisture initializations were conducted and ERA5 reanalysis data are used to provide initial and boundary conditions. For the experiment runs (EXP), soil moisture was decreased by 50% compared to the control runs (CTL), while the EXP and CTL runs were otherwise identical. By comparing the differences between the EXP and CTL runs, soil moisture impacts were quantified. Two 6-day case studies were investigated to examine the seasonal variations, i.e., one during the dry season (DJF) and one during the wet season (SON) over the region. The hypothesis of this study is that land surface properties such as soil moisture can impact the development of convection through modulation of the solar heating and the planetary boundary layer (PBL) and the subsequent influence on atmospheric temperature and humidity profiles.

5.1 Introduction

The Congo rainforest, the second largest rainforest on the planet, has been experiencing an increase in dry season length (Jiang et al. 2019) and a decrease in forest greenness (Zhou et al. 2014) as a result of an observed long-term drying trend over the region. As rainforests become increasingly drier, soil moisture can become a limiting factor if evapotranspiration increases while rainfall amounts are low (Jiang et al. 2019; Guan et al. 2015). Soil moisture can influence a variety of variables, such as the surface heat fluxes, the planetary boundary layer (PBL), and near surface relative humidity and temperature. Subsequently, soil moisture induced changes can cause modifications in the atmospheric circulation and stability and thereby impact the formation, propagation, and development of convective storms and precipitation. While several studies suggest a positive feedback between soil moisture and convection, with convective systems mostly being generated over wetter soils, some studies also show a negative feedback with decreased convective activity over wetter areas (Taylor and Ellis 2006; Liu et al. 2022).

For example, Pal and Eltahir (2001) suggest a positive feedback with higher soil moisture enhancing convection. They argument that an increase in soil moisture will increase evapotranspiration and the latent heat flux while decreasing the sensible heat flux. This may lead to lowered turbulent mixing and a shallower PBL, increasing the moist static energy as well as CAPE (i.e., amount of energy available for convection) and reducing CIN (i.e., energy needed to lift an air parcel to the level of free convection) and thereby enhancing convective activity. Higher soil moisture may also reduce albedo, leading to increased absorption of surface radiation.

On the other hand, studies such as Findell and Eltahir (2003) have shown a negative feedback between soil moisture and convection. According to their study, increased soil moisture may lead to decreased ground temperatures, increased surface air pressure, reduced PBL height, an increased vertical gradient of equivalent potential temperature and thus increased atmospheric stability. This reduces the sensible heat flux, decreases the thickness of the convective PBL, and leads to fewer air parcels being able to overcome CIN which may decrease convective activity. Thus, increased soil moisture may inhibit the vertical movement of air. In contrast, a decrease in soil moisture may limit evapotranspiration and the latent heat flux, increase surface temperatures, vertical velocity, PBL height, and reduce CAPE. Although reduced CAPE is not favorable for convection, the increased surface heating may make it easier for air particles to overcome CIN (Liu et al. 2022). Taylor and Ellis (2006) studied the interactions between soil moisture and precipitation using TRMM satellite precipitation data over the Sahel and found convection to be suppressed over wet soil during the afternoon and evening when compared to adjacent drier areas, contributing the decreased convection to suppressed convective initiation over wetter soils due to a shallower, moister, and cooler boundary layer.

Most previous studies analyzing these feedbacks are focused on regional hotspots of land-atmosphere interactions, which are mostly located in transitional zones between dry and wet climates, such as the U.S. Great Plains, the semiarid Sahel, Northern India, and the Mediterranean region (Koster et al. 2004; Seneviratne et al. 2006; Guo et al. 2006; Guo et al. 2011), while it is largely unknown how tropical rainforests will respond to droughts. Guan et al. (2015) showed that forest canopy photosynthetic activities are sensitive to water stress and co-vary with precipitation seasonality in the rainforests of Africa. They further suggest that with precipitation totals greater than 2000 $mmyr^{-1}$, tropical rainforests can sustain plant water needs throughout the year, inferring that water will not be a limiting factor for photosynthesis. With 90% of African tropical evergreen forests existing below the 2000 $mmyr^{-1}$ threshold, water storage from the wet season may not be able to satisfy plant water demands during the subsequent dry season. Thus, the observed long-term drying trend might result in a transition of the rainforest from higher-biomass, closed-canopy forests to lower-biomass, open-canopy forests (Zhou et al. 2014), with rainforests becoming another hotspot with strong land-atmosphere interactions, where evapotranspiration responds strongly to soil water availability and affects the subsequent PBL development and convection (Koster et al. 2004; Seneviratne et al. 2006; Guo et al. 2006; Guo et al. 2011).

Interestingly, despite the observed drying trend and the decreasing trend in precipitation (Zhou et al. 2014; Hua et al. 2016; Hua et al. 2018; and Jiang et al. 2019) convective activity over the Congo Basin has been observed to be increasing (Raghavendra et al. 2018; Taylor et al. 2018, Alber et al. 2021a; Alber et al. 2021b). Since changes in soil moisture can have impacts on atmospheric stability, convection, and precipitation as discussed above, it is crucial to understand how the observed drying trend may be impacting atmospheric stability and convection over the

Congo. Nevertheless, no other studies have investigated this issue to the author's knowledge. Thus, this study aims to close this knowledge gap by answering the open question of how a decrease in soil moisture will impact convection and atmospheric stability, from a diurnal perspective. The data and methods used, including a description of the model setup and verification, are presented in section 5.2, the results are described in section 5.3, and section 5.4 entails a discussion and conclusions.

5.2 Data and Methods

5.2.1 Model Setup

The NCAR advanced Weather Research and Forecasting (AWR-WRF) model version 4.4.1 was used in this study to simulate the effects of a decrease in soil moisture on convection over the study region, the Congo Basin. The study domain is defined as the area from 5°S to 5°N and 12°E to 30°E (Fig. 5.1). Two 192-hour (8-day) simulations were conducted where the first 48 hours were reserved for model stabilization and spin up and were discarded, resulting in two 6-day simulation periods that were analyzed. One dry season case (16-January to 21-January 2018) and one wet season case (21-October to 26-October 2019) was selected. Hourly European Centre for Medium Range Weather Forecast (ECMWF) ERA5 reanalysis data were used to provide initial and boundary conditions. The model was initialized at 00:00 UTC and run at a 4 km convection permitting resolution. Running the model at a 2 km resolution showed a minimal increase in model performance. 38 vertical levels and 511 longitude and 310 latitude grid points were used. The parameterization schemes are summarized in Table 5.1, where no cumulus parameterization schemes were used since the model was run at a convection permitting resolution to resolve convection more accurately. Several sensitivity tests were conducted to evaluate the performance of different WRF parameterization schemes and achieve the most accurate configurations. For the control runs (CTL), the WRF model was initialized with ERA5 data and run for the two selected case studies with no further changes. For the experiment runs (EXP), the soil moisture was decreased by 50% compared to the CTL runs, to simulate the decrease in soil moisture over the region. More specifically, the soil moisture was changed by decreasing the soil moisture of the ERA5 data used for initial conditions. No other changes were made compared to the CTL runs. A decrease of soil moisture by 25% showed similar, but less pronounced impacts (not shown).

The selected Noah land surface model has one canopy layer and one snow layer and includes the prognostic variables soil moisture, soil temperature, canopy moisture, snow depth, as well as surface and ground runoff accumulation. Soil moisture is simulated in four layers of increasing thickness at 0.1 m, 0.3 m, 0.6 m, and 1.0 m, with the depth of the total soil column being 2.0 m. The vegetation data are derived from MODIS land-cover and leaf area index (LAI) data (Srivastava et al. 2015; Wei et al. 2010). The Noah land surface model takes soil and vegetation processes into account to close the surface energy and water budgets (Wei et al. 2010; Zhuo et al. 2019). The root zone depth lies in the upper 1 m of the soil and varies spatially depending on the vegetation class while the layers below serve as a reservoir including drainage at the bottom due to gravity (Srivastava et al. 2015). Each layer's soil moisture (i.e., soil water movement and flow between soil layers) is calculated based on the mass conservation law and the diffusivity form of the Richard's equation, while infiltration is controlled by a conceptual parameterization taking soil moisture and precipitation into account. Evapotranspiration is calculated using the Ball-Berry equation and considers the canopy intercepted water evaporation, transpiration from vegetation canopies, and evaporation from the soil (Achugbu et al. 2020; Srivastava et al. 2015; Zhuo et al. 2019).

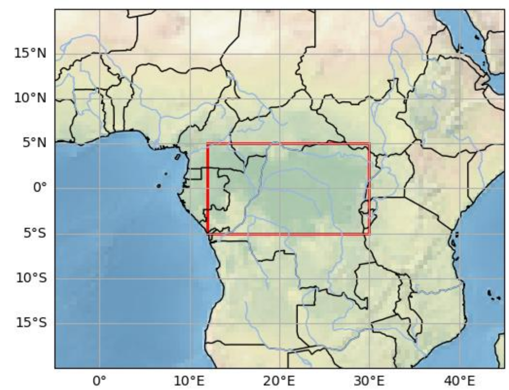

Figure 5.1: Map of Africa and the study domain (i.e., the Congo Basin) which is depicted by the red box.

Table 5.1: Selected WRF parameterization schemes.

Model Physics	**Parameterization Scheme Used**
Longwave radiation	Rapid Radiation Transfer Model *(Mlawer et al. 1997)*
Shortwave radiation	Dudhia scheme *(Dudhia 1989)*
Surface layer	Monin-Obukhov surface layer scheme *(Jiménez et al. 2012)*
Boundary layer	Yonsei University (YSU) boundary layer parameterization scheme *(Hong et al., 2006)*
Land surface	Noah land surface scheme *(Chen and Dudhia 2001; Ek et al. 2003)*
Microphysics	Thompson microphysics scheme *(Thompson et al. 2008)*
Convection	No scheme used since model was ran at 4 km convection permitting resolution.

5.2.2 Satellite Data used for Model Validation

Due to the scarcity of surface observation and in-situ measurements over the Congo as well as the decreasing number of rain gauges available since 1980 (Washington et al. 2013), two different satellite datasets were used for the model validation, i.e., the GridSat-B1 and TRMM satellite data. From the GridSat-B1 data (Knapp 2008; Knapp et al. 2011), infrared (IR) 11 μm channel brightness temperature (T_b) was derived to identify convective clouds. The GridSat-B1 T_b, sampled by the European Meteorological (MET) series of geostationary satellites from the International Satellite Cloud Climatology project (ISCCP; Schiffer and Rossow 1983) is available at a 3-hourly temporal and a 0.07° × 0.07° spatial resolution. The GridSat-B1 T_b data was used for comparison to the WRF model derived T_b from the CTL run to validate the time series and spatial patterns of convective clouds. The T_b from the WRF CTL run was converted from model OLR by using the Stefan-Boltzman law for a more accurate comparison between the model output and satellite observations (Yang and Slingo 2006).

TRMM satellite precipitation data was used for comparison to the modeled precipitation, since the TRMM dataset has been shown to perform well over the Congo by several different studies such as Munzimi et al. (2015) and Nicholson et al. (2019). More specifically, the TRMM 3B42 product was used, which is available at a 3-hourly temporal and a 0.25° × 0.25° spatial resolution from 1998 to 2019. The data was acquired from NASA's Goddard Earth Sciences Data and Information Services Center (https://disc.gsfc.nasa.gov/datasets/TRMM_3B42_7/summary).

5.2.3 Model Validation

To evaluate the WRF model performance in reproducing clouds and precipitation, WRF model derived T_b and precipitation 6-day time series averaged over the study domain, as well as spatial patterns from the CTL run were compared to the satellite derived T_b (GridSat-B1) and precipitation (TRMM). The model simulated T_b captures the diurnal structures and matches the satellite derived T_b reasonably well (Figs. 5.2a and b). The correlations between the model and satellite T_b time series are significant with R=0.79 ($p<0.01$) for the dry season case and R=0.70 ($p<0.01$) for the wet season case. As expected, the skill of the WRF model to simulate precipitation is lower (Figs. 5.2c and d). However, the CTL and TRMM derived precipitation data are still significantly correlated, with R values of 0.59 ($p<0.01$) for the dry season case and R=0.5 ($p<0.01$) for the wet season case.

Additionally, the spatial patterns of the WRF T_b are compared to the GridSat-B1 T_b patterns over the study domain at 6-hourly time steps for the dry season case (Fig. 5.3) and the wet season case (Fig. 5.4). The model is mostly able to capture the spatial extent and propagation of thunderstorms over the Congo Basin. For the dry season case, storms are simulated reasonably well for day 1 to 4, where the model is mostly able to reproduce the spatial extent, location, and intensity of the storms. For day 5, the locations of the storms are too far to the east, and for day 6 the model does not capture the storms at the southern border of the domain very accurately. For the wet season case, days 1, 2 and 4 are reasonably simulated, while the intensity is overestimated for days 3 and 6. For day 5, the intensity is first overestimated and then underestimated.

Overall, the WRF model simulates T_b and precipitation reasonably well and captures general spatial patterns and diurnal time series, with some deviations from the observations being expected.

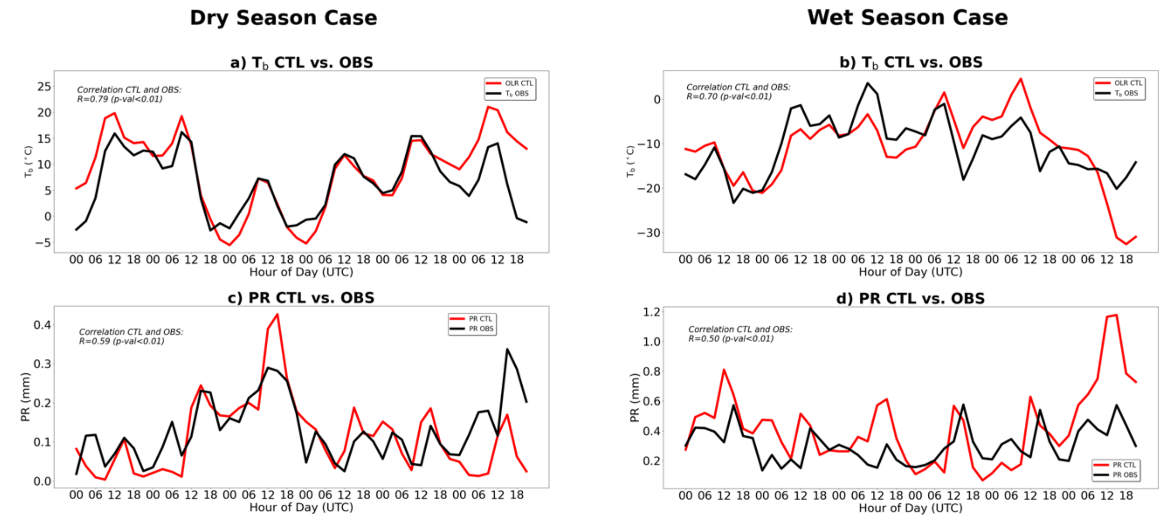

Figure 5.2: Spatially averaged (**a**), (**b**) T_b from the CTL run (red) and GridSat-B1 satellite data (black), and (**c**), (**d**) rainfall from the CTL run (red) and TRMM satellite data (black), for the dry season case (16-21 January 2018; left) and the wet season case (21-26 October 2019; right) over the study domain.

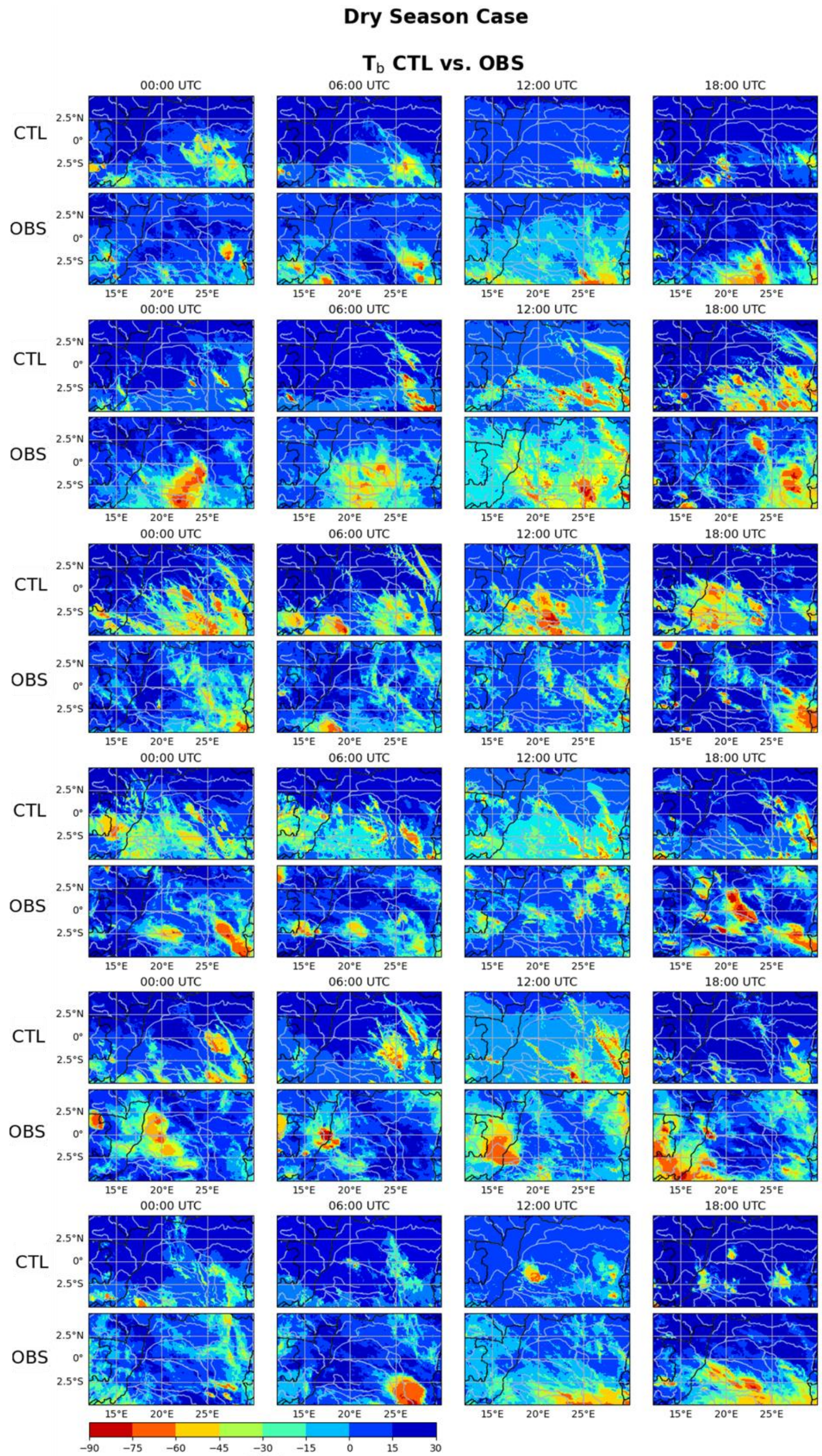

Figure 5.3: Spatial evolution of T_b from the CTL run (respective top rows) and from GridSat-B1 (OBS; respective bottom rows) from 16-21 January 2018 (dry season case) over the study domain, shown every 6 hours.

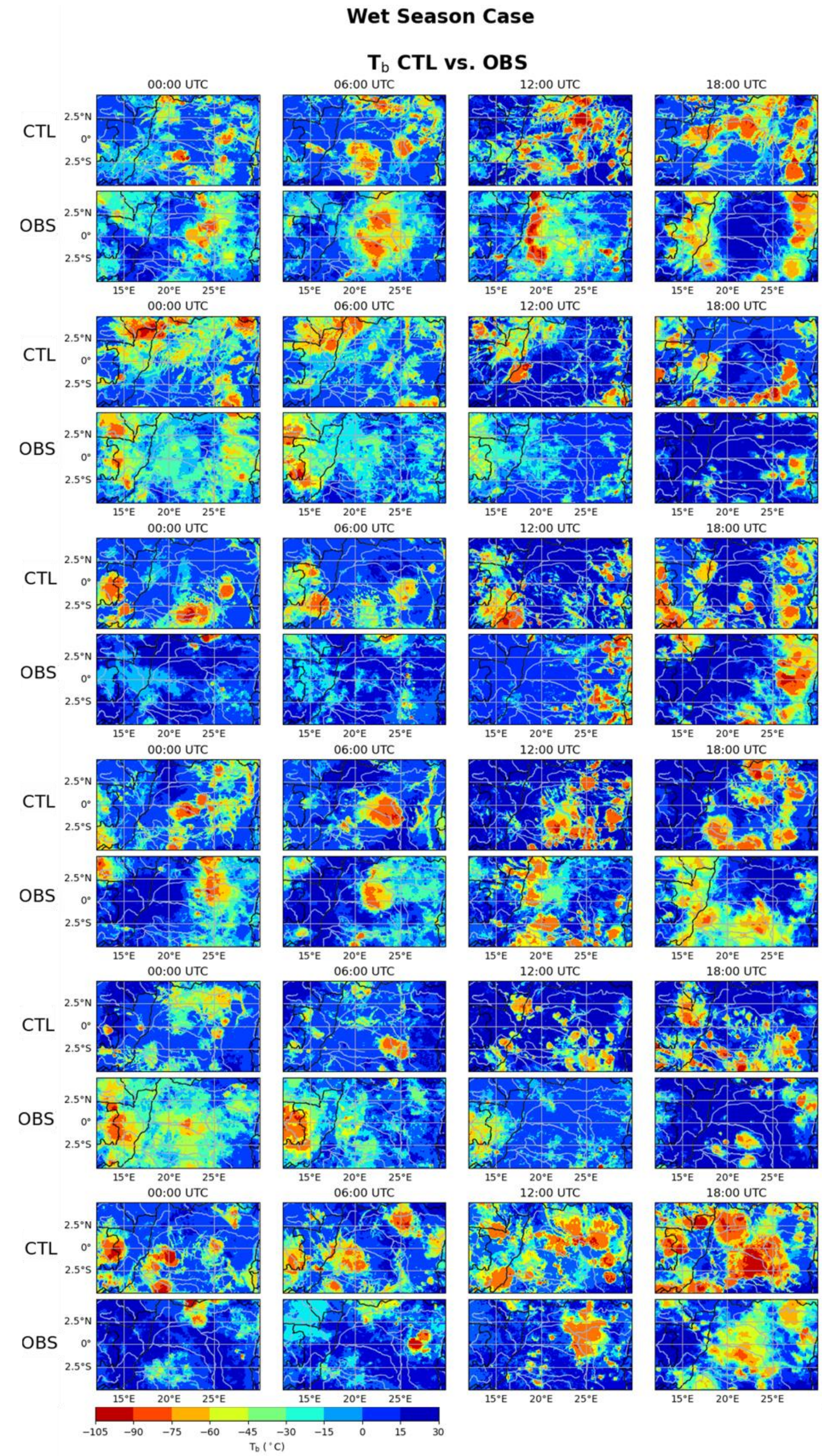

Figure 5.4: Spatial evolution of T_b from the CTL run (respective top rows) and from GridSat-B1 (OBS; respective bottom rows) from 21-26 October 2019 (wet season case) over the study domain, shown every 6 hours.

5.2.4 Gálvez -Davison Index

The Gálvez-Davison Index (GDI) was used to estimate the potential for convection in addition to CAPE and CIN. The GDI is a thermodynamic index developed by Michel Davison and José Gálvez at NOAA's Weather Prediction Center (WPC). It consists of different sub-indices, where each sub-index evaluates different thermodynamic process in the mid- and low troposphere. The Column Buoyancy Index (CBI) analyzes the availability of heat and moisture in the mid- and low troposphere, the Mid-Tropospheric Warming Index (MWI) considers the stabilizing and destabilizing effects of mid-level ridges and troughs, and the Inversion Index (II) evaluates the entrainment of dry air and stabilization associated with trade wind inversions. One major advantage of the GDI is that changes in convective potential can be attributed to changes of different thermodynamic processes by evaluating the sub-indices separately. For the calculation of the GDI, temperature and specific humidity values at 950 hPa, 850 hPa, 700 hPa, and 500 hPa are needed. For this study, model derived temperature and specific humidity data were used to calculate the GDI. The reader is referred to Gálvez and Davison (2016) and Alber et al. (2021a) for a complete derivation of the GDI.

5.3 Results

5.3.1 Impacts on surface heat fluxes, temperature and humidity profiles, LCL, and PBL

The impacts of a decrease in soil moisture on the surface heat fluxes, temperature and humidity profiles, LCL and PBL height are analyzed first, since changes in soil moisture can modulate convection through changes in the partitioning of the surface heat fluxes, as well as in changes in atmospheric temperature and humidity profiles, which will impact the LCL and PBL height. The 6-day composites of the sensible and latent heat fluxes for the CTL and EXP runs are illustrated in Fig. 5.5 for both cases. As expected, the decrease in soil moisture changes the partitioning of the energy fluxes, where the sensible heat flux is generally increased, and the latent heat flux is decreased during the EXP run. The differences between the CTL and EXP run are highest between 10:00 UTC and 12:00 UTC when the heat fluxes are at a maximum. However, there is no observed shift in the diurnal cycle when comparing the EXP and CTL runs.

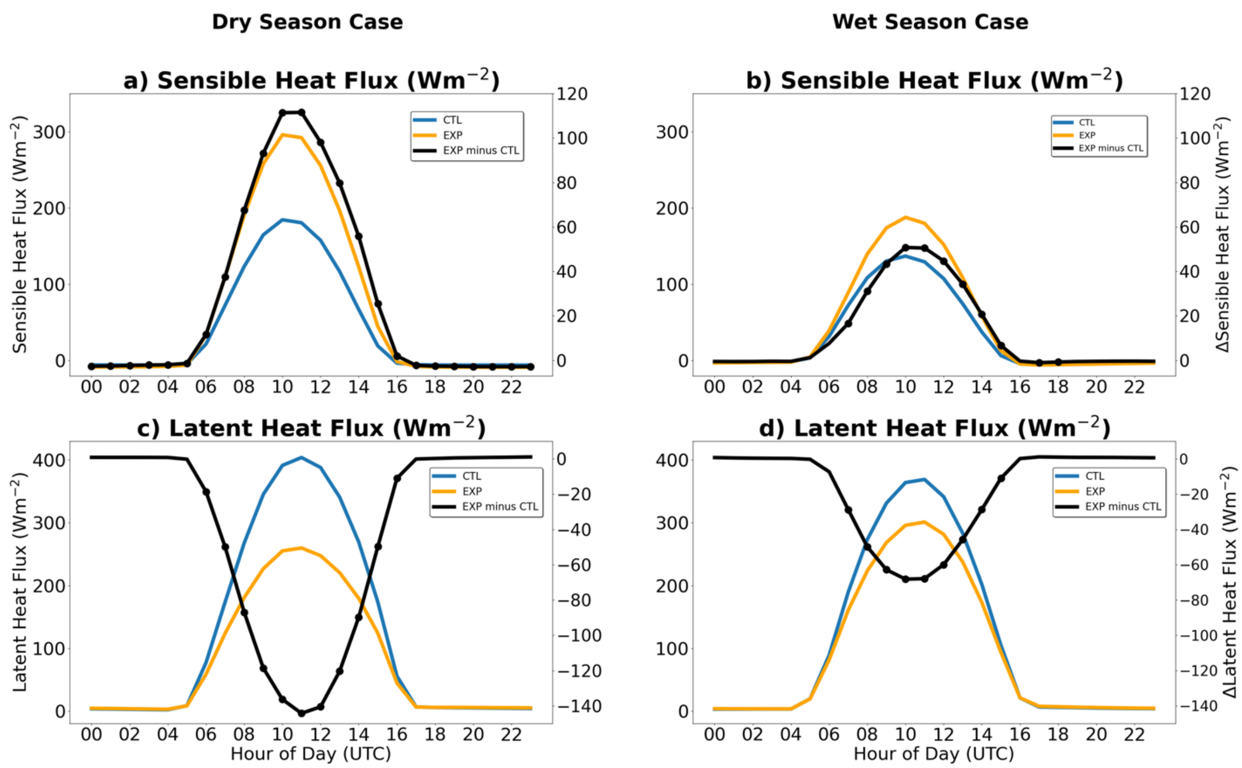

Figure 5.5: Diurnal cycle of the (**a**), (**b**) sensible and (**c**), (**d**) latent heat fluxes for the dry season case (left) and the wet season case (right), for the CTL run (blue; left y-axis), the EXP run (orange; left y-axis), and the difference between the two (black; right y-axis). The values are averaged over all 6 days and the study domain. Black dots indicate that the difference is significant at p<0.1 (determined using a two-sample t-test).

To investigate the impacts of drier soils on atmospheric temperature and humidity profiles, the 6-day time-height composites for temperature, water vapor mixing ratio, relative humidity, and equivalent potential temperature are illustrated in Fig. 5.6. For the lower atmospheric levels (below 700 hPa), the temperature is generally increased during the EXP run, where the differences are most pronounced in the afternoon around 15:00 UTC during the dry season case and around 13:00 UTC during the wet season case (Fig. 5.6a and b). Additionally, a slight but not significant decrease in temperatures is observed in the early morning hours during the EXP run. From around 700 hPa to 550 hPa, there is a distinct area of decreased temperatures during the EXP run. The differences aloft are less pronounced and not statistically significant. Comparing the dry season and the wet season case, the differences between the CTL and EXP run are generally higher during the dry season, where the strip of colder temperatures around 600 hPa is more pronounced during the dry season case while it is not statistically significant during the wet season case. The water vapor mixing ratio (Figs. 5.6c and d) shows a similar pattern, with a decrease in water vapor mixing ratio below 700 hPa, an increase between 700 hPa and 550 hPa, and smaller differences aloft. The same pattern can be observed for the relative humidity and equivalent potential temperature profiles as well (Fig. 5.6e-h), with decreased values during the EXP run below 700 hPa, an increase right above from around 700 hPa to 550 hPa, and smaller differences aloft. The differences are again more pronounced during the dry season case. Overall, a decrease in soil moisture in the EXP run leads to increased temperatures, decreased moisture, relative humidity, and equivalent potential temperature in the levels below 700 hPa, where the differences are most pronounced in the early afternoon. Right above, around 600 hPa, there is a distinct narrow area showing opposite signals, i.e., decreased temperature, and increased moisture, relative humidity, and equivalent potential temperature, while the levels above 550 hPa do not show a clear pattern. When comparing the changes in temperature to the changes in water vapor mixing ratio, it becomes apparent that the changes in moisture are more pronounced.

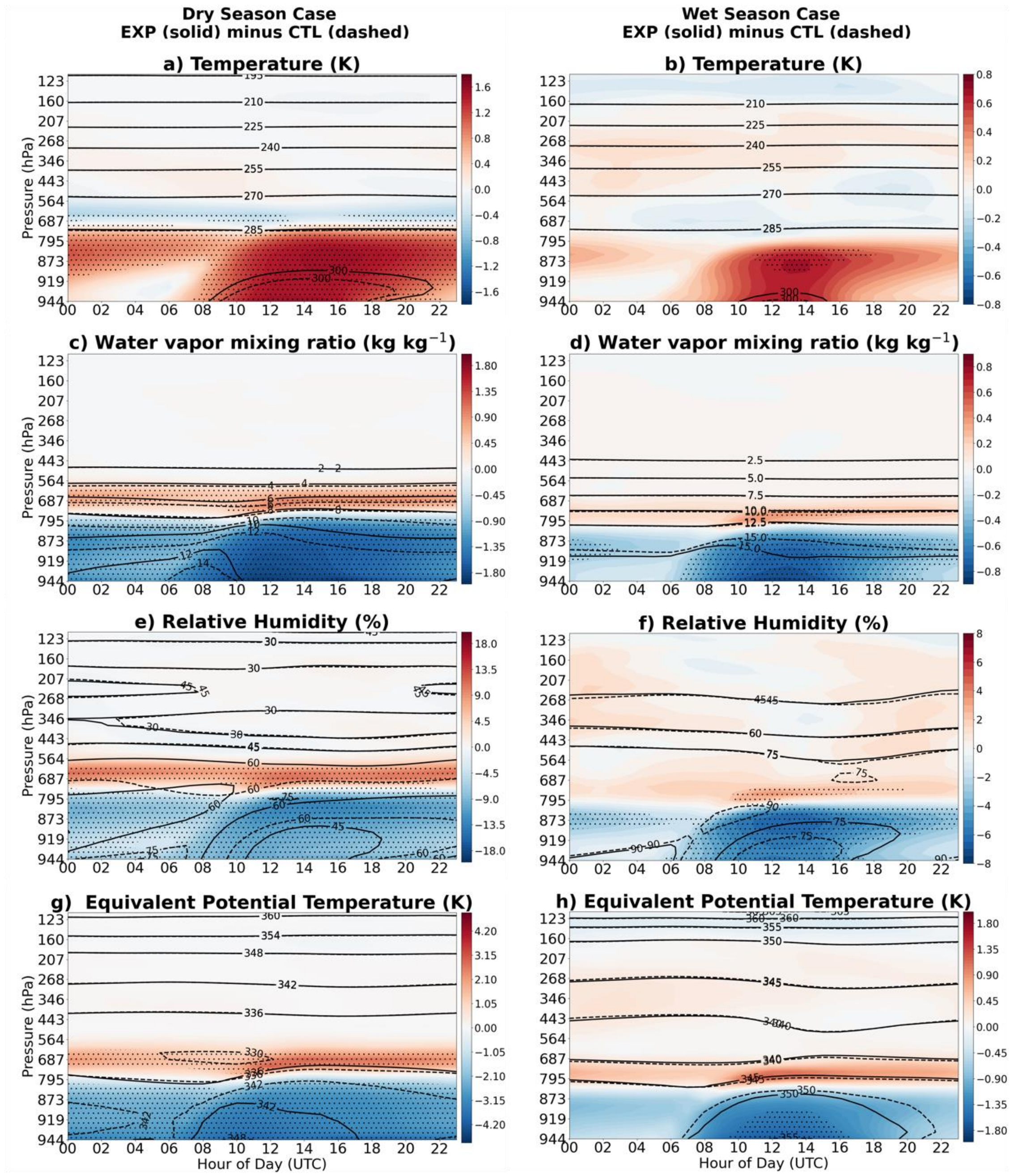

Figure 5.6: Time-height cross section composites of (**a**), (**b**) temperature (K), (**c**), (**d**) water vapor mixing ratio ($10^{-3} \times$ kg kg $^{-1}$), (**e**), (**f**) relative humidity (%), and (**g**), (**h**) equivalent potential temperature (K) values for the CTL run (dashed lines), the EXP run (solid lines), and the differences between the EXP and the CTL run (shading) for the dry season case on the left side and the wet season case on the right side. All values are averaged over all 6 days and the study domain. Stippling indicates that the difference is significant at $p<0.1$ (determined using a two-sample t-test).

Figs. 5.7a and b show the diurnal cycles of the LCL for both the wet and the dry season case. The LCL is lowest in the morning for both cases and reaches a maximum in the afternoon around 14:00 UTC. The LCL is generally higher during the EXP run, where the difference between the EXP and CTL run is largest in the early afternoon when the LCL is highest. Figs. 5.7c and d highlight the changes in PBL height. The PBL height is increased during the EXP run, where the differences are largest around noon, similar to the changes in the LCL. Both the increase in LCL and PBL height are possibly the result of the drier and warmer surface air layer. The changes in the LCL height are discussed in more detail below.

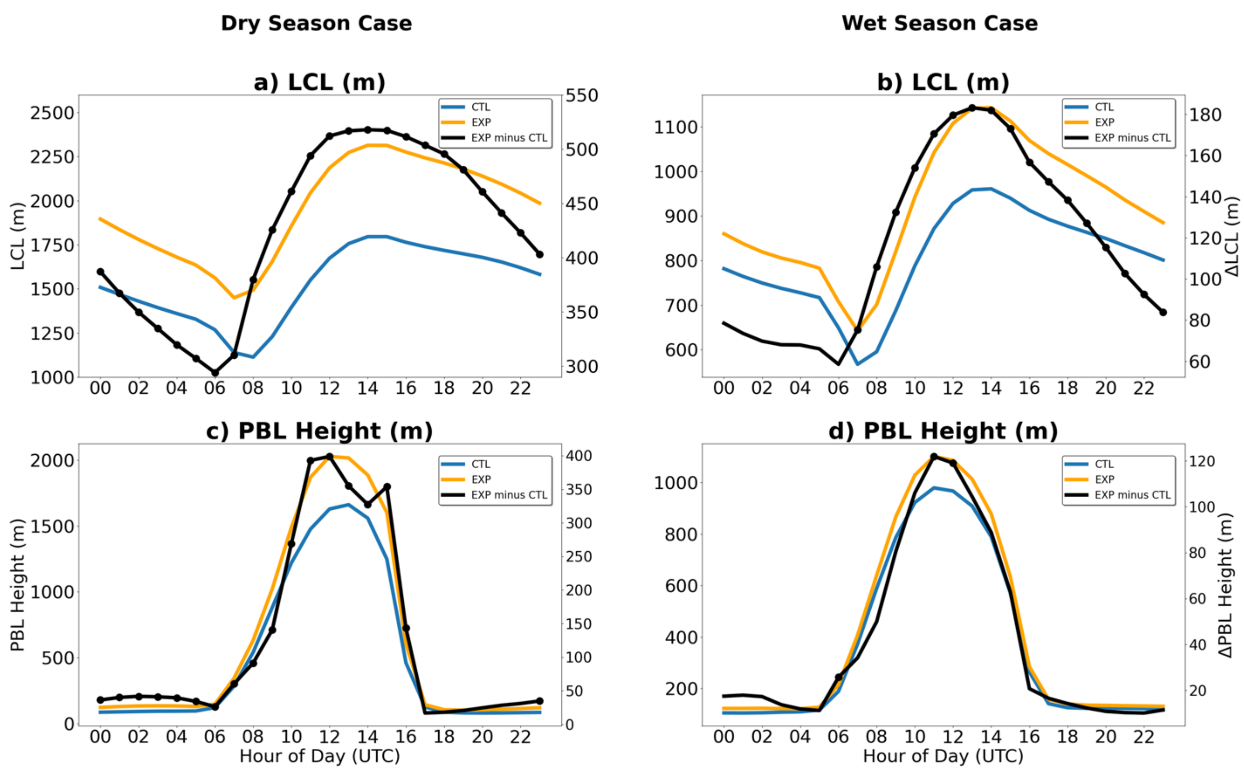

Figure 5.7: Diurnal cycles of the (**a**), (**b**) LCL (m), and (**c**), (**d**) PBL (m) height, for the dry season case (left) and the wet season case (right), for the CTL run (blue line; left y-axis), the EXP run (orange line; left y-axis), and the difference between the two (black; right y-axis). Averaged over all 6 days and the study domain. Black dots indicate that the difference is significant at $p<0.1$ (determined using a two-sample t-test).

5.3.2 Impacts on atmospheric stability and convective potential

In a next step, the impacts of a decrease in soil moisture on atmospheric stability and convection are analyzed by evaluating different tools and variables such as Skew-T diagrams, CAPE, CIN, and the GDI. Figs. 5.8 and 5.9 show Skew-T diagrams for the CTL (dotted lines) and EXP (solid lines) runs averaged over all 6 days at 6-hourly time steps, i.e., 00:00 UTC, 06:00 UTC, 12:00 UTC, and 18:00 UTC, for the dry and wet season case, respectively. Although the diagrams only show results at 6-hourly time steps, the other hours have similar results. As illustrated by the temperature (red) and dewpoint (green) lines, a parcel at the surface is generally warmer and has a lower dewpoint (i.e., less moisture) during the EXP run. The parcel paths, depicted by the black lines, indicate that a parcel in the EXP run is warmer than in the CTL run in the lower levels, before becoming colder compared to the CTL run at higher levels. While a parcel is lifted from the surface, it cools at the dry adiabatic lapse rate (i.e., 9.8°C / 1000m) and eventually reaches saturation, i.e., the LCL, which is depicted by the black dots in the Skew-T diagrams. Since a parcel in the EXP run contains less moisture and has a higher temperature at the surface, it takes longer for the parcel to reach saturation while ascending at the dry adiabatic lapse rate and thus, the LCL is higher compared to the CTL run. After reaching the LCL, the parcel will subsequently cool at the moist adiabatic lapse rate (~5°C / 1000m) and will therefore be cooling at a slower rate. Since a parcel during the EXP run takes longer to reach saturation, the change to cooling at the moist adiabatic lapse rate will take place at a higher atmospheric level when compared to the CTL run. Thus, a parcel in the EXP run will cool at a faster rate (i.e., at the dry adiabatic lapse rate) compared to a parcel in the CTL run at the same level, before reaching saturation and changing to cooling at the moist adiabatic lapse rate. This slower change from the dry adiabatic to the moist adiabatic lapse rate in the EXP run results in a parcel being warmer in the lower levels and colder aloft when comparing the EXP to the CTL run. This may also help to partially explain the band of decreased temperature and increased moisture from 700 hPa to 550 hPa during the EXP run. The

Skew-T diagrams further show that the difference between the EXP and CTL run are higher for the dew point than for the temperature, suggesting that the changes in moisture due to a decrease in soil moisture have a greater impact on changes in the LCL height and the parcel path than the changes in temperature. Looking at the vertical wind profiles, the differences between the EXP and CTL run are minimal.

To further investigate the impacts of drier soils on convective potential, Fig. 5.10 shows the composited diurnal cycles of maximum CAPE and CIN for both cases. The maximum CAPE and CIN are calculated by considering a parcel with maximum θe in the lowest 3000 m. A 500 m deep parcel is then calculated, which is used to compute CAPE and CIN. Generally, there is a minimum in CAPE in the morning around 06:00 UTC and a maximum right before noon. CIN shows the opposite pattern, with a maximum during the nighttime and the early morning and a minimum right before noon. Comparing CAPE and CIN for the EXP and CTL runs, CAPE is lower during the EXP run for both cases (Figs. 5.10a and b) while CIN is generally higher (Figs. 5.10c and d). Consequently, these results suggest that there is less energy available for convection (i.e., decreased CAPE), while more energy is needed to lift an air parcel adiabatically to the LCL (i.e., increased CIN). The diurnal cycles of CAPE and CIN are similar for the EXP and CTL runs but show a slight shift to an earlier peak of CAPE and an earlier minimum in CIN during the EXP run.

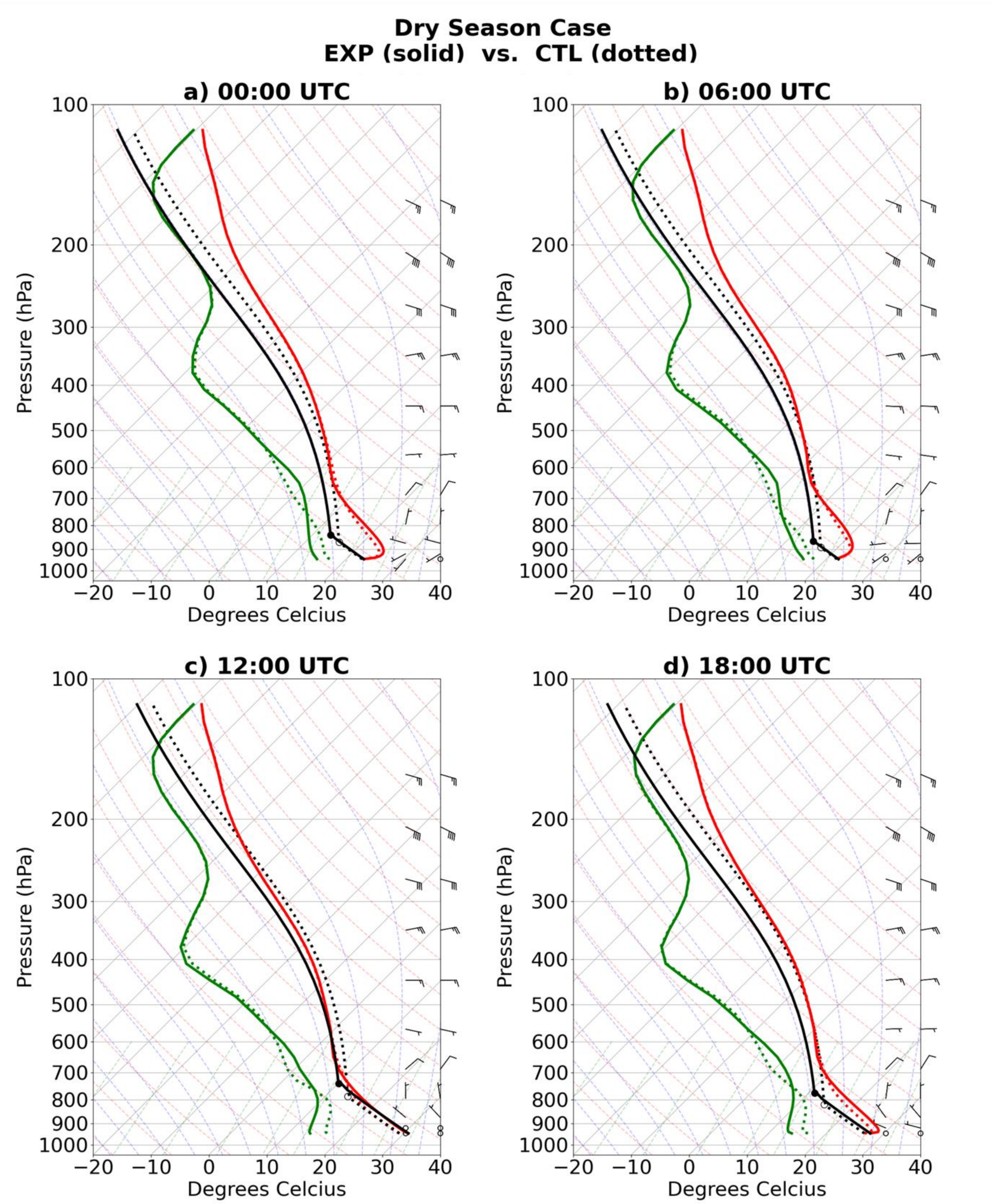

Figure 5.8: Skew-T diagrams for the dry season case for different hours of day. Values are averaged over all 6 days for the respective hour. The red lines indicate the temperature, the green lines indicate the dew point, and the black lines show the parcel paths for the EXP run (solid lines) and the CTL run (dotted line). Wind barbs (knots) are shown for the CTL (left) and the EXP (right) runs.

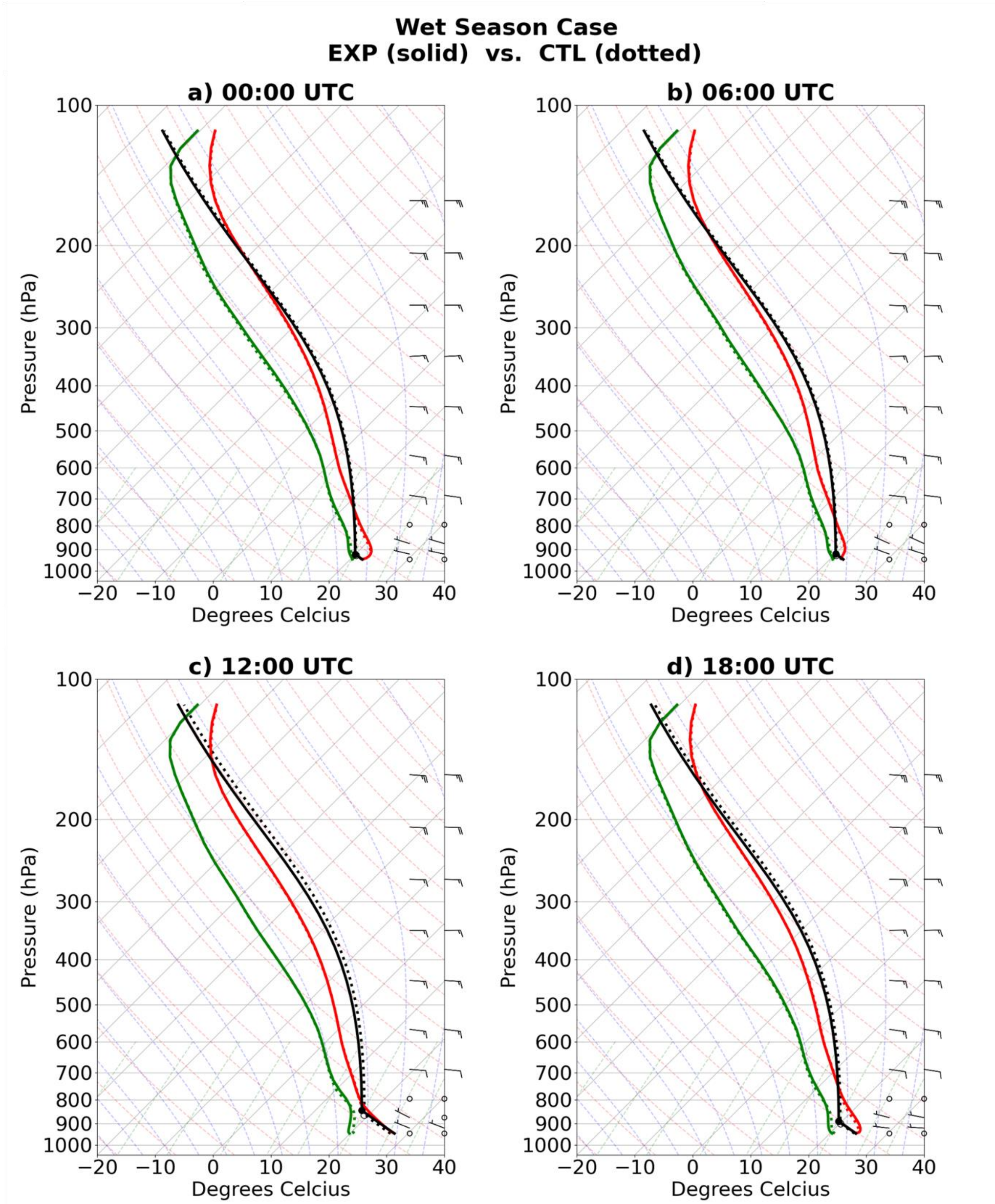

Figure 5.9: Skew-T diagrams for the wet season case for different hours of day. Values are averaged over all 6 days for the respective hour. The red lines indicate the temperature, the green lines indicate the dew point, and the black lines show the parcel paths for the EXP run (solid lines) and the CTL run (dotted line). Wind barbs (knots) are shown for the CTL (left) and the EXP (right) runs.

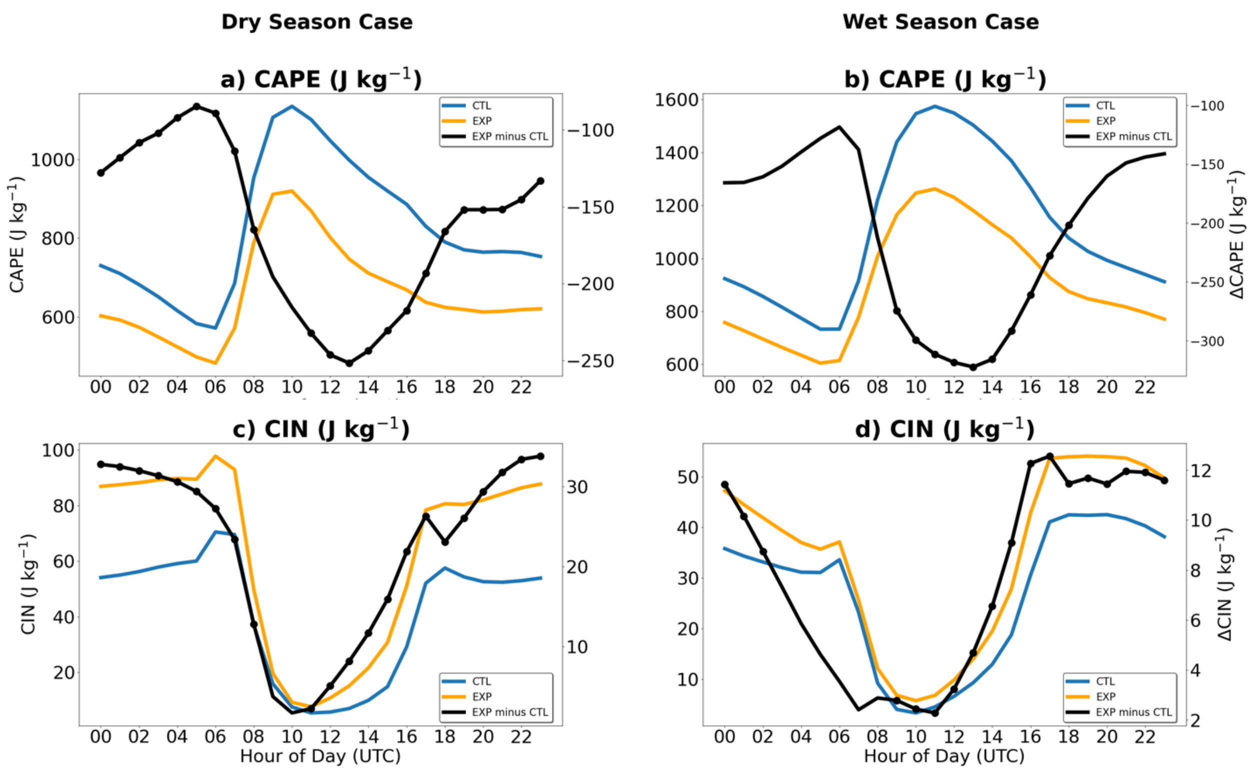

Figure 5.10: Diurnal cycle of (**a**), (**b**) maximum CAPE, and (**c**), (**d**) maximum CIN for the dry season case (left) and the wet season case (right), for the CTL run (blue line; left y-axis), the EXP run (orange line; left y-axis), and the difference between the two (black; right y-axis). Averaged over all 6 days and the study domain. Black dots indicate that the difference is significant at $p<0.1$ (determined using a two-sample t-test).

In Fig. 5.11, the impacts of a decrease in soil moisture on the potential for convection are investigated further by looking at changes in the GDI and its sub-indices. Similar to the diurnal cycle of CAPE, Figs. 5.11a and b show a minimum in the GDI in the early morning and a maximum around noon. For the dry season case (Fig. 5.11a), the GDI is generally decreased (i.e., decreased convective potential) during the EXP run with the differences being significant in the afternoon and evening hours, which is consistent with the observed changes in CAPE and CIN during the EXP run. The differences in the GDI between the EXP and CTL run for the wet season case (Fig. 5.11b) are very small and not significant. To investigate the changes in the GDI further, Figs. 5.11c to h analyze changes in the sub-indices of the GDI. The CBI (Figs. 5.11c and d) evaluates the moisture availability and temperature at 950 hPa and 500 hPa by calculating the θ_e of the respective layer. Higher values are indicative of a larger potential for deep convection, since a warm and moist mid tropospheric layer, reinforced by a warm and moist lower tropospheric layer suggests the presence of a deep moist layer, which will enhance convective activity. The observed decrease of the CBI in the EXP run during both cases thus suggests that the decreased potential for convective activity is associated with decreased moisture availability. Figs. 5.11e and f show minor and insignificant differences in the MWI between the EXP and CTL run, which analyzes mid-level warming and cooling at 500 hPa. Looking at the differences in the II, Figs. 5.11g and h reveal that the values are less negative during the EXP run, indicating weaker stabilization and thus an increased potential for convection during the EXP run. To investigate this further, the two sub-indices of the II, the II_S and the II_D are analyzed separately in Fig. 5.12. The II_S considers the difference in temperature between 950 hPa and 700 hPa, with lower values indicating stronger stabilization. The II_S values are higher during the EXP run for both cases (Figs. 5.12a and b), and subsequently indicate weaker stabilization and a higher potential for convection during the EXP run. Similarly, the II_D (Figs. 5.12c and d) shows less negative values during the EXP run, which suggests a decreased θ_e gradient with height, resulting in enhanced convection and thunderstorm activity. Consequently, the less negative II during the EXP run suggests increased thunderstorm potential with decreased soil moisture, despite the observed overall decrease in GDI (and CAPE). Overall, the decreased GDI during the dry season case can mostly be attributed to a decrease in CBI (i.e., decreased moisture availability), whereas the less negative II values (i.e., decreased stabilization) in turn act to increase the GDI during the EXP run. Consequently, while the GDI is decreased during the EXP run, indicating decreased convective potential with drier soil conditions, a decrease in soil moisture may also result in decreased stabilization through increased temperature differences between low and mid-level layers, as well as a decrease of the θ_e gradient with height. This, in turn, acts to enhance convective activity. From a diurnal standpoint, the peak in GDI shifted to a slightly earlier time of day, which is consistent with the small shift observed in CAPE and CIN.

In summary, a decrease in soil moisture over the study domain leads to a decrease in CAPE and the GDI, and an increase in CIN. This suggests that drier soils are associated with decreased convective potential due to decreased moisture availability. However, while an overall decrease in convective potential is observed, certain effects triggered by a decrease in soil moisture (i.e., an increased temperature gradient and a decrease in the θ_e gradient with height) may counteract the reduced potential for convection by decreasing atmospheric stability.

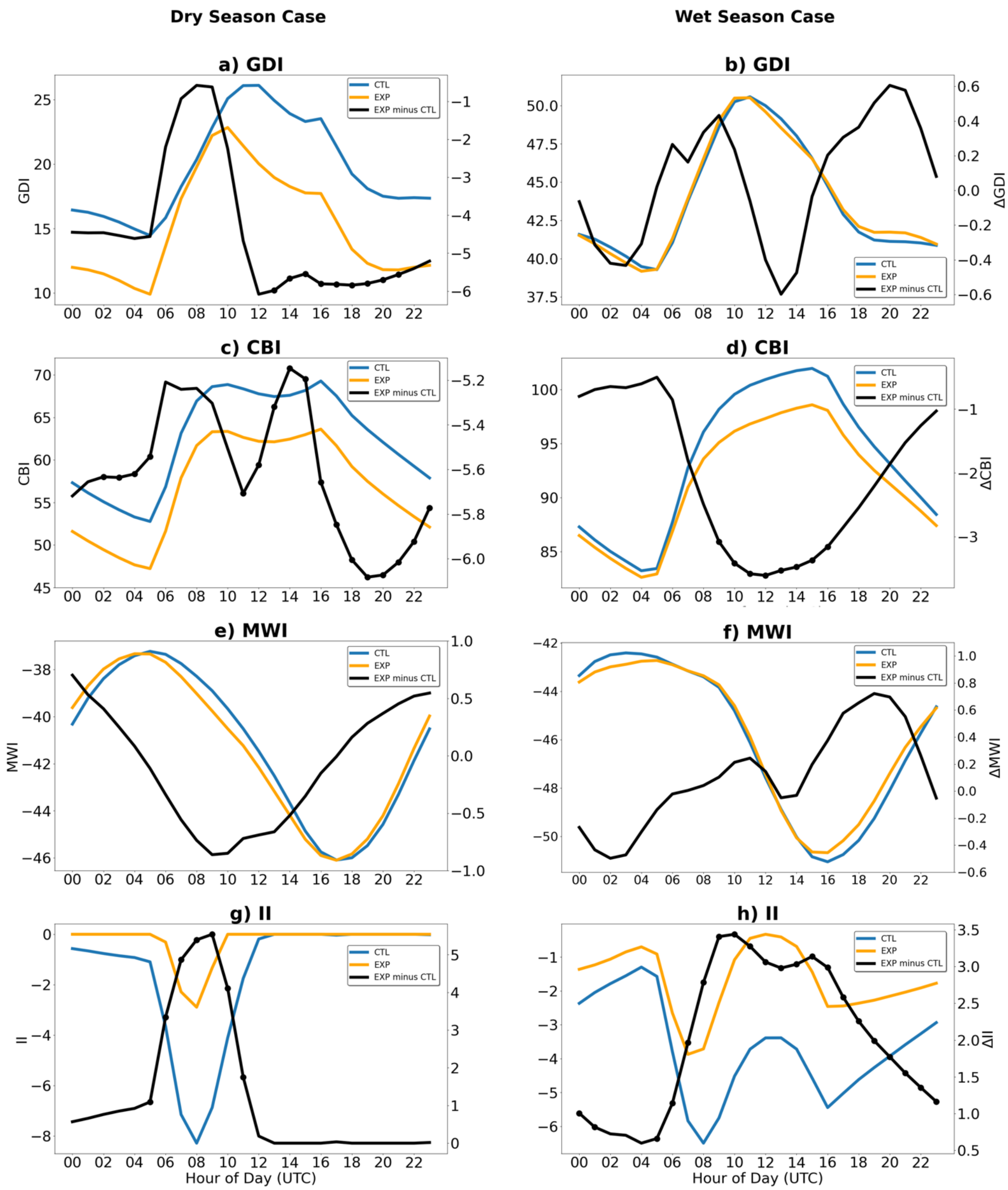

Figure 5.11: Diurnal cycles of the (**a**), (**b**) GDI, (**c**), (**d**) CBI, (**e**), (**f**) MWI, and (**g**), (**h**) II, for the dry season case (left) and the wet season case (right), for the CTL run (blue line; left y-axis), the EXP run (orange line; left y-axis), and the difference between the two (black; right y-axis). Averaged over all 6 days and the study domain. Black dots indicate that the difference is significant at $p<0.1$ (determined using a two-sample t-test).

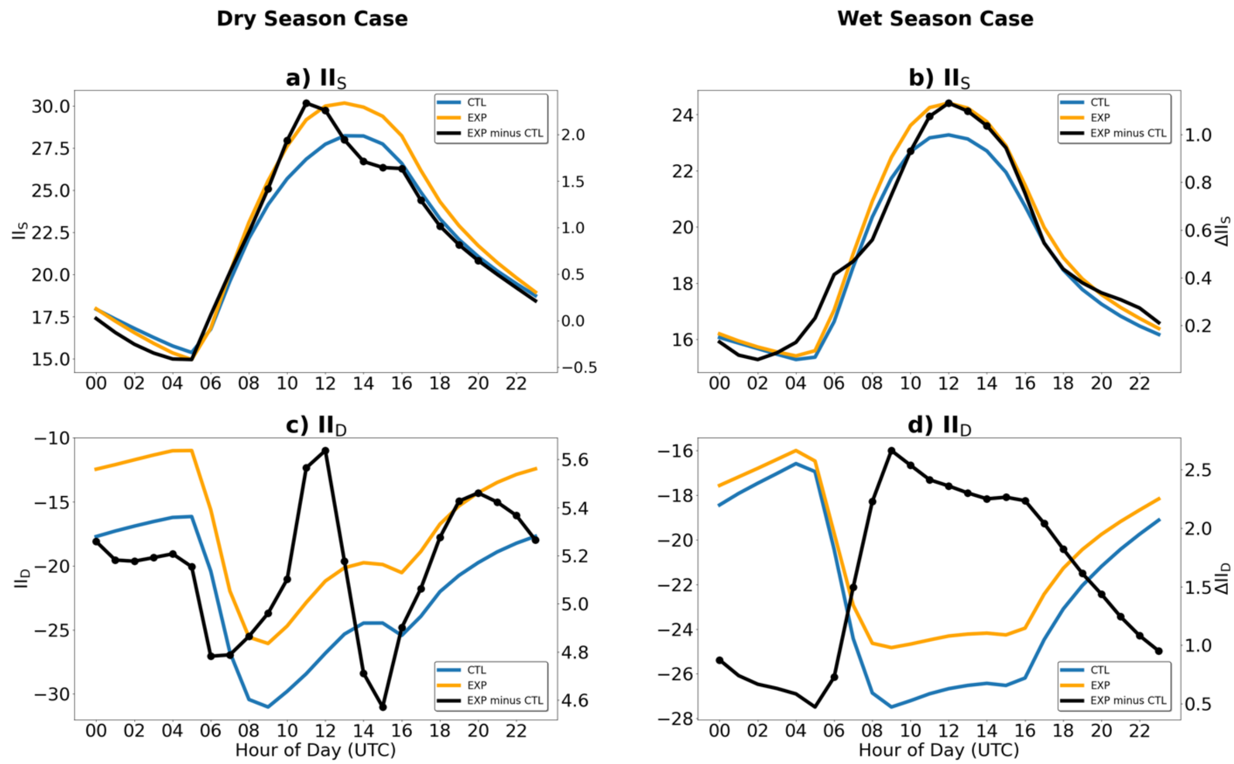

Figure 5.12: Diurnal cycles of the (**a**), (**b**) II$_S$, and (**c**), (**d**) II$_D$, for the dry season case (left) and the wet season case (right), for the CTL run (blue line; left y-axis), the EXP run (orange line; left y-axis), and the difference between the two (black; right y-axis). Averaged over all 6 days and the study domain. Black dots indicate that the difference is significant at $p<0.1$ (determined using a two-sample t-test).

5.3.3 Impacts on cloud fractions and precipitation

To investigate changes in clouds associated with a decrease in soil moisture, Fig. 5.13 illustrates differences in cloud fraction between the EXP and CTL run. Figs. 5.13a and b analyze the diurnal cycles of total cloud fraction, i.e., the average cloud fraction for all layers. The total cloud fraction is slightly increased during the EXP run for both cases, despite the observed decrease in CAPE and the GDI. However, the differences between the EXP and CTL runs are not significant for either case. Additionally, Figs. 5.13c and d show the time-height cross section composites for the cloud fraction over the study domain. Clouds are decreased in the lower-level during the EXP run and increased in the mid- and upper levels. The changes are significant in the lower and mid-layers for both cases, while the changes are not significant in the upper levels. The observed significant changes in clouds may be the effect of the detected decrease in moisture and increase in temperature (decrease in low-level clouds) and the associated increase of the LCL and PBL height (increase in mid-level clouds).

Figure 5.14 shows the composited diurnal cycles of precipitation for the two cases, where the differences are small and not statistically significant, suggesting that a decrease in soil moisture may have limited impacts on precipitation over the region.

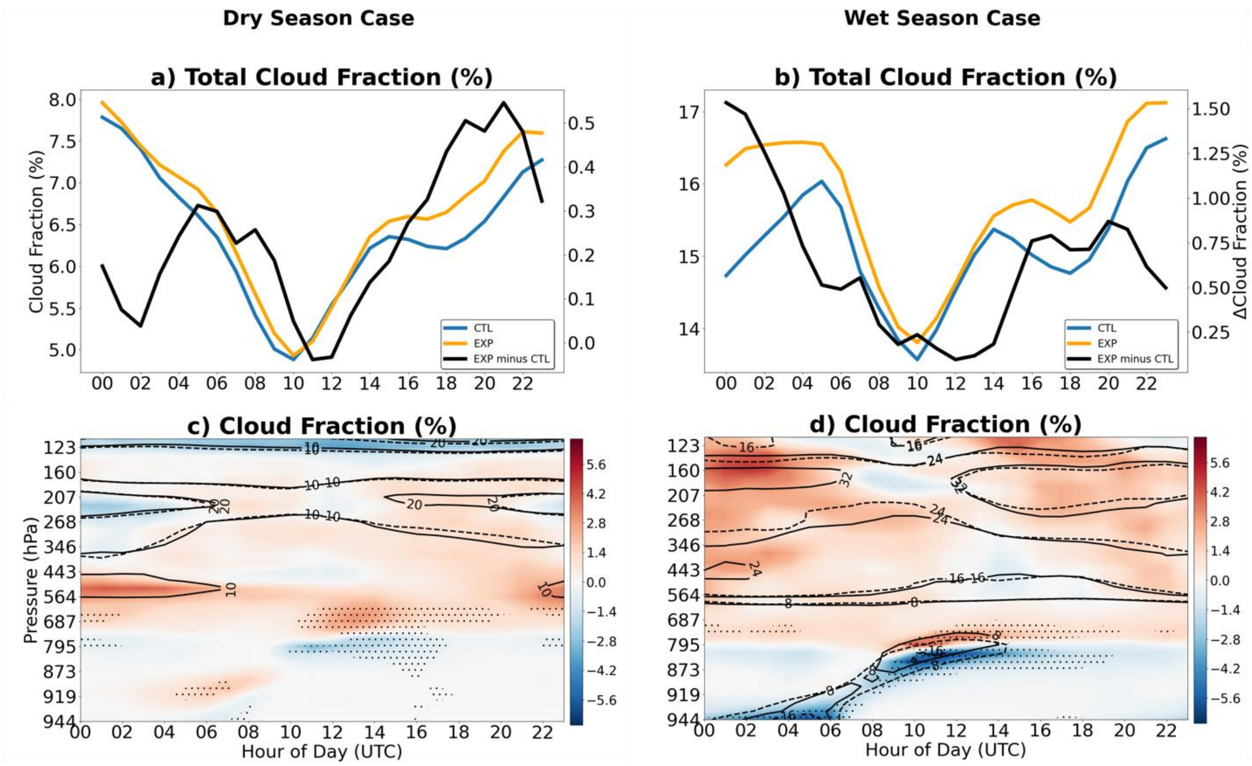

Figure 5.13: (**a**), (**b**) Diurnal cycles of total cloud fraction (%) for the dry season case (left) and the wet season case (right), for the CTL run (blue line; left y-axis), the EXP run (orange line; left y-axis), and the difference between the two (black; right y-axis). Black dots indicate that the difference is significant at p<0.1 (determined using a two-sample t-test). (**c**), (**d**) Time-height cross section composites of cloud fraction (%) for the CTL run (dashed lines), the EXP run (solid lines), and the differences between the EXP and the CTL run (shading) for the dry season case on the left side and the wet season case on the right side. All values are averaged over all 6 days and the study domain.

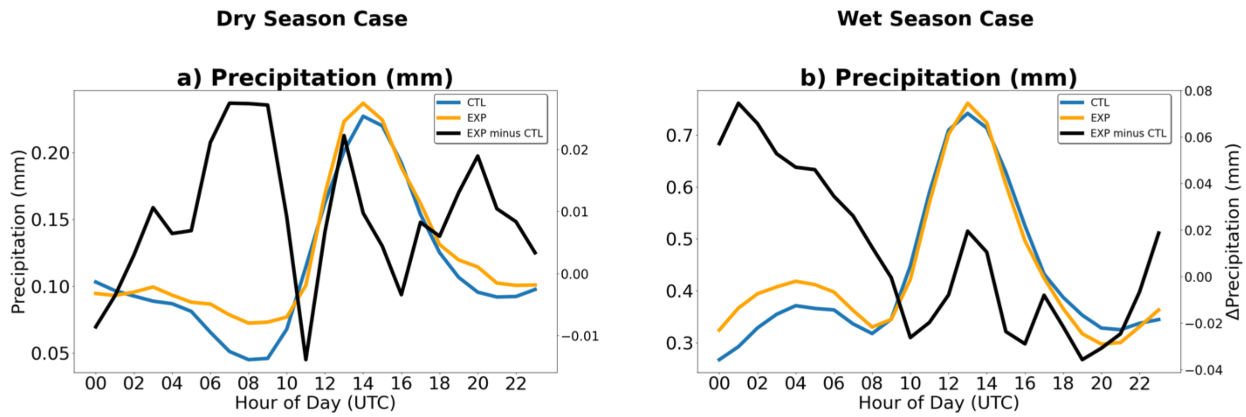

Figure 5.14: Diurnal cycles of precipitation (mm) for the dry season case (left) and the wet season case (right), for the CTL run (blue line; left y-axis), the EXP run (orange line; left y-axis), and the difference between the two (black; right y-axis). All values are averaged over all 6 days and the study domain. Black dots indicate that the difference is significant at $p<0.1$ (determined using a two-sample t-test).

5.3.4 Impacts on mesoscale circulation

Next, soil moisture induced changes in omega, divergence, and surface pressure are investigated to analyze the impacts of drier soils on air flow and circulation, which can possibly help explain some of the observed changes in cloud fractions. For the dry season case, Figs. 5.15a, c, and e indicate increased convergence below 800 hPa, increased vertical air movement between 600 hPa and 900 hPa, and increased divergence between 600 hPa and 800 hPa during the EXP run. Additionally, surface pressure is decreased. These circulation changes are likely contributing to the increase in mid-level clouds during the EXP run, where the increased vertical velocity in the lower levels can help air parcels to overcome CIN more easily. For the wet season case (Figs. 5.15b, d, and f) the circulation changes are more subtle and not statistically significant. Vertical velocity is slightly increased during the EXP run. Additionally, convergence is enhanced in the lower levels, and divergence is increased around 800 hPa and 160 hPa, while the differences in surface pressure are minimal. Consequently, circulation changes induced by the decrease in soil moisture may help to explain changes in cloud patterns during the dry season, where areas of increased vertical velocity and divergence coincide with areas of increased cloud fractions. For the wet season case, the relationship between changes in clouds and related dynamic effects may be much weaker.

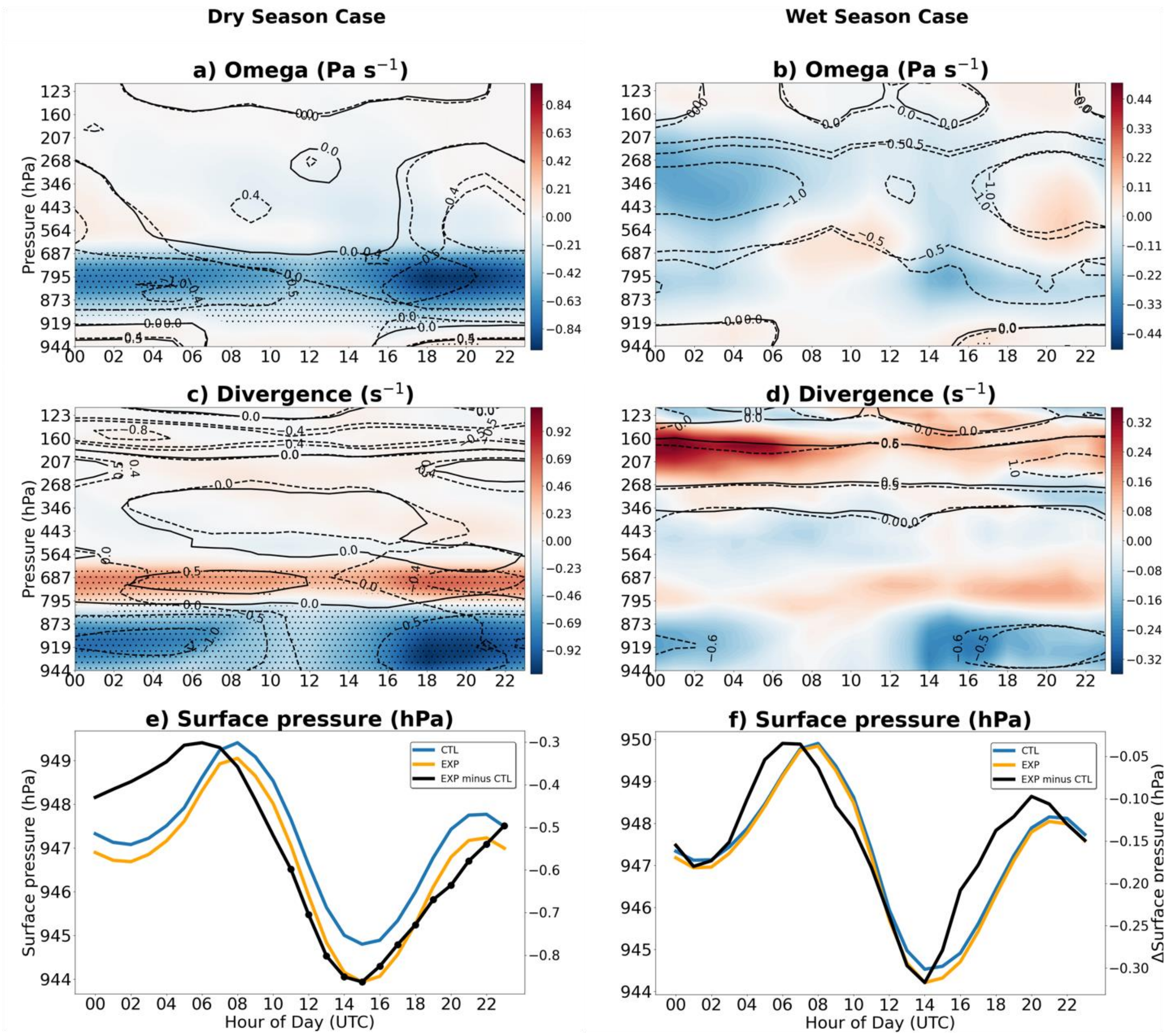

Figure 5.15: (**a-d**)Time-height cross section composites of (**a**), (**b**) omega ($10^{-1} \times$ Pa s^{-1}), and (**c**), (**d**) divergence ($10^{-5} \times$ s^{-1}) values for the CTL run (dashed lines), the EXP run (solid lines), and the differences between the EXP and the CTL run (shading) for the dry season case on the left side and the wet season case on the right side. Stippling indicates that the difference is significant at p<0.1 (determined using a two-sample t-test). **(e)**, **(f)** Diurnal cycles of surface pressure (hPa). Black dots indicate that the difference is significant at p<0.1 (determined using a two-sample t-test). All values are averaged over all 6 days and the study domain.

5.4 Discussion and Conclusions

The Congo has been experiencing a long-term and large-scale drying trend accompanied by a decrease in precipitation since around 1980 (Zhou et al. 2014; Hua et al. 2016; Hua et al. 2018; Jiang et al. 2019). Simultaneously, an increase in convective activity has been observed over the region (Raghavendra et al. 2018; Taylor et al. 2018, Alber et al. 2021a; Alber et al. 2021b). To explore possible connections between the observed drying trend and changes in convection over the Congo rainforest, this study investigates the impacts of a decrease in soil moisture on atmospheric stability and convection by using the WRF model. Two 6-day case studies are analyzed (i.e., one wet season case and one dry season case), where the soil moisture was decreased by 50% and the effects on several different variables such as heat fluxes, temperature and humidity profiles, LCL, PBL, CAPE/CIN, the GDI, and cloud fraction are quantified. Additionally, circulation changes induced by drier soils are investigated through an analysis of changes in omega, divergence, and surface pressure.

Results indicate an increase in total cloud fraction when decreasing soil moisture. More specifically, mid- and high-level clouds (i.e., convective clouds) show an increase consistent with previous studies (Raghavendra et al. 2018; Taylor et al. 2018, Alber et al. 2021a; Alber et al. 2021b), whereas low-level clouds are decreased. Interestingly, the GDI and CAPE are decreased while CIN is increased, indicating a decrease in convective potential associated with drier soils. An analysis of the sub-indices of the GDI suggests that the decrease in convective potential is mainly attributable to reduced moisture availability in the lower and mid layers. However, some drying induced changes (i.e., increasing temperature difference between mid and low layers, and a decreasing θe gradient with height) are enhancing convective potential and are possibly contributing to the observed increase in mid-level clouds. Overall, the decrease in CAPE and GDI can primarily be attributed to a decrease in moisture in the mid- and lower layers, which has a more pronounced effect compared to temperature changes. Simultaneously, although less pronounced, temperature changes are resulting in decreased atmospheric stability which will in turn act to enhance thunderstorm activity.

Figure 5.16 summarizes the soil moisture induced changes in low-, mid-, and high-level clouds as well as the processes associated with the observed changes. A decrease in soil moisture will decrease the latent heat flux and increase the sensible heat flux, which enhances the warming and drying of near surface atmospheric layers. These changes may increase the LCL and lead to the simulated decrease in low-level clouds. Additionally, the reduced moisture availability decreases the overall GDI and CAPE, which may also help to decrease clouds below 700 hPa. Contrastingly, the warmer and drier surface conditions will increase the PBL height and result in parcels reaching saturation at higher levels, subsequently increasing the LCL height, which likely contributes to the observed increase in mid-level clouds. A warmer and drier surface layer also increases the ability of air parcels to overcome CIN, which enhances convection (Findell and Ethair 2003; Hohenegger et al. 2009; Liu et al. 2022). Additionally, the warming of the lower layers increases the temperature differences between low and mid-level layers, which destabilizes the atmosphere, increases the GDI, and ultimately increases convective activity. These factors likely collectively act to enhance mid- and high-level clouds. Taking dynamic soil moisture responses into account as well, results indicate altered circulation patterns with decreasing soil moisture. Observed changes include increased near surface convergence and vertical motion, which possibly helps to enhance mid- and high-level clouds. In summary, although the overall GDI and CAPE are decreased due to the limited latent heat flux with reduced soil moisture, the sensible heat flux is increased. This will result in more heat being produced and thus increased surface temperatures, PBL height, and vertical velocity. These changes likely enhance the ability of air parcels to overcome CIN and may destabilize the column by increasing the temperature differences between low and mid-level layers, possibly contributing to the simulated increase in clouds with reduced soil moisture.

Although several studies have documented a drying trend and an increase of thunderstorms and convection over the Congo in recent years, the presented WRF results indicate an overall decrease of convective potential associated (i.e., decreased CAPE and overall GDI) with a decrease in soil moisture. This discrepancy with other studies may be explained by several factors.

Firstly, previous studies have shown that CAPE is not necessarily a good indicator for convection in the tropics. For example, Schiro et al. (2020) argue that while CAPE estimates the maximum potential of convective systems, high CAPE does not necessarily mean that the indicated high potential will always lead to the strongest convective storms or high precipitation amounts. Furthermore, studies such as Chen et al. (2020), Yin et al. (2015), Adams and Souza (2009), or DeMott and Randall (2004) indicate that trends in CAPE are primarily driven by changes in low-level moisture. Thus, a decrease in soil moisture as simulated in the presented study, and hence a decrease in low-level moisture, will likely lead to a decrease in CAPE, which is consistent with our results. However, increased surface heating and drying will also impact convective activity and act to increase convection. This is reconciled by an analysis of the sub-indices of the GDI, suggesting that an increase in the temperature difference between low- and mid-levels enhances convection, which is possibly linked to the increase in mid- and high-level clouds. This is consistent with the observed increase in convective activity found in other studies and can be associated with the increased surface heating and the subsequent increase in LCL and PBL heights as well as circulation changes with drier soils.

Secondly, here, the results of a controlled modeling study are presented, where only one variable was altered. Other factors that have possibly been influencing trends in convective activity over recent years such as changes in forest greenness and leaf area index, wave activity, climate variability, or other circulation changes were not taken into account. However, these factors may have been contributing to the increase in thunderstorm activity documented in other studies using reanalysis and satellite data.

An intriguing result was revealed by the time-height cross section composites of temperature and humidity (Fig. 5.6), namely a very distinct strip of decreased temperature and increased moisture around 600 hPa as a result of a reduction in soil moisture. This result is consistent with the temperature, relative humidity, and equivalent potential temperature trends presented in Alber et al. (2021a), which showed a decrease in temperature as well as an increase in relative humidity and equivalent potential temperature around 600 hPa over the Congo Basin from 1983 to 2019. One possible explanation for this observed cooling and moistening signal is the increased LCL height associated with drier soil conditions. With wetter soils (i.e., CTL run), the saturation and thus the LCL is reached earlier, and the latent heat release will offset the cooling, resulting in warmer temperatures in the CTL run compared to the EXP run. More specifically, as discussed in section 5.3.2, a parcel in the EXP run is warmer and drier at the surface. It then cools dry adiabatically while it is lifted until it reaches saturation, after which it cools moist adiabatically and thus at a slower rate. Since a parcel in the CTL run is colder and moister, it reaches saturation earlier and changes to cooling at the moist adiabatic lapse rate at lower levels, and thus cools at a slower rate when compared to the EXP run. This difference in the cooling rate could help to partially explain the colder temperatures around 600 hPa. However, one caveat of this explanation is that it focuses on the temperature and moisture of the parcel and not the environment. Since the base of the cooling strip is collocated with the base of the area of increased clouds, cloud radiative feedbacks could also play a role.

Looking at the changes in clouds and convection from a diurnal standpoint, the largest and most significant changes in temperature, humidity, LCL, and CAPE are observed in the early afternoon, while the GDI and cloud fractions showed the largest changes in the late afternoon and evening. Additionally, some variables such as CAPE and the GDI, indicated a small shift of maximum values to earlier in the day, suggesting that the peak in convection is shifting to earlier in the day as a result of drier soil conditions, which is consistent with changes observed in Alber et al. (2021b).

When comparing the wet season case to the dry season case, it becomes evident that the effects of drier soils are more pronounced and substantial during the dry season. The enhanced impacts during the dry season may be linked to the reduced water availability during this period, where the limited moisture availability likely amplifies the effects of soil moisture changes.

Overall, the results presented in this study enhance our understanding of the present and future climate over the Congo by learning how drying soils will impact convection, clouds, and atmospheric stability. This is crucial when trying to understand trends in rainfall and convection over the region and how these trends are connected to the long-term and large-scale drying trend that has been stressing the Congo Basin since the 1980's.

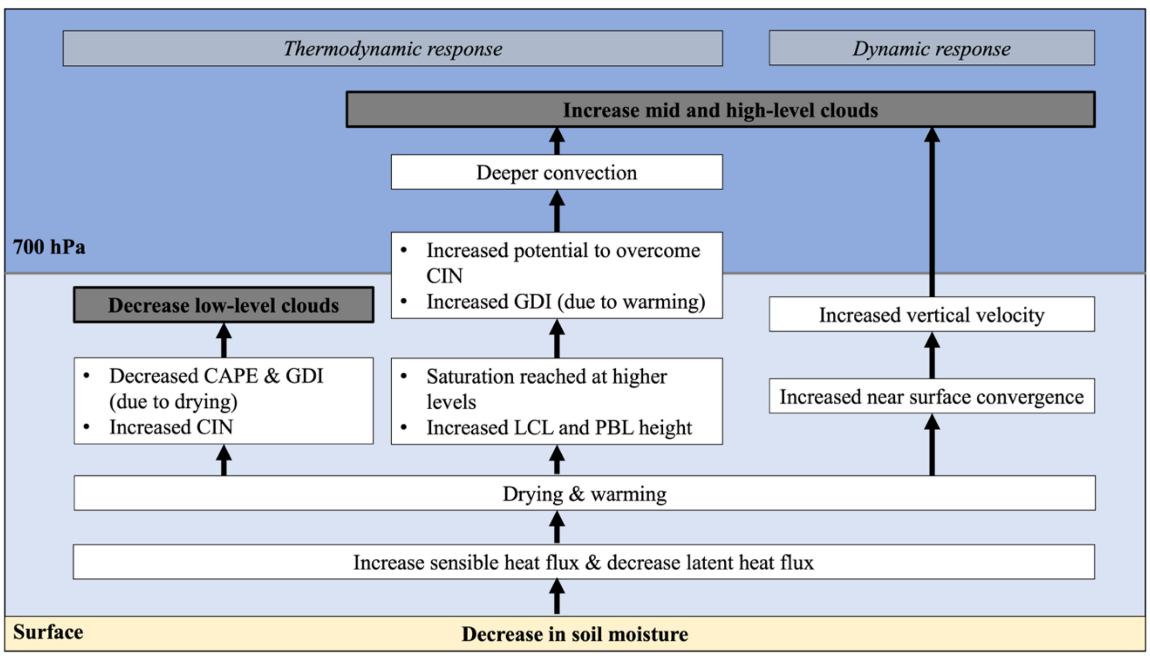

Figure 5.16: Schematic summarizing the impacts of a decrease in soil moisture on clouds and convection over the Congo Basin, identified by conducting two different WRF modeling experiments.

CHAPTER 6:
Summary, Conclusions, and Future Work

In this dissertation, I have conducted a comprehensive analysis of trends and variations in convection over the Congo Basin in central equatorial Africa. Based on four different research questions posed in Chapter 1.3, I first identified trends in thunderstorm activity over the region since 1983. I then explored changes in the diurnal cycle of convection and possible connections to the observed long-term drying trend detected over the Congo. In a next step, I looked into how the MJO impacts the diurnal cycles of convection and rainfall. A WRF study investigating how a decrease in soil moisture impacts atmospheric stability and convection over the study region concludes this dissertation. The presented results enhance our understanding of trends and variations in convection and how the observed changes might be connected to the long-term and large-scale drying trend that the Congo has been experiencing since the 1980s. This will help us to better apprehend past and future climatic changes over central equatorial Africa. Furthermore, this work contributes to the limited research and literature conducted on the Congo, which remains understudied compared to other major rainforests. This may be partly due to the very limited surface observations available over the region. This limitation was overcome in this dissertation by utilizing a range of different datasets (i.e., reanalysis and satellite data) and conducting numerical modeling studies. Below, the key results of each chapter are summarized and some avenues for future work are explored.

6.1 Summary and Conclusions

In Chapter 2, I used the GDI and GridSat-B1 satellite cold cloud fraction to analyze trends in thunderstorm activity over the Congo rainforest from 1983 to 2018 during all four seasons (i.e., DJF, MAM, JJA, and SON). The GDI was chosen for this study because it focuses on thermodynamic rather than dynamical processes, and its different sub-indices evaluating different atmospheric processes allow a more in-depth analysis of the different factors contributing to the observed changes in thunderstorm activity. ERA-Interim specific humidity and temperature data were used for the GDI calculation. Additionally, GridSat-B1 cloud fraction with T_b between -50°C and -70°C was used to quantify intense thunderstorms in addition to using the GDI to achieve a more comprehensive analysis by utilizing both reanalysis and satellite data. The analysis of both the GDI and the cloud fraction indicated an increasing trend in thunderstorm activity during all four seasons over the region. Evaluating the trends of the different sub-indices of the GDI attributed the increase in convective activity to the three following processes decreasing the hydrostatic stability: 1) a cooling of the 500 hPa temperature, 2) an increase of the temperature gradient between 700 hPa and 950 hPa, and 3) a decrease of the θ_e gradient with height. The cooling of the 500 hPa temperature was hypothesized to be connected to the more frequent occurrence of Kelvin waves over the region detected by Raghavendra et al. (2019). Furthermore, the observed warming of the lower levels and the cooling of the mid-levels was shown to be responsible for the increase in the temperature difference between 700 hPa and 950 hPa. Lastly, the decrease of the θ_e gradient with height was demonstrated to be associated with a decrease of θ_e in the lower troposphere and an increase of θ_e in the mid/upper troposphere. This change is resulting mostly from a change in moisture (i.e., a decrease in moisture in the lower troposphere and an increase in the mid/upper troposphere) rather than a change in temperature. Overall, the presented results highlight the cooling and moistening of the mid-troposphere, and drying and warming of the near surface levels, resulting in a decrease in vertical stability and convective inhibition and thus an increase in convective activity. Together, these factors may act to reinforce the drying trend which has stressed the Congo rainforest over the past 40-years.

To expand on the analysis of Chapter 2, Chapter 3 investigated changes in convective activity over the Congo Basin from a diurnal perspective. More specifically, this chapter analyzed changes in the diurnal variations of cloudiness and deep convection from 1979 to 2019 during all four seasons over the region, evaluated their associations with trends in precipitation efficiency, and explored possible connections to the observed decrease in precipitation. In addition to using the GDI and GridSat-B1 cold cloud fraction (CCF), MODIS satellite land surface temperature, CPC precipitation, and ERA5 reanalysis data were included in this study for a more comprehensive analysis. Results showed contrasting trends in clouds and T_b during the morning versus the afternoon. In the morning, a decrease in clouds and an increase in T_b was observed, while convective activity was shown to be increasing in the afternoon, which is resulting in an amplification of the diurnal T_b amplitude. These changes can possibly be connected to the observed warming and drying trend over the region, where the enhanced surface warming and drying may be contributing to the detected decrease in clouds in the morning. Additionally, the surface warimg possibly increases thunderstorm activity in the afternoon by decreasing the equivalent potential temperature gradient with height, decreasing convective inhibition, and ultimately leading to increased convective activity in the afternoon. Furthermore, precipitation efficiency was shown to be decreasing while the cloud base height is increasing. Such changes may also be partly attributable to the Congo drought, since increased surface temperatures and decreased surface relative humidity will raise the lifted condensation level, increase the cloud base height, and possibly decrease the precipitation efficiency. This positive-feedback mechanism may be a contributing factor to the observed decrease in precipitation at the surface, which will further accelerate the drying trend over the Congo. Possible connections between the drying trend and convective activity over the region are further explored in the WRF modeling study presented in Chapter 4.

Before diving deeper into investigating the impacts of the warming and drying conditions on convection over the region, I first focused on the variability of convection and precipitation induced by the MJO in Chapter 3. The MJO is the leading mode of intraseasonal variability in the tropics and can significantly impact precipitation and convection over tropical land areas. Thus, this study analyzed the influence of the MJO on diurnal variations of convection and precipitation over the Congo from 1985 to 2019 during October through March. Additionally, possible mechanisms leading to the observed changes were explored, aiming to enhance our understanding of the MJO's impacts on precipitation and convection variability, ultimately contributing to improving predictions of MJO modulated rainfall over the Congo. An analysis of GridSat-B1 and TRMM satellite as well as ERA5 reanalysis data showed that convection and precipitation are increased during the MJO enhanced convective phase (RMM phases 1 and 2) and decreased during the MJO suppressed convective phase (RMM phases 5 and 6). Exploring changes of the diurnal cycles of convection and precipitation revealed that the differences between the two phases are largest during the morning hours when convection is weakest. Additionally, the influence of the MJO was found to be stronger on stratiform precipitation while the impact on convective precipitation is negligible. More specifically, the diurnal cycles of convective precipitation are similar during both MJO phases, while the stratiform precipitation is significantly higher during the MJO enhanced phase, mainly in the morning hours. Overall, convection was found to be shallower during the MJO suppressed phase and deeper during the MJO enhanced phase, where the decay of convective clouds and anvils is also slower during the enhanced phase. To investigate possible physical mechanisms responsible for the MJO induced modulations of convection and precipitation, changes in divergence, vertical velocity, wind speed, relative humidity, and temperature were analyzed. Enhanced upward air motion in the mid- and upper levels as well as strong divergence in the upper levels were identified to be contributing to the increase in precipitation and convection during the MJO enhanced phase. During the MJO suppressed phase, strong mid-level divergence and upper- to mid-level subsidence, mainly during the nighttime and morning hours, were the main factors identified to contribute to the observed changes in convection and rainfall. Additionally, a decrease in mid-level wind speed and an increase in upper-level wind speed, together with increased relative humidity were found to be contributing to the increased formation of (stratiform) precipitation during the enhanced phase.

To further explore the impacts of a decrease in soil moisture on atmospheric stability, convection, and clouds, I performed and analyzed numerical experiments using the WRF model in Chapter 5. The model was run at a 4 km convection permitting resolution and initialized with hourly ERA5 reanalysis data. Two 6-day case studies were performed. For comparison between the wet and the dry season, one case study was selected during the dry season (16-January to 21-January 2018) while the other case study was selected during the wet season (21-October to 26-October 2019). Soil moisture was decreased by 50% for the EXP run to simulate the impacts of the drying trend on convection since studies such as Taylor et al. (2015) have shown that land surface properties and changes such as soil moisture can influence the development of convection through modulation of solar heating at the surface and thereby influencing atmospheric temperature and humidity profiles. A decrease of soil moisture by 25% showed similar but less pronounced results (not shown). As expected, the latent heat flux is limited as a result of a reduction in soil moisture, while the sensible heat flux is increased. These changes were associated with increased surface and near surface temperatures and decreased near surface humidity. Results further showed decreased convective potential (i.e., CAPE and GDI) as a result of drier soils, where the observed decrease in convective potential was attributed to a decrease in moisture availability, mainly in the lower and mid layers. Although results indicated an overall decrease in convective potential, two processes induced by a decrease in soil moisture, identified using the GDI and its sub-indices, were discovered to be contributing to increased convective activity. These processes include the increasing temperature difference between the mid- and low layers, and a decreased θ_e gradient with height. An analysis of the impacts of drier soils on cloud fractions showed a decrease in clouds in the lower levels (below 700 hPa), an increase in clouds in the mid-levels (700 hPa to 550 hPa), and a slight but mostly insignificant increase in clouds in the upper atmospheric levels (above 550 hPa). The decrease in cloud in the lower levels was mostly attributed to the decreased moisture availability in the near surface levels associated with a reduction in soil moisture. The increase in clouds in the mid (and upper) levels was hypothesized to be the effect of increased surface heating, leading to an increase in PBL and LCL height, a decrease in atmospheric stability, and circulation changes such as increased near surface convergence and vertical motion. These factors may collectively act to increase clouds in the mid-levels. Overall, this chapter analyzes the complex interactions between changes in soil moisture and atmospheric stability and convection over the Congo rainforest, where a decrease in soil moisture was found to significantly impact convective potential, especially during the dry season, while also modulating clouds depending on the respective atmospheric level.

6.2 Future Work

This dissertation points to more questions and future research ideas that will help to further enhance our understanding of observed trends and variations in convection, rainfall, and other variables over the Congo.

In this dissertation, it was determined that thunderstorm activity over the Congo has been increasing by using several methods and datasets. Simultaneously, precipitation has been decreasing over the region. Although some potential mechanisms explaining this counterintuitive relationship have been explored in this dissertation, a more detailed analysis determining specific physical mechanisms should be conducted in order to completely solve this puzzle. Studies such as Schiro et al. (2020) suggest that precipitation intensity does not necessarily correlate strongly with environmental instability, while other studies such as Hamada et al. (2015) or Zipser et al. (2006) conclude that the heaviest precipitation does not always occur in the most unstable environments with strong updrafts. Accordingly, the relationship between convection and precipitation over the Congo should be further examined.

A cooling and moistening trend in the mid-atmospheric levels around 500 hPa was identified in this dissertation both by conducting a trend analysis of reanalysis data from 1983 to 2018 as well as by running numerical modeling experiments investigating impacts of a reduction in soil moisture on atmospheric stability profiles. Some possible explanations for this phenomenon were described. However, the underlying mechanisms should be examined more extensively. For example, the connection of the cooling to cloud radiative feedbacks should be investigated further. This could be done by running more extensive numerical modeling experiments.

In this dissertation, the effects of the drying trend on atmospheric stability were investigated by decreasing the soil moisture by 50%. However, other variables are also affected by the drying trend. The WRF modeling work should be expanded to include these factors such as changes in the LAI.

A significant increase in MJO dry days was discovered in this dissertation, which could be a contributing factor to the drying trend over the region. It would be of interest to find the factors responsible for this increase since the decrease in MJO dry days could be a remote factor contributing to the drying trend over the Congo.

References

Achugbu, I.C., Dudhia, J., Olufayo, A.A., Balogun, I.A., Adefisan, E.A., Gbode, I.E., 2020. Assessment of WRF land surface model performance over West Africa. Advances in Meteorology, 2020, 1687–9309.

Adams, D. K., and Souza, E. P., 2009. CAPE and convective events in the Southwest during the North American monsoon. Mon. Wea. Rev. 137, 83–98.

Adler, R.F., Gu, G., Sapiano, M., Wang, J.J., Huffman, G.J., 2017. Global precipitation: means, variations and trends during the satellite era (1979–2014). Surv. Geophys. 38, 679–699.

Alaka, G.J., Maloney, E.D., 2012. The influence of the MJO on upstream precursors to African easterly waves. J. Clim. 25(9), 3219-3236.

Alber, K., Raghavendra, A., Zhou, L., Jiang, Y., Sussman, H.S., Solimine, S.L., 2021a. Analyzing intensifying thunderstorms over the Congo Basin using the Gálvez- Davison index from 1983–2018. Clim. Dyn. 56, 949–967.

Alber, K., Zhou, L., Raghavendra, A., 2021b. A shift in the diurnal timing and intensity of deep convection over the Congo Basin during the past 40 years. Atmos. Res. 264, 0169-8095.

Alduchov, O.A., Eskridge, R.E., 1996. Improved magnus form approximation of saturation vapor pressure. J. Appl. Meteorol. 35, 601–609.

Alsdorf D et al., 2016. Opportunities for hydrologic research in the Congo Basin. Rev. Geophys. 54, 378–409.

Anber, U., Wang, S., Sobel, A.H., 2014. Response of atmospheric convection to vertical wind shear: Cloud-system resolving simulations with parameterized large-scale circulation. Part I: Specified radiative cooling. J. Atmos Sci. 71, 2976–2993.

Angelis, C. F., McGregor, G. R., Kidd, C., 2004. Diurnal cycle of rainfall over the Brazilian Amazon. Climate Res. 26(2), 139–149.

Awaka, J., Iguchi, T., Kumagai, H., Okamoto, K., 1997. Rain type classification algorithm for TRMM precipitation radar. JOURNAL OF APPLIED METEOROLOGY VOLUME 42 IEEE 1997 Int. Geoscience and Remote Sensing Symp., Singapore, Japan, Institute of Electrical and Electronics Engineers. 1633–1635.

Berhane, F., Zaitchik, B., 2014. Modulation of daily precipitation over East Africa by the Madden–Julian Oscillation. J. Clim. 27, 6016–6034.

Betts, A. K., J. H. Ball, 1998. FIFE surface climate and site-average dataset 1987–89. J. Atmos. Sci. 55, 1091–1108.

Betts, A.K., Dugan, F.J., 1973. Empirical formula for saturation psuedoadiabats and saturation equivalent potential temperature. J. Appl. Meteor. 12, 731–732.

Bolton, D., 1980. The computation of equivalent potential temperature. Mon. Wea. Rev. 108, 1046–1053.

Brncic, T.M., Willis, K.J., Harris, D.J., Washington, R., 2007. Culture or climate? The relative influences of past processes on the composition of the lowland Congo rainforest. Phil. Trans. R. Soc. B. 362, 229-242.

Brock, F.V., Richardson, S.J, 2001. Meteorological Measurement Systems. Oxford University Press 290pp.

Buizza, R., Houtekamer, P.L., Toth, Z., Pellerin, G., Wei, M., Zhu, Y., 2005. A comparison of the ECMWF, MSC, and NCEP global ensemble prediction systems. Mon. Wea. Rev. 133, 1076–1097.

Bush, E.R., Jeffery, K., Bunnefeld, N., Tutin, C., Musgrave, R., Moussavou, G., Mihindou, V., Malhi, Y., Lehmann, D., Edzang, Ndong, J., Makaga, L., Abernethy, K., 2020. Rare ground data confirm significant warming and drying in western equatorial Africa. Peer J. 8, e8732.

Byrne, M.P., Schneider, T., 2016. Narrowing of the ITCZ in a warming climate: Physical mechanisms. Geophys. Res. Lett. 43, 11350–11357.

Chakraborty, S., Jiang, J.H., Su, H., and Fu, R., 2019. Deep convective evolution from shallow clouds over the Amazon and Congo rainforests. J. Geophys. Res. Atmos. 125, e2019JD030962.

Chen, J., Dai, A., Zhang, Y., Rasmussen, K. L., 2020. Changes in convective available potential energy and convective inhibition under global warming. J. Clim. 33, 2025–2050.

Chen, F., Dudhia, J., 2001. Coupling an advanced land surface–hydrology model with the Penn State–NCAR MM5 modeling system. Part I: Model implementation and sensitivity. Mon. Wea. Rev. 129, 569–585.

Christian, H.J., Blakeslee, R.J., Boccipio, D.J., Boeck, W.L., Buechler, D.E., Driscoll, K.T., Goodman, S.J., Hall, J.M., Koshak, W.J., Mach, D.M., Stewart, M.F., 2003. Global frequency and distribution of lightning as observed from space by the Optical Transient Detector. J. Geophys. Res. 108, 4005.

Creese, A., Washington, R., Jones, R., 2019. Climate change in the Congo Basin: processes related to wetting in the December–February dry season. Clim. Dyn. 53, 3583–3602.

Dai, A., 2006. Precipitation characteristics in eighteen coupled climate models. J. Clim. 19, 4605–4630.

Dai, A., Giorgi, F., Trenberth, K. E., 1999. Observed and model-simulated diurnal cycles of precipitation over the contiguous united states, J. Geophys. Res. 104(D6), 6377–6402.

Dai, A., 2001a. Global precipitation and thunderstorm frequencies. Part I: Seasonal and interannual variations. J. Climate. 14, 1092-1111.

Dai, A., 2001b. Global precipitation and thunderstorm frequencies. Part II: diurnal variations. J.

Climate. 14, 1112-1128.

Dai, A., Xin, L., Hsu, K.-L., 2007. The frequency, intensity, and diurnal cycle of precipitation in surface and satellite observations over low- and mid-latitudes. Clim. Dyn. 29, 727-744.

Dee, D.P., Uppala, S.M., Simmons, A.J., et al., 2011. The ERA-Interim reanalysis: configuration and performance of the data assimilation system. Q. J. R. Meteorol. Soc. 137, 553–597.

DeMott, C. A., Randall, D. A., 2004. Observed variations of tropical convective available potential energy. J. Geophys. Res. 109, D02102.

Déqué, M., Rowell, D.P., Lüthi, D., et al., 2007. An intercomparison of regional climate simulations for Europe: assessing uncertainties in model projections. Clim. Change, 81l, 53–70.

Dias, J., Sakaeda, N., Kiladis, G.N., Kikuchi, K., 2017. Influences of the MJO on the space-time organization of tropical convection. J. Geophys. Res. Atmos. 122, 8012-8032.

Diem, J., Ryan, S., Hartter, J., Palace, M., 2014. Satellite-based rainfall data reveal a recent drying trend in central equatorial Africa. Clim. Change. 126, 263– 272.

Dudhia, J., 1989. Numerical study of convection observed during the winter monsoon experiment using a mesoscale twodimensional model. J. Atmos. Sci. 46, 3077–3107.

Dyer, E.L.E., Jones, D.B.A., Nusbaumer, J., Li, H., Collins, O., Vettoretti, G., Noone, D., 2017.

Congo Basin precipitation: assessing seasonality, regional interactions, and sources of moisture. J. Geophys. Res. Atmos. 122, 6882–6898.

Ek, M. B., Mitchell, K. E., Lin, Y., Rogers, E., Grunmann, P., Koren, V., Gayno, G., Tarpley, J. D., 2003. Implementation of Noah land surface model advances in the National Centers for Environmental Prediction operational mesoscale Eta model. J. Geophys. Res. 108, 8851.

Engelbrecht, F., et al., 2015. Projections of rapidly rising surface temperatures over Africa under low mitigation. Environ. Res. Lett. 10, 85004.

Evans, J.P., Westra, S., 2012. Investigating the mechanisms of diurnal rainfall variability using a regional climate model. J. Clim. 25, 7232–7247.

Feng, S., Fu, Q., 2013. Expansion of global drylands under a warming climate. Atmos. Chem. Phys. 13(19), 10081–10094.

Feng, Z., Leung, L.R., Liu, N., Wang, J., Houze Jr, R.A., Li, J., Hardin, J.C., Chen, D. Guo, J., 2021. A global high-resolution mesoscale convective system database using satellite-derived cloud tops, surface precipitation, and tracking. J. Geophys. Res. 126(8), e2020JD034202.

Findell, K.L. Eltahir, E.A.B., 2003. Atmospheric controls on soil moisture–boundary layer interactions. Part II: Feedbacks within the continental United States. J. Hydrometeorol. 4, 570–583.

Fotso-Nguemo, T.C., Chamani, R., Yepdo, Z.D., Sonkoué, D., Matsaguim, C.N., Vondou, D.A., Tanessong, R.S., 2018. Projected trends of extreme rainfall events from CMIP5 models over central Africa. Atmo. Sci. Lett. 19, 1–8.

Frigo, M., Johnson, S.G., 1998. FFTW: an adaptive software architecture for the FFT. Proc. IEEE Int. Conf. Acoust. Speech Signal Process. Seattle, WA 3, 1381–1384.

Frigo, M., Johnson, S.G., 2005. The design and implementation of FFTW3. Proc. IEEE 93, 216–231.

Fu, R., 2015. Global warming-accelerated drying in the tropics. Proc. Natl. Acad. Sci. USA. 112, 3593–3594.

Fu, R., Zhu, B., Dickinson, R.E., 1999. How do atmosphere and land surface influence seasonal changes of convection in the tropical Amazon? J. Clim. 12(5), 1306–1321.

Gálvez, J.M., Davison, M., 2016. The Gálvez-Davison Index for Tropical Convection. http://www.wpc.ncep.noaa.gov/international/gdi/GDI_Manuscript_V20161021.pdf Accessed 24 Apr 2020.

Garreaud, R.D., Wallace, J.M., 1997. The diurnal march of convective cloudiness over the Americas. Mon. Weather Rev. 125, 3157–3171.

Gleixner, S., Demissie, T., Diro, G.T., 2020. Did ERA5 improve temperature and precipitation reanalysis over East Africa? Atmosphere 2020 (11), 996.

Gottschalck, J., Wheeler, M., Weickmann, K., Vitart, F., Savage, N., et al., 2010. A framework for assessing operational Madden–Julian oscillation forecasts: a CLIVAR MJO working group project. Bull. Am. Meteorol. Soc. 91, 1247-1258.

Guan, K., Pan, M., Li, H. et al., 2015. Photosynthetic seasonality of global tropical forests constrained by hydroclimate. Nature Geosci. 8, 284–289.

Guillod, B.P., Orlowsky, B., Miralles, D.G., Teuling, A.J., Seneviratne, S.I., 2015. Reconciling spatial and temporal soil moisture effects on afternoon rainfall. Nat. Commun. 6, 6443.

Guo, Z., Dirmeyer, P. A., DelSole, T., 2011. Land surface impacts on subseasonal and seasonal predictability, Geophys. Res. Lett. 38, L24812.

Guo, Z., et al., 2006. GLACE: The Global Land–Atmosphere Coupling Experiment. Part II: Analysis. J. Hydrometeor. 7, 611–625.

Haensler, A., Saeed, F., Jacob, D., 2013. Assessment of projected climate change signals over central Africa based on a multitude of global and regional climate projections. In: Climate Change Scenarios for the Congo Basin. [Haensler A, Jacob D, Kabat P, Ludwig F (eds.)]. Climate Service Centre Report No. 11, Hamburg, Germany, ISSN: 2192-4058.

Haklander, A., van Delden, A.J., 2003. Thunderstorm predictors and their forecast skill for the Netherlands. Atmos. Res. 67–68, 273-299.

Hamada, A., Takayabu, Y.N., Liu, C., Zipser, E.J., 2015. Weak linkage between the heaviest rainfall and tallest storms. Nat. Commun. 6, 6213.

Hart, N.C., Reason, C.J., Fauchereau, N., 2013. Cloud bands over southern Africa: Seasonality, contribution to rainfall variability and modulation by the MJO. Clim. Dyn. 41, 1199-1212.

Hart, N.C.G., Washington, R., Maidment, R.I., 2019. Deep Convection over Africa: Annual Cycle, ENSO, and Trends in the Hotspots. Bull. Am. Meteorol. Soc. 32, 8791-8811.

Hartman, A.T., 2021. Tracking mesoscale convective systems in central equatorial Africa. Int. J. Climatol. 41(1), 469– 482.

Hassim, M.E., Lane, T.P., Grabowski, W.W., 2016. The diurnal cycle of rainfall over New Guinea in convection-permitting WRF simulations. Atmos. Chem. Phys. 16, 161–175

Hawinkel, P., Thiery, W., Lhermitte, S., Swinnen, E., Verbist, B., Van Orshoven, J., Muys, B., 2016. Vegetation response to precipitation variability in East Africa controlled by biogeographical factors. J. Geophys. Res. 121, 2422–44.

Heath, N. K., Fuelberg, H. E., 2014. Using a WRF simulation to examine regions where convection impacts the Asian summer monsoon anticyclone. Atmos. Chem. Phys. 14, 2055–2070.

Hendon, H. H., Woodberry, K., 1993. The diurnal cycle of tropical convection. J. Geophys. Res. 98, 16 523–16 637.

Hersbach, H., et al., 2020. The ERA5 global reanalysis. Q. J. R. Meteorol. Soc. 2020, 1–51.

Hohenegger, C., Brockhaus, P., Bretherton, C., Schär, C., 2009. The soil moisture–precipitation feedback in simulations with explicit and parameterized convection. J. Clim. 22 (19), 5003-5020.

Hong, S.-Y., Noh, Y. Dudhia, J., 2006. A new vertical diffusion package with an explicit treatment of entrainment processes. Mon. Wea. Rev. 134, 2318–2341.

Hong, G., Heygster, G., Miao, J. G., Kunzi, K., 2005. Detection of tropical deep convective clouds from AMSU-B water vapor channels measurements. J. Geophys. Res.: Atmos. 110(D5), D05205.

Houze Jr., R. A., 1997. Stratiform precipitation in regions of convection: A meteorological paradox? Bull. Amer. Meteor. Soc. 78, 2179–2196.

Hua, W., Zhou, L., Chen, H., Nicholson, S.E., Jiang, Y., Raghavendra, A., 2016. Possible causes of the central equatorial African long-term drought. Environ. Res. Lett. 11, 124002.

Hua, W., Zhou, L., Chen, H., Nicholson, S.E., Jiang, Y., Raghavendra, A., 2018. Understanding the central equatorial African long-term drought using AMIP-type simulations. Clim. Dyn. 50, 1115–1128.

Hua, W., Zhou, L., Nicholson, S.E., Chen, H., Qin, M., 2019. Assessing reanalysis data for understanding rainfall climatology and variability over Central Equatorial Africa. Clim. Dyn. 53, 651–669.

Huffman, G.J., Bolvin, D.T., Nelkin, E.J., Wolff, D.B., Adler, R.F., Gu, G., Hong, Y., Bowman, K.P., Stocker, E.F., 2007. The TRMM multisatellite precipitation analysis (TMPA): quasi-global, multiyear, combined-sensor precipitation estimates at fine scales. J. Hydrometeorol. 8 38–55.

Jackson, B., Nicholson, S.E., Klotter, D., 2009. Mesoscale convective systems over western equatorial Africa and their relationship to large-scale circulation. Mon. Wea. Rev. 137, 1272–1294.

Jacob, D., Petersen, J., Eggert, B., et al., 2014. EURO-CORDEX: new high-resolution climate change projections for European impact research. Reg. Environ. Change. 14, 563–578.

James, R.P., Markowski, P.M., 2010. A numerical investigation of the effects of dry air aloft on deep convection. Mon. Wea. Rev. 138, 140–161.

James, R., Washington, R., 2013. Changes in African temperature and precipitation associated with degrees of global warming. Clim. Chang. 117, 859–872.

Jayakrishnan, P.R., Babu, C.A., 2014. Assessment of convective activity using stability indices as inferred from radiosonde and MODIS data. Atmos. Clim. Sci. 4, 122-130.

Jiang, Y., Zhou L., Tucker, C.J., Raghavendra, A., Hua, W., Liu, Y., Joiner, J., 2019. Widespread increase of boreal summer dry season length over the Congo rainforest. Nat. Clim. Chang. 9, 617–622.

Jiang, Y., Zhou L., Roundy, P.E., Hua, W., Raghavendra, A., 2021. Increasing Influence of Indian Ocean Dipole on Precipitation Over Central Equatorial Africa. Geophys. Res. Lett. 48, e2020GL092370.

Jiménez, P.A., Dudhia, J., González-Rouco, J. F., Navarro, J., Montávez, J. P., García-Bustamante, E., 2012. A Revised Scheme for the WRF Surface Layer Formulation. Mon. Wea. Rev. 140, 898–918.

Johnston, B. R., F. Xie, and C. Liu, 2018. The effects of deep convection on regional temperature structure in the tropical upper troposphere and lower stratosphere. J. Geophys. Res. Atmos. 123, 1585–1603.

Jucker, M., Lane, T.P., Vincent, C.L., Webster, S., Wales, S.A. Louf, V., 2020. Locally forced convection in subkilometre-scale simulations with the Unified Model and WRF. Q. J. R. Meteorolog. Soc. 146(732), 3450–3465.

Kamitewoko, E., 2021. Impact of Climate Change on Food Crop Production in Congo Brazzaville. Modern Economy. 12, 1686-1702.

Kim, H. M., Webster, P.J., Hoyos, C.D., Kang, I-S., 2008. Sensitivity of MJO simulation and predictability to sea surface temperature variability. J. Clim. 21, 5304–5317.

Knapp, K.R., 2008. Scientific data stewardship of International Satellite Cloud Climatology Project B1 global geostationary observations. J. Appl. Remote Sens. 2, 023548.

Knapp, K.R., et al., 2011. Globally gridded satellite observations for climate studies. Bull. Am Meteorol. Soc. 92, 893–907.

Knapp, K.R., 2012. Intersatellite bias of the high-resolution infrared radiation sounder water vapor channel determined using ISCCP B1 data. J. Appl. Remote Sens. 6, 063523.

Knapp, K.R., 2016. Gridded Satellite B1 FCDR - Monthly Means. https://ncics.org/ncics/pdfs/obs4MIPs/GriddedSatelliteB1FCDR-MonthlyMeans_technical-note_final.pdf Accessed 18 May 2020.

Koster, R. D., et al., 2004. Regions of strong coupling between soil moisture and precipitation. Science. 305, 1138–1140.

Lafleur, D. M., Barrett, B.S., Henderson, G.R., 2015. Some climatological aspects of the Madden–Julian oscillation (MJO). J. Clim. 28, 6039–6053.

Lau, K.M., Wu, H.T., 2003. Warm rain processes over tropical oceans and climate implications. Geophys. Res. Lett. 30, 2290.

Lazri, M., Ameur, S., Brucker, J. M., Ouallouche, F., 2014. Convective rainfall estimation from MSG/SEVIRI data based on different development phase duration of convective systems (growth phase and decay phase). Atmos. Res. 147–148 38–50.

Lee, D.E., Biasutti, M., 2014. Climatology and variability of precipitation in the Twentieth

Century Reanalysis. J. Clim. 27, 5964–5981.

Lewis, S. L., 2006. Tropical forests and the changing earth system. Phil. Trans. R. Soc. Lond. B. 361, 195–210.

Lewis, S., Lopez-Gonzalez, G., Sonké, B. et al., 2009. Increasing carbon storage in intact African tropical forests. Nature. 457, 1003–1006.

Lin, J., B. E. Mapes, M. Zhang, M. Newman, 2004. Stratiform precipitation, vertical heating profiles, and the Madden-Julian Oscillation. J. Atmos. Sci. 61, 296–309.

Liu, W., Zhang, Q., Li, C., Xu, L., Xiao, W., 2022. The influence of soil moisture on convective activity: A review. Theor. Appl. Climatol. 149(1–2), 221–232.

Liu, F., Wang, B., Ouyang, Y. et al., 2022. Intraseasonal variability of global land monsoon precipitation and its recent trend. npj Clim. Atmos. Sci. 5, 30.

Lu, J., Li, T., Wang, L., 2019. Precipitation diurnal cycle over the Maritime Continent modulated by the MJO. Clim. Dyn. 53, 6489–6501.

Lutsko, N.J., Cronin, T.W., 2018. Increase in precipitation efficiency with surface warming in radiative-convective equilibrium. J. Adv. Model. Earth Syst. 10, 2992–3010.

Madden, R.A., Julian, P.R., 1971. Detection of a 40–50 day oscillation in the zonal wind in the tropical Pacific. J. Atmos. Sci. 28, 702–708.

Madden, R. A., Julian, P. R., 1972. Description of global-scale circulation cells in the tropics with a 40–50 day period. J. Atmos. Sci. 29, 1109–1123.

Mapes, B. E., Lin, J., 2005. Doppler radar observations of mesoscale wind divergences in regions of tropical convection. Mon. Wea. Rev. 133, 1808–1824.

Mapes, B. E., Houze Jr. R. A., 1993. Cloud clusters and superclusters over the oceanic warm pool, Mon. Weather Rev. 121, 1398–1415.

Marion, G.R., Trapp, R.J., 2019. The dynamical coupling of convective updrafts, downdrafts, and cold pools in simulated supercell thunderstorms. J. Geophys. Res. Atmos. 124, 664–683.

Market, P., Allen, S., Scofield, R., Kuligowski, R., Gruber, A., 2003. Precipitation efficiency of warm-season Midwestern mesoscale convective systems. Wea. Forecasting 18, 1273–1285.

Maybee, B., Ward, N., Hirons, L. C., Marsham, J. H., 2022. Importance of Madden–Julian oscillation phase to the interannual variability of East African rainfall. Atmos. Sci. Lett. e1148.

Miller, P.W., Mote, T.L., Ramseyer, C.A., 2019. An Empirical Study of the Relationship between Seasonal Precipitation and Thermodynamic Environment in Puerto Rico. Bull. Am.. Meteorol. Soc. 34, 277-288.

Mlawer, E. J., Taubnam, S. J., Brown, P. D., Iacono, M. J., Clough, S. A., 1997. Radiative transfer for inhomogeneous atmospheres: RRTM, a validated correlated-k model for the longwave. J. Geophys. Res. 102, 16663–16682.

Munzimi, Y.A., Hansen, M.C., Adusei, B., Senay, G.B., 2015. Characterizing Congo basin rainfall and climate using Tropical Rainfall Measuring Mission (TRMM) satellite data and limited rain gauge ground observations. J. Appl. Meteor. Climatol. 54, 541–555.

Musau, J., Patil, S., Sheffield, J., Marshall, M., 2018. Vegetation dynamics and responses to climate anomalies in East Africa. Earth Syst. Dyn. Discuss. 1-27.

National Research Council (NRC 2004) Climate Data Records from Environmental Satellites. National Academies Press. 102 pp.

Negri, A.J., Bell, T.L., Xu, L., 2002. Sampling of the diurnal cycle of precipitation using TRMM. J. Atmos. Ocean. Technol. 19, 1333-1344.

Nesbitt, S. W., E. J. Zipser, 2003. The diurnal cycle of rainfall and convective intensity to three years of TRMM measurements. J. Clim. 16, 1456–1475.

Nicholson, S.E., 2018. The ITCZ and the seasonal cycle over equatorial Africa. Bull. Am. Meteorol. Soc. 30, 337–348.

Nicholson, S. E., Klotter, D., Zhou, L., Hua, W., 2019. Validation of satellite precipitation estimates over the Congo Basin. J. Hydrometeor. 20, 631–56.

Nkem, J.N., Somorin, O.A., Jum, C. et al., 2013. Profiling climate change vulnerability of forest indigenous communities in the Congo Basin. Mitig. Adapt. Strateg. Glob. Change. 18, 513–533.

Oh, J.-H., Kim, K.-Y., Lim, G.-H., 2012. Impact of MJO on the diurnal cycle of rainfall over the western Maritime Continent in the austral summer. Clim. Dyn. 38, 1167–1180.

Otto, F. E. L., Jones, R. G., Halladay, K., Allen, M. R., 2013. Attribution of changes in precipitation patterns in African rainforests. Phil. Trans. R. Soc. B. 368(1625), 20120299.

Pal, J.S., Eltahir, E.A.B., 2001. Pathways relating soil moisture conditions to future summer rainfall within a model of the land-atmosphere system. J. Clim. 14, 1227–1242.

Perez, R., Kivalov, S., Schlemmer, J., Hemker, K. Jr., Renné, D., Hoff, T.E., 2010. Validation of short and medium term operation solar radiation forecasts in the US. Sol. Energy. 84, 2161-2172.

Pohl, B., Camberlin, P., 2006. Influence of the Madden–Julian Oscillation on East African rainfall. I: intraseasonal variability and regional dependency. Q. J. R. Meteorol. Soc. 132, 2521–2539.

Pokam, W.M., Djiotang, L.A.T., Mkankam, F.K., 2012. Atmospheric water vapor transport and recycling in Equatorial Central Africa through NCEP/NCAR reanalysis data. Clim. Dyn. 38, 1715–1729.

Polcher, J., 1995. Sensitivity of tropical convection to land surface processes. J. Atmos. Sci. 52, 3143–3161.

Prein, A.F., Heymsfield, A.J, .2020. Increased melting level height impacts surface precipitation phase and intensity. Nat. Climate Change. 10, 771–776.

Prein, A.F., Langhans, W., Fosser, G., et al., 2015. A review on regional convection-permitting climate modeling: demonstrations, prospects, and challenges. Rev. Geophys. 53, 323–361.

Raghavendra, A., Xia, G., Zhou, L., Jiang, Y., 2022. Orographic Enhancement of Rainfall Over the Congo Basin. Atmos. Sci. Lett. 23, e1079.

Raghavendra, A., Zhou, L., Roundy, P.E., et al., 2020. The MJO's impact on rainfall trends over the Congo rainforest. Clim. Dyn. 54, 2683–2695.

Raghavendra, A., Roundy, P.E., Zhou, L., 2019. Trends in tropical wave activity from 1980s–2016. J. Clim. 32, 1661–1676.

Raghavendra, A., Milrad, S.M., 2019. A new metric to diagnose precipitation distribution in transitioning tropical cyclones. J. Operational Meteor. 7, 61–77.

Raghavendra, A., Zhou, L., Jiang, Y., Hua, W., 2018. Increasing extent and intensity of thunderstorms observed over the Congo Basin from 1982 to 2016. Atmos. Res. 213, 17–26.

Raghavendra, A., Zhou, L., Roundy, P.E., et al., 2020. The MJO's impact on rainfall trends over the Congo rainforest. Clim. Dyn. 54, 2683–2695.

Rasmussen, K. L., and Houze Jr., R. A., 2016. Convective initiation near the Andes in subtropical South America. Mon. Wea. Rev. 144, 2351–2374.

Rauniyar, S.P., Walsh, K.J.E., 2011. Scale interaction of the diurnal cycle of rainfall over the Maritime Continent and Australia: Influence of the MJO. J. Clim. 24, 325–348.

Rauniyar, S. P., and Walsh, K. J. E., 2013. Influence of ENSO on the diurnal cycle of rainfall over the Maritime Continent and Australia. J. Clim. 26, 1304–1321.

Robe, F.R., Emanuel, K.A., 2001. The effect of vertical wind shear on radiative–convective equilibrium states. J. Atmos. Sci. 58, 1427–1445.

Rooney, G. G., N. P. M. Van Lipzig, W. Thiery, 2018. Estimating the effect of rainfall on the surface temperature of a tropical lake. Hydrol. Earth Syst. Sci. 22, 6357–6369.

Sakaeda, N., Kiladis, G., Dias, J., 2017. The diurnal cycle of tropical cloudiness and rainfall associated with the Madden–Julian oscillation. J. Clim. 30, 3999–4020.

Sandjon, A. T., Nzeukou, A., Tchawoua, C., 2012. Intraseasonal atmospheric variability and its interannual modulation in central Africa. Meteorog. Atmos. Phys. 117(3–4), 167–179.

Saxen, T.R., Rutledge, S.A., 2000. Surface rainfall–cold cloud fractional coverage relationship in TOGA COARE: A function of vertical wind shear. Mon. Wea. Rev. 128, 407-415.

Scaff, L., Prein, A., Li, Y., Liu, C., Rasmussen, R., Ikeda, K., 2020. Simulating the convective precipitation diurnal cycle in North America's current and future climate. Clim. Dyn. 55, 369–382.

Schiffer, R.A., Rossow, W.B., 1983. The International Satellite Cloud Climatology Project (ISCCP): the first project of the World Climate Research Program. Bull. Amer. Meteor. Soc. 64, 779–784.

Schiro, K. A., J. D. Neelin, 2018. Tropical continental downdraft characteristics: Mesoscale systems versus unorganized convection. Atmos. Chem. Phys. 18, 1997–2010.

Schiro, K. A., Sullivan, S. C., Kuo, Y., Su, H., Gentine, P., Elsaesser, G. S., Jiang, J. H., Neelin, J. D., 2020. Environmental Controls on Tropical Mesoscale Convective System Precipitation Intensity. J. Atmos. Sci. 77, 4233–4249.

Schlueter, A., Fink, A.H., Knippertz, P., Vogel, P., 2019a. A systematic comparison of tropical waves over Northern Africa. Part I: influence on rainfall. J. Clim. 32, 1501–1523.

Schlueter, A., Fink, A.H., Knippertz, P., 2019b. A systematic comparison of tropical waves over northern Africa. Part II: dynamics and thermodynamics. J. Clim. 32, 2605–2625.

Schmetz, J., Tjemkes, S. A., Gube, M., Van de Berg, L., 1997. Monitoring deep convection and convective overshooting with METEOSAT. Adv. Space Res. 19, 433-441.

Schumacher, C., Houze Jr., R.A., 2003. Stratiform rain in the tropics as seen by the TRMM Precipitation Radar. J. Clim. 16, 1739– 1756.

Schumacher, C., Houze, R. A., 2006. Stratiform precipitation production over sub-Saharan Africa and the tropical East Atlantic as observed by TRMM, Q. J. R. Meteorol. Soc., 132(620), 2235– 2255.

Sellers, W.D., 1965. Physical Climatology. The University of Chicago Press, 272 pp.

Soden, B.J., 2000. The diurnal cycle of convection, clouds, and water vapor in the tropical upper troposphere. Geophys. Res. Lett. 27, 2173–2176.

Seneviratne, S. I., et al., 2006. Soil Moisture Memory in AGCM Simulations: Analysis of Global Land–Atmosphere Coupling Experiment (GLACE) Data. J. Hydrometeor. 7, 1090–1112.

Sherwood, S. C., Bony, S., and Dufresne, J.-L., 2014. Spread in model climate sensitivity traced to atmospheric convective mixing. Nature. 505(7481), 37–42.

Sinclaire, Z., Lenouo, A., Tchawoua, C., Janicot, S., 2015. Synoptic Kelvin type perturbation waves over Congo basin over the period 1979–2010. J. Atmos. Sol. Terr. Phys. 130–131, 43–46.

Slingo, J., Inness, P., Neale, P., Woolnough, S., Yang, G.Y., 2003. Scale interactions on diurnal to seasonal timescales and their relevance to model systematic errors. Ann. Geophys. 46, 139–155.

Soden, B.J., 2000. The diurnal cycle of convection, clouds, and water vapor in the tropical upper troposphere. Geophys. Res. Lett. 27, 2173-2176.

Soden, B.J., Fu, R., 1995. A satellite analysis of deep convection, upper tropospheric humidity, and the greenhouse effect. J. Clim. 8, 2333–2351.

Soden, B.J., Jackson, D.L., Ramaswamy, V., Schwarzkopf, D., Huang, X., 2005. The radiative signature upper tropospheric moistening. Science. 310, 841–844.

Sossa, A., Liebmann, B., Bladé, I., Allured, D., Hendon, H.H., Peterson, P. Hoell, A., 2017. Statistical connection between the Madden–Julian oscillation and large daily precipitation events in West Africa. J. Clim. 30(6),1999-2010.

Srivastava, P.K, et al., 2015. Performance evaluation of WRF-Noah land surface model estimated soil moisture for hydrological application: synergistic evaluation using SMOS retrieved soil moisture. J. Hydrol. 529, 200–212.

Stratton, R.A., et al., 2018. A Pan-African Convection-Permitting Regional Climate Simulation with the Met Office Unified Model: CP4-Africa. J. Clim. 31, 3485–3508.

Su, H., Read, W.G., Jiang, J.H., Waters, J.W., Wu, D.L., Fetzer, E.J., 2006. Enhanced positive water vapor feedback associated with tropical deep convection: New evidence from Aura MLS. Geophys. Res. Lett. 33, L05709.

Sui, C.-H., Lau, K.-M., 1992. Multiscale phenomena in the tropical atmosphere over the western Pacific. Mon. Wea. Rev. 120, 407–430.

Sui, C.-H., Lau, K.-M., Takayabu, Y.N., Short, D.A., 1997. Diurnal variations in tropical oceanic cumulus convection during TOGA COARE. J. Atmos. Sci. 54, 639–655.

Sui, C.-S., Li, X., Yang, M.-J., 2007. On the definition of precipitation efficiency. J. Atmos. Sci. 64, 4506–4513.

Sun, Q., Miao, C., Duan, Q., Ashouri, H., Sorooshian, S., Hsu, K.-L., 2018. A review of global precipitation data sets: data sources, estimation, and intercomparisons. Rev. Geophys. 56, 79–107.

Suzuki, T., 2009. Diurnal cycle of deep convection in super clusters embedded in the Madden–Julian oscillation. J. Geophys. Res. 114, D22102.

Talib, J., Taylor, C.M., Harris, B.L., Wainwright, C.M., 2023. Surface-driven amplification of MJO circulation anomalies across East Africa and its influence on the Turkana jet. Quarterly Q. J. R. Meteorolog. Soc.

Tamoffo, A.T., Moufouma-Okia, W., Dosio, A., et al., 2019. Process-oriented assessment of RCA4 regional climate model projections over the Congo Basin under 1.5°C and 2°C global warming levels: influence of regional moisture fluxes. Clim. Dyn. 53, 1911–1935.

Taylor, C.M., 2015. Detecting soil moisture impacts on convective initiation in Europe, Geophys. Res. Lett. 42, 4631– 4638.

Taylor, C.M., Belusic, D., Guichard, F., Parker, D.J., Vischel, T., Bock, O., Harris, P.H., Janicot, S., Klein, C., Panthou, G., 2017. Frequency of extreme Sahelian storms tripled since 1982 in satellite observations. Nature. 544, 475–478.

Taylor, C.M., et al., 2018. Earlier seasonal onset of intense Mesoscale Convective Systems in the Congo Basin since 1999. Geophys. Res. Lett. 45, 13458–13467.

Taylor, C.M. and Ellis, R.J., 2006. Satellite detection of soil moisture impacts on convection at the mesoscale. Geophys. Res. Lett. 33(3), L03404.

Taylor, C.M., De Jeu, R.A.M., Guichard, F., Harris, P.P., Dorigo, W.A., 2012. Afternoon rain more likely over drier soils. Nature. 489, 282-286.

Thompson, G., Field, P. R., Rasmussen, R. M., Hall W. D., 2008. Explicit forecasts of winter precipitation using an improved bulk microphysics scheme. Part II: Implementation of a new snow parameterization. Mon. Wea. Rev. 136, 5095–5115.

Tian, B., Soden, B.J., Wu, X., 2004. Diurnal cycle of convection, clouds and water vapor in the tropical upper troposphere: Satellites versus a general circulation model. J. Geophys. Res. 109, D10101.

Tian, B., Waliser, D.E., Fetzer, E.J., 2006. Modulation of the diurnal cycle of tropical deep convective clouds by the MJO. Geophys. Res. Lett. 33, L20704.

Uma, K.N., Das, S.K., 2019. Do the stability indices indicate the formation of deep convection? Meteorol. Atmos. Phys. 131, 1–10.

Vashisht, A., Zaitchik, B., 2022. Modulation of East African boreal fall rainfall: combined effects of the Madden–Julian oscillation (MJO) and El Niño–Southern oscillation (ENSO). J. of Clim. 35, 2019–2034.

Wan, Z., Hook, S., Hulley, G., 2015a. MYD11A2 MODIS/Aqua Land Surface Temperature/Emissivity 8-Day L3 Global 1km SIN Grid V006. NASA EOSDIS Land Processes DAAC.

Wan, Z., Hook, S., Hulley, G., 2015b. MOD11A2 MODIS/Terra Land Surface Temperature/Emissivity 8-Day L3 Global 1km SIN Grid V006. NASA EOSDIS Land Processes DAAC.

Ward, N., Fink, A., Keane, R., Guichard, F., Marsham, J., Parker, D., Taylor, C., 2021. Synoptic timescale linkage between midlatitude winter troughs Sahara temperature patterns and northern Congo rainfall: A building block of regional climate variability. Inter. J. Clim. 41, (5), 3153–3173.

Washington, R., James, R., Pearce, H., Pokam, W.M., Moufouma-Okia, W., 2013. Congo Basin rainfall climatology: can we believe the climate models? Phil. Trans. R. Soc. B. 368, 20120296.

Webster, P.J., 1973. Temporal variation of low-latitude zonal circulations. Mon. Wea. Rev. 101, 803–816.

Wedam, G.B., McMurdie, L.A., Mass, C.F., 2009. Comparisons of model forecast skill over the east and west coasts of the United States. Wea. Forecasting. 24, 843–854.

Wei, J., Dirmeyer, P. A., Guo, Z., Zhang, L., Misra, V., 2010. How much do different land models matter for climate simulation? Part I: Climatology and variability. J. Clim. 23, 3120–3134.

Weisman, M. L., Skamarock, W. C., Klemp, J. B., 1997. The resolution dependence of explicitly modeled convective systems. Mon. Wea. Rev. 125(4), 527–548.

Wheeler, M., Hendon, H.H., 2004. An all-season real-time multivariate MJO index: Development of an index for monitoring and prediction. Mon. Wea. Rev. 132, 1917-1932.

Worku, L. Y., Mekonnen, A., Schreck, C. J., 2019. Diurnal cycle of rainfall and convection over the Maritime Continent using TRMM and ISCCP. Int. J. Climatol. 39(13), 5191–5200.

Yang, G.Y., Slingo, J., 2001. The diurnal cycle in the Tropics. Mon. Wea. Rev. 129, 784–801.

Yang, S., Smith, E.A., 2006. Mechanisms for diurnal variability of global tropical rainfall observed from TRMM. J. Clim. 19, 5190–5226.

Yin, J., Albertson, J. D., Rigby, J. R., and Porporato, A., 2015. Land and atmospheric controls on initiation and intensity of moist convection: CAPE dynamics and LCL crossings. Water

Resour. Res. 51, 8476–8493.

Yuan, G.H., Zhang, L., Liang, J.N., Cao, J., Guo, Q., and Yang, Z.H., 2017. Impacts of initial soil moisture and vegetation on the diurnal temperature range in arid and semiarid regions in China. J. Geophys. Res.-Atmos. 122, 11568-11583.

Zaitchik, B.F., 2017. Madden-Julian oscillation impacts on tropical African precipitation. Atmos. Res. 184, 88–102.

Zelinka, M.D., Hartmann, D.L., 2009. Response of humidity and clouds to tropical deep convection. J. Clim. 22, 2389– 2404.

Zeng, X. M., Wang, B., Zhang, Y., Song, S., Huang, X., Zheng, Y., Chen, C., Wang, G., 2014. Sensitivity of high-temperature weather to initial soil moisture: A case study using the WRF model. Atmos. Chem. Phys. 14(18), 9623–9639.

Zhang, C., Dong, M., 2004. Seasonality of the Madden–Julian oscillation. J. Clim. 17, 3169–3180.

Zhang, C., 2005. Madden–Julian Oscillation. Rev. Geophys. 43, RG2003.

Zhang, Z., Li, Y., Chen, F., Barlage, M., Li, Z., 2018. Evaluation of convection-permitting WRF CONUS simulation on the relationship between soil moisture and heatwaves. Clim. Dyn. 55(1-2), 235–252.

Zhao, L., Dai, A., Dong, B., 2018. Changes in global vegetation activity and its driving factors during 1982–2013. Agric. For Meteorol. 249, 198-209.

Zhou, L., et al., 2014. Widespread decline of Congo rainforest greenness in the past decade. Nature. 509, 86–90.

Zhuo, L., Dai, Q., Han, D., Chen, N., Zhao, B., 2019. Assessment of simulated soil moisture from WRF Noah, Noah-MP, and CLM land surface schemes for landslide hazard application. Hydrol. Earth Syst. Sci. 23, 4199–4218.

Zipser, E., Liu, C., Cecil, D., Nesbitt, S., Yorty, D., 2006. Where are the most intense thunderstorms on Earth? Bull. Am. Meteorol. Soc. 87, 1057–1107.

Appendix

[1] Alber, K., Raghavendra, A., Zhou, L. et al. 2021. Analyzing intensifying thunderstorms over the Congo Basin using the Gálvez-Davison index from 1983–2018. Clim. Dyn. 56, 949–967. Reproduced with permission from Springer Nature.

Dear Kathrin,

Thank you for your recent email. Springer Nature journal authors may reuse their article's Version of Record, in whole or in part, in their own thesis without any additional permission required, provided the original publication is properly cited and includes the following acknowledgement '"Reproduced with permission from Springer Nature". This includes the right to make a copy of your thesis available in your academic institution's repository, or other repository required by your awarding institution. For more information please visit see our FAQs here.

If your awarding institution requires formal permission, please locate your article on either nature.com or link.springer.com. At the end of the article page you will find the 'Reprints and Permissions' link; clicking on this will redirect you to our CCC RightsLink service where you may input the details of your request. **Please ensure you select ''reuse in a thesis/dissertation' as your type of use, and to tick the box that asks whether you are the author.**

During the process, you will need to set up an account with RightsLink. You will be able to use your RightsLink account in the future to request permissions from Springer Nature and from other participating publishers. RightsLink will also email you confirmation of your request with a link to your printable licence.

If you have any further questions, please do not hesitate to get in touch.

Kind Regards,

Elise

Elise Lagden
Permissions Executive
SpringerNature
The Campus, 4 Crinan Street, London N1 9XW, United Kingdom
T: [0]+442078434596
E elise.lagden@springernature.com
http://www.nature.com
http://www.springernature.com

[2] Alber, K., Zhou, L., and Raghavendra, A., 2021. A shift in the diurnal timing and intensity of deep convection over the Congo Basin during the past 40 years. Atmos. Res., 264, 0169-8095. Used with permission.

[3] Alber, K., Zhou, L., Roundy, P.E., and Solimine, S.L., 2023. Influence of the Madden-Julian Oscillation on the diurnal cycles of convection and precipitation over the Congo Basin. Atmos. Res., 294, 0169-8095. Used with permission.

06/12/2023, 09:48 Mail - Alber, Kathrin - Outlook

Re: Permission to use published articles for PhD dissertation [231206-000846]

Permissions Helpdesk <permissionshelpdesk@elsevier.com>
Wed 12/6/2023 9:46 AM
To:Alber, Kathrin <kalber2@albany.edu>

Dear Kathrin Alber

We hereby grant you permission to reprint the material below at no charge in your thesis subject to the following conditions:

RE:

- **A shift in the diurnal timing and intensity of deep convection over the Congo Basin during the past 40 years, Atmospheric Research, Volume 264, 2021, Alber et al.**
- **Influence of the Madden-Julian Oscillation on the diurnal cycles of convection and precipitation over the Congo Basin, Atmospheric Research, Volume 294, 2023, Alber et al.**

1. If any part of the material to be used (for example, figures) has appeared in our publication with credit or acknowledgment to another source, permission must also be sought from that source. If such permission is not obtained then that material may not be included in your publication/copies.

2. Suitable acknowledgment to the source must be made, either as a footnote or in a reference list at the end of your publication, as follows:

"This article was published in Publication title, Vol number, Author(s), Title of article, Page Nos, Copyright Elsevier (or appropriate Society name) (Year)."

3. Your thesis may be submitted to your institution in either print or electronic form.

4. Reproduction of this material is confined to the purpose for which permission is hereby given.

5. This permission is granted for non-exclusive world English rights only. For other languages please reapply separately for each one required. Permission excludes use in an electronic form other than submission. Should you have a specific electronic project in mind please reapply for permission.

6. As long as the article is embedded in your thesis, you can post/share your thesis in the University repository.

7. Should your thesis be published commercially, please reapply for permission.

8. Posting of the full article/ chapter online is not permitted. You may post an abstract with a link to the Elsevier website [http://www.elsevier.com,/]www.elsevier.com, or to the article on ScienceDirect if it is available on that platform.

Kind regards,

Roopa Lingayath
Senior Copyrights Specialist
ELSEVIER | HCM - Health Content Management

Visit Elsevier Permissions